Equation of State and Neutrino Interactions in Neutron Star Matter with Quarks

A Dissertation Presented

by

Andrew William Steiner

to

The Graduate School

in Partial Fulfillment of the

Requirements

for the Degree of

Doctor of Philosophy

in

Physics and Astronomy

State University of New York

at Stony Brook

August 2002

Copyright © by
Andrew William Steiner
2002

State University of New York
at Stony Brook

The Graduate School

Andrew William Steiner

We, the dissertation committee for the above candidate for the Doctor of Philosophy degree, hereby recommend acceptance of the dissertation.

Madappa Prakash (Dissertation Advisor)
Professor, Department of Physics and Astronomy, Stony Brook

Gerald E. Brown
Distinguished Professor, Department of Physics and Astronomy, Stony Brook

James M. Lattimer (Chairperson of Defense)
Professor, Department of Physics and Astronomy, Stony Brook

John M. Kincaid
Professor, Department of Mechanical Engineering, Stony Brook

Gene Sprouse
Professor, Department of Physics and Astronomy, Stony Brook

This dissertation is accepted by the Graduate School.

Dean of the Graduate School

Abstract of the Dissertation

Equation of State and Neutrino Interactions in Neutron Star Matter with Quarks

by

Andrew William Steiner

Doctor of Philosophy

in

Physics and Astronomy

State University of New York

at Stony Brook

2002

Advisor: Madappa Prakash

In this dissertation, the structure and evolution of neutron stars containing deconfined quark matter are investigated. The essential microphysical ingredients, the equation of state and the associated neutrino opacity that govern the macrophysical evolution of a neutron star, are calculated and utilized in the first self-consistent dynamical calculation of a proto-neutron star containing quark matter.

It is shown that neutrino trapping inhibits the appearance of a mixed phase that leads to proto-neutron star metastability. Sufficiently massive stars containing negatively-charged, strongly interacting, particles (including quarks) may collapse to black holes during the first minute of evolution. In addition, the specific heat of the quark-hadron mixed phase is found to be much larger than

that of the kaon condensate-hadron mixed phase. This produces core temperatures significantly lower in stars containing quarks than in those not containing quarks.

Neutrino opacities in quark matter are calculated for the neutrino degeneracies and lepton contents encountered in a proto-neutron star's evolution. It is shown that the appearance of quarks in baryonic matter drastically reduces the neutrino opacity for a given entropy. Neutrino fluxes are calculated from proto-neutron stars with and without quarks. Because the neutrino flux would vanish if a black hole forms, metastability provides an obvious signal that quarks (or other types of strange matter) have appeared. The metastability timescales for stars with quarks are intermediate between those containing hyperons and kaon condensates.

The consequences of enforcing local color neutrality on the color superconducting phases of quark matter are investigated. At zero temperature, the energy cost of enforcing color and electric charge neutrality in the color-flavor-locked (CFL) phase is lower than that in the two-flavor-superconducting (2SC) phase, which favors the formation of the CFL phase. With increasing temperature and neutrino content, however, an unlocking transition occurs from the CFL phase to the 2SC phase. A new phase diagram for quark-hadron matter is presented. The CFL phase is unlikely to appear until after the neutrinos have left the star. The astrophysical implications of the structure of this phase diagram are discussed.

To my wife and my family

Soli Deo Gloria

Contents

List of Figures x

Preface xi

Acknowledgements xii

1 Introduction 1
- 1.1 Neutron Stars . . . 2
- 1.2 The Equation of State . . . 6
- 1.3 The Equation of State of Quark Matter . . . 9
  - 1.3.1 The bag model . . . 10
  - 1.3.2 Chiral symmetry and the NJL model . . . 10
  - 1.3.3 QCD at high baryon density . . . 11
  - 1.3.4 The phase diagram of QCD . . . 13
- 1.4 Mixed Phase Thermodynamics and Electro-Weak Interactions 14
- 1.5 Effects of Quark Matter on Neutron Star Structure . . . 15
- 1.6 Strange Quark Stars . . . 16
- 1.7 Neutrino Interactions in Quark Matter . . . 16
- 1.8 Time and Length Scales . . . 17
- 1.9 Organization . . . 18

2 Quark-Hadron Phase Transitions in Young and Old Neutron Stars 19
- 2.1 Thermodynamics . . . 20
  - 2.1.1 Hadronic phase . . . 20
  - 2.1.2 Quark phase . . . 21
  - 2.1.3 Proto-neutron star matter . . . 23
- 2.2 Results . . . 24
- 2.3 Discussion . . . 34

3 Diffusion of Neutrinos in Proto-Neutron Star Matter with Quarks 36
- 3.1 Theory . . . 38
  - 3.1.1 Standard model cross sections . . . 38
  - 3.1.2 Diffusion coefficients . . . 43
  - 3.1.3 EOS of neutron star matter with quarks . . . 44
- 3.2 Results . . . 45
  - 3.2.1 Cross sections of neutrino-quark reactions . . . 45

4 Evolution of Quark Proto-Neutron Stars with Quarks 49
- 4.1 Exotic Phases in Dense Matter . . . 49
- 4.2 Metastability and Black Hole Formation . . . 50
- 4.3 Equation of State and Neutrino Opacity . . . 50
- 4.4 Examples of Results . . . 51
- 4.5 Implications . . . 56

5 Color-Neutral Superconducting Quark Matter 59
- 5.1 Introduction . . . 59
  - 5.1.1 Charges, chemical potentials, and color neutrality . . . 60
- 5.2 Thermodynamics . . . 61
- 5.3 Results for $G_{DIQ} = 3G_S/4$ . . . 64
  - 5.3.1 Zero temperature and zero neutrino chemical potential 64
  - 5.3.2 Phase diagram at finite temperature and lepton content 69
  - 5.3.3 Sensitivity of Results to G_{DIQ} . . . 71
- 5.4 Astrophysical implications . . . 72
- 5.5 Conclusions . . . 72

6 Conclusions and Outlook 83

Epilogue: "Neutrinos Reveal Star's Inner Secrets" 88

A Thermodynamical Potential in the Hadronic Phase 99

B Neutrino-Quark Scattering 101
- B.1 Evaluation of the Angular Integrals from Eqs. (3.5) and (3.8) 101
  - B.1.1 The integral I_a in Eq. (3.5) . . . 101
  - B.1.2 The integral I_b in Eq. (3.8) . . . 102
- B.2 Scattering of Degenerate Neutrinos . . . 104
  - B.2.1 Results to leading order in energy transfer q_0 . . . 104
  - B.2.2 Results to all orders in q_0 for the case $\mu_2 > E_1$ . . . 105
- B.3 Scattering of Non-Degenerate Neutrinos . . . 109

B.4 Integrals Expressible as Polylogarithms 109

C Color Superfluidity **111**
C.1 The Derivation of the Mean-Field Lagrangian 111
C.2 The Thermodynamic Potential 115

List of Figures

1.1 Proto-neutron star evolution diagram 5
1.2 Schematic representation of the phase structure of neutron-star matter 8
1.3 The QCD phase diagram in the $\mu_B - T$ plane 14

2.1 Volume fraction of hadronic matter in a neutron star containing quarks in the mixed phase 25
2.2 Pressure of neutron star matter containing quarks 27
2.3 Temperature as a function of density for constant entropy per baryon 29
2.4 Concentrations of hadrons, quarks, and leptons in neutron star matter 30
2.5 Concentrations of hadrons, quarks, and leptons in hyperonic neutron star matter 31
2.6 Gravitational mass vs. radius for neutron stars containing quarks in the mixed phase 33
2.7 The phase diagram of neutron stars at finite temperature and neutrino chemical potential 35

3.1 Electron neutrino cross sections per unit volume in pure quark matter 42
3.2 Neutrino cross sections per unit volume in matter containing a mixed phase of quarks and hadrons 46
3.3 Diffusion coefficients relevant for proto-neutron star formation 48

4.1 Thermodynamic evolution of a proto-neutron star 52
4.2 Count rates in the SuperK neutrino detector for stars with or without quarks 53
4.3 The neutrino luminosity for quark proto-neutron stars with various baryon masses 55
4.4 Metastability lifetimes for proto-neutron stars with various phase transitions 57

5.1 The color density of quark matter for $\mu_3 = \mu_8 = 0$ in the NJL model 74
5.2 Dynamical masses and pairing gaps for superconducting quarks 75
5.3 The energy cost of color-neutrality in superconducting quark matter 76
5.4 The pressure of superfluid quark matter 77
5.5 The phase diagram of superfluid quark matter at finite temperature and neutrino chemical potential 78
5.6 Same as Figure 5.2, but with $G_{DIQ} = G_S$. 79
5.7 Same as Figure 5.3, but with $G_{DIQ} = G_S$. 80
5.8 Same as Figure 5.4, but with $G_{DIQ} = G_S$. 81
5.9 Same as Figure 5.5, but with $G_{DIQ} = G_S$. 82

6.1 Sudbury Neutrino Observatory 90

B.1 Neutrino-quark scattering cross sections 108

Preface

This dissertation consists of work on the effects of quark matter in neutron star cores performed during my graduate studies. Chapter 2 is based upon *Physics Letters B* **486** *(2000) 239*, Chapter 3 is based upon *Physics Letters B* **509** *(2001) 10*, and Chapter 4 is based upon *Physical Review Letters* **86** *(2001) 5223*. These works were performed in collaboration with Madappa Prakash, James M. Lattimer, and José A. Pons. Chapter 5 is based on work performed with Sanjay Reddy and Madappa Prakash; this work has been submitted for publication to *Physical Review D* (http://arxiv.org/abs/hep-ph/0205201) which is not yet published. A paper on the long-term evolution of neutron stars with quark matter, which was not included here, can be found in *Physical Review Letters* **85** *(2000) 2048*. This work was performed in collaboration with Dany Page, Madappa Prakash, and James M. Lattimer. The work in Chapter 4 was highlighted in a Physical Review Focus (http://focus.aps.org/v7/st26.html) article which is reproduced in the Epilogue.

Acknowledgements

My advisor, Prof. Madappa Prakash, has consistently gone above and beyond the call of duty in order to prepare me for the future that lies ahead. He has taken the time to teach and advise me on a number of topics while being patient with my idiosyncrasies. His daily work is characterized by honesty and moral conviction that is matched by very few people. I am indebted to him for the education I received, and look forward to continued collaboration with him as I progress in my academic endeavors.

Prof. James M. Lattimer has been an essential part of my graduate career, playing the roles of collaborator, teacher, and co-advisor during my graduate education. His dedication has contributed greatly to my success; I sincerely appreciate his time and effort.

During the past couple of years, I was afforded the opportunity to work with several excellent collaborators. The work in Chapter 4 was completed with the essential efforts of José A. Pons, now at the University of Rome in Italy. It has been a pleasure to work with Sanjay Reddy, now a staff member at Los Alamos National Laboratory, which resulted in the paper presented in Chapter 5. I have truly enjoyed working with Dany Page, at the Universidad Nacional Autonómia de México, in work not discussed in detail in this dissertation. Prof. Page was an excellent host during my travels to Mexico and made my stay enjoyable. Finally, I have had the distinct pleasure to begin an exciting collaboration with Prof. Paul J. Ellis at the University of Minnesota.

The Nuclear Theory Group at the State University of New York has been an excellent place to begin my career in Physics. I particularly appreciate the support that I have been given by Prof. Gerald E. Brown, who has made great efforts on behalf of all of the graduate students. Prof. Thomas Schäfer has been very helpful in my understanding of some of the details of high-density QCD. The Nuclear Theory Group has also provided me with many courses to broaden my understanding, including courses taught by Prof. Gerald E. Brown, Prof. Madappa Prakash, Prof. Edward Shuryak, Prof. Jacobus Verbaarschot, and Prof. Ismail Zahed.

Ellen Popenoe is the lifeblood of the Nuclear Theory Group. She consistently keeps the group alive and has been of great assistance to me in overcoming many of the hurdles associated with graduate life at Stony Brook; everything from getting paid, to rides back home when my car didn't feel up to the task. I appreciate her efforts to greatly improve the quality of my life.

I would like to acknowledge the support of my peers, Prashanth Jaikumar, Derek Teaney, Achim Schwenk, Pietro Faccioli, and Loïc Grandchamp-Desraux, who have demonstrated great patience with my persistent questions.

I would like to thank my family for encouraging me to follow my dreams and encouraging me during difficult times. Finally, I would like to thank my wife Michelle for loving and supporting me without reservation. This work would not have been possible without her.

Chapter 1

Introduction

The primary goal of this work is to explore the effects of the presence of deconfined quark matter on the structure and evolution of neutron stars. Special emphasis will be placed on identifying distinctive signatures in basic observables of neutron stars, such as (i) their masses and radii, (ii) their surface temperatures, and (iii) the neutrino luminosities from their newly-born state (termed proto-neutron stars) in the aftermath of galactic core-collapse supernovae. Essential microphysical ingredients are calculated, namely the equation of state and the associated neutrino opacity and emissivity which governs the macrophysical evolution of a neutron star containing quark matter. These physical inputs are then used to perform detailed simulations of a neutron star from its birth to old age (up to millions of years). The existence of quark matter in neutron stars might be confirmed by multiwavelength photon observations with new generation satellites such as the Hubble Space Telescope (HST), Chandra, and X-ray–Multi-Mirror–Newton (XMM-Newton), and by neutrino signals from future galactic supernovae in detectors like Super-Kamiokande, the Sudbury Neutrino Observatory (SNO), and others under consideration, including the Underground Neutrino Observatory (UNO).

Neutron stars are nearly the only objects in the universe where matter at extremely high baryon densities (up to 5-10 n_0 where $n_0 \approx 0.16$ fm^{-3} is the empirical nuclear equilibrium density) are encountered. Matter at such high densities is inaccessible in the laboratory except for very short times in relativistic heavy ion collisions. In such collisions, very high temperatures (up to hundreds of MeV) are reached, much larger than what is encountered in neutron stars. Combining knowledge from studies of neutron stars and heavy ion collisions will enable us to construct the phase diagram of strongly interacting matter in the temperature (T) versus baryon density (n_B), or equivalently, chemical potential (μ_B) plane. Furthermore, the study of neutron stars offers the opportunity to extend the phase diagram to include the lepton chemical

potential (μ_L), since neutrinos are trapped inside neutron stars during their early stages of evolution. Rapid developments, including those in this work, are currently taking place in effective approaches to the theory of strong interactions, Quantum Chromo-Dynamics (QCD), at high baryon densities. (Exact calculations, such as the successful lattice simulations at finite T, remain technically infeasible at finite μ_B or n_B relevant for neutron stars). Some examples of these developments include color superconductivity, Bose condensation, etc. These possibilities offer the promise of establishing the properties of QCD in the $\mu_B - \mu_L - T$ plane in addition to delineating the composition, structure, and evolution of both newly-born and old neutron stars. Undoubtedly, the evergrowing observations of neutron stars will provide a testing ground where the recent developments in the study of quark matter may be confirmed.

1.1 Neutron Stars

Neutron stars originate in supernovae. Baade and Zwicky [1] first suggested in 1934 that neutron stars are the collapsed cores of massive (> 8 M$_\odot$) stars and are created when the outer mantle of the progenitor red-giant star explodes. The supernova explosion is powered by the gravitational binding energy ($\sim 3GM^2/5R \approx 3 \times 10^{53} (M/1.4\ \mathrm{M}_\odot)^2$ ergs) released in stellar collapse. The physical processes that drive a supernova explosion have been understood by considering the entropy and the electron fraction of stellar matter. Illuminating discussions that identify the various important stages may be found in Refs. [2, 3, 4, 5]. Although heat is initially lost from the core due to the escape of neutrinos, matter quickly becomes dense enough to be opaque to neutrinos, shutting off this cooling. A general picture of collapse has now emerged. When the core mass exceeds the Chandrashekar mass, which depends sensitively on the electron fraction of matter, the core collapses. Electron degeneracy pressure is no longer able to support the core against gravitational collapse. Collapse is accelerated by processes like $e^- + p \to n + \nu_e$. The entropy per nucleon of matter in a star's core during collapse remains nearly constant, on the order of unity. The combination of neutron degeneracy pressure and the short-distance repulsion of nuclear interactions stops the stellar matter from complete gravitational collapse when the central density is a few times nuclear equilibrium density, n_0. The pressure due to strong interactions of matter at this density creates a shock wave at the outer boundary of the inner core. This shock wave initially propagates outward, then stalls due to energy expended in neutrino losses and the dissociation of nuclei. The core of the progenitor star becomes a "proto-neutron star" (PNS). Numerical calculations [6, 7] have gen-

erally verified this picture, but have not yet succeeded in achieving an actual "explosion" of the outer mantle that is as powerful as what is observed.

The subsequent evolution of the neutron star can be divided into two parts. We will designate the evolution for the first minute after collapse as "short-term evolution" and the subsequent evolution, up to a million years of age, as "long-term evolution." The short-term evolution, during which the neutron star is referred to as a proto-neutron star, can be characterized by several important stages (Figure 1.1):

- *From Stage 1 to Stage 2:* The shock wave which stalled is revived by neutrino emission and ejects the outer layers of the star. The star radiates copious amounts of neutrinos of all flavors. If the core is sufficiently massive $\gtrsim 2-3$ $M_\odot$, or if it accretes enough mass from a companion, it forms a black hole within a fraction of a second.

- *From Stage 2 to Stage 3:* The hot dense core, now a neutron star, is sufficiently dense to keep neutrinos from leaving the star within the dynamical timescale of tens of seconds [8]. The neutrinos are effectively "trapped", since their mean free path (see Eq. (3.11))

$$\lambda_\nu \approx (10 G_F^2 E_\nu^2 \mu_n)^{-1} \sim 2 \text{ cm} \tag{1.1}$$

  where $G_F \sim 10^{-5}/m_p^2$ is the Fermi coupling constant, $E_\nu \sim 10$ MeV is the neutrino energy, and $\mu_n \sim 1000$ MeV is the nucleon chemical potential, is much shorter than the radius of the star ($\sim$ 15-20 km). The region where neutrinos decouple from matter because the density is not sufficiently large to trap them is called the "ν-sphere". Neutrinos outside of this region escape from the star with a near-thermal distribution with a temperature equal to that of the temperature of matter at the ν-sphere. In the core, the lepton number per baryon ($Y_L \sim 0.4$) is fixed by beta-equilibrium reactions which occur much faster than the dynamical time scale. Neutrinos leak out of the neutron star, which further heats the matter through Joule heating, and the neutrino fraction, Y_ν, becomes small on a time scale of tens of seconds. As explained below, the departure of the neutrinos allows the presence of deconfined quark matter in the core. Several other components may appear at this stage, including hyperons, and pion or kaon condensates. The "deleptonization" of the star lowers its maximum mass. If the maximum mass is lowered below the mass of the neutron star, it collapses to a black hole [9].

- *From Stage 3 to Stage 4:* The neutrino chemical potential vanishes as the neutrinos become extremely non-degenerate. The star continues to cool via neutrino emission and the temperature becomes less than 1 MeV within a minute.

This general picture of proto-neutron star evolution proposed in Refs. [10, 11] has emerged from detailed numerical simulations and has been verified for neutron stars containing solely nucleonic matter [12], those additionally containing hyperons [12], and for neutron stars with kaon condensates [13]. One of the goals of this work is to perform similar calculations taking into account the possible presence of deconfined quark matter [14], self-consistently including the effects of quarks on the equation of state [15] and the interactions of quarks with neutrinos [16].

The long-term evolution of a neutron star proceeds according to the following scenario. After the first minute, the cooling wave that began in the core is initially prohibited from reaching the surface by a high-entropy outer crust which insulates the core. After $\sim$ 100 years, the cooling wave diffuses to the surface of the star and the star becomes nearly isothermal. In the so-called "standard scenario" [17, 18] the proton content of the matter is quite low (<10%), and the star must cool by the relatively slow modifed Urca processes

$$n + n \to n + p + e^- + \bar{\nu}_e \qquad \text{and} \qquad p + p \to p + n + e^- + \bar{\nu}_e \tag{1.2}$$

in order to simultaneously satisfy energy and momentum conservation. However, if the proton fraction is sufficiently large, or if other exotic components (hyperons, bose-condensates, or quarks) appear, then the star instead cools by the more rapid direct Urca process

$$f_1 \to f_2 + e^- + \bar{\nu}_e \,, \tag{1.3}$$

where f_1 and f_2 represent any pair of particles involved in a beta-decay reaction [19, 20]. The cooling history of the star thus depends sensitively on the proton content of dense matter, which is not well known. Furthermore, cooling rates can be significantly suppressed by superfluidity, which affects beta decay processes involving nucleons, hyperons, and quarks, when the associated gap is larger than the temperature.

Neutrino cooling dominates the thermal evolution for $\sim 10^5$ years, after which time photon cooling is more important. After 10^7 years, the temperature is so small that the neutron star becomes extremely difficult to detect.

Neutron star evolution is a complex process involving several microphysical ingredients. The equation of state of neutron-star matter determines the structure and size of the neutron star as it evolves hydrostatically. The composition of dense matter affects global properties of the star, as well as its

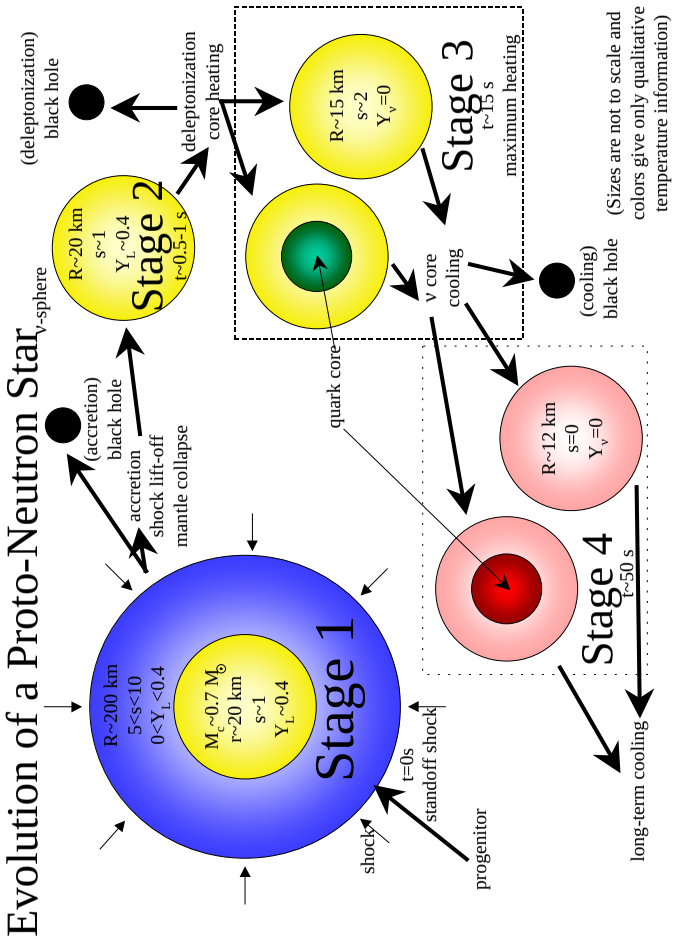

Figure 1.1: A schematic diagram of proto-neutron star evolution. This diagram is fashioned after Ref. [10].

dynamical evolution. Since the energy released in neutron star evolution is dominated by neutrinos for the first 10^5 years, both neutrino emissivities and absorptivities of matter become critical. Neutrino transport is essential to the short- and long-term evolution. These microphysical issues: the equation of state and the ν-interactions, will be directly addressed with regard to the effects of deconfined quark matter.

1.2 The Equation of State

An equation of state gives the pressure or energy density as a function of density for the various temperatures that are relevant to any particular problem. In the case of neutron stars, the electron fraction of matter is an additional variable and is directly connected with the isospin content of matter through the conditions of charge neutrality and beta-equilibrium, as discussed in detail below. A schematic representation of the many phases possibly encountered in a neutron star is shown in Figure 1.2. In order of increasing density, at least four regions may be identified:

1. *"Surface"* ($\rho < 10^6$ g/cm^3): Assuming no magnetic field and in the absence of accretion from a companion star, matter in this region consists of Fe peaked nuclei in a lattice surrounded by a gas of electrons.

2. *"Outer crust"* (10^6 g/cm$^3 < \rho < \rho_{nd}$): In the outer crust, the equilibrium nucleus chosen by the system varies; nuclei become increasingly neutron-rich as the density increases. This picture is modified when we reach the "neutron drip" density, $\rho_{nd} \sim 4.3 \times 10^{11}$ g/cm^3 where neutrons drip out of nuclei to form a gas. These neutrons, no longer confined to nuclei, are superfluid and pair in the $^1S_0$ channel.

3. *"Inner crust"* ($\rho_{nd} < \rho \lesssim \rho_{nuc}$): As the density increases beyond neutron drip density, there is a phase transition to "nuclear matter", a liquid-like state of neutrons, protons, and a gas of electrons where there is little geometrical structure [21, 22]. The neutrons and protons are both likely superfluid at densities near nuclear matter density. Nuclear matter resembles the matter in the center of large nuclei at the saturation density $\rho_{nuc} \sim 2.8 \times 10^{14}$ g/cm$^3 = 0.16$ fm^{-3}. Near the phase transition density, exotic nuclei with non-spherical shapes and small proton fraction supply the transition between nuclei and nuclear matter [23, 24].

4. *"Core"* ($\rho_{nuc} \lesssim \rho$): Matter in the core above nuclear density generally consists mostly of neutron-rich nuclear matter with electrons and muons.

Several other components may contribute, most notably hyperons and Bose-condensates [10]. At some critical density, hadrons melt into nearly-free quarks. The critical density for the hadron to quark transition, $\rho_c \sim (5-10)\rho_{nuc}$, remains model dependent.

Only the equation of state above $\sim \rho_{nuc}/2$ will be discussed in detail here. For the low-density region, we will use the results from Refs. [21, 25] in our numerical calculations.

The description of hadronic matter at densities near nuclear matter density requires a non-perturbative many-body approach. The first is a potential model approach. Typically, a Hamiltonian with a nucleon-nucleon potential is constructed to match two-body nucleon-nucleon scattering data (a recent collection may be found in the Nijmegen database [26]) and the properties of the deuteron. From this Hamiltonian, the nuclear-many body problem is solved, either by diagrammatic (Brueckner-Bethe-Goldstone) or variational (Monte Carlo) methods. Two-body interactions have benn found not to give saturation at nuclear matter density, therefore, three-body forces must be added to the original Hamiltonian [27]. These three-body forces, which are not well understood, form a large part of the uncertainty in these methods. One can write the energy density of nucleonic matter as

$$\varepsilon = \varepsilon_n + \varepsilon_p + V(n_n, n_p, T)\,, \tag{1.4}$$

where ε_i and n_i $(i = n, p)$ are the kinetic energy and number densities and V is a potential that contains information about the nucleon-nucleon interaction. Potential model approaches are generally computationally intensive and have acausal (the speed of sound in matter exceeds the speed of light) high-density behavior [28, 29].

The second approach to the equation of state near nuclear matter density is the use of field theory [30]. Here, one calculates the equation of state utilizing the mean-field approximation to a local and renormalizable Lorentz-covariant Lagrangian density. One can go beyond the mean-field approximation and include loop effects, but this process often does not converge, owing to the large coupling constants involved [31]. The coupling constants in the Lagrangian are fixed to the empirical properties of nuclear matter. This method does not allow a direct connection to nucleon-nucleon scattering, but is usually computationally less intensive than the potential model approach, and is causal at all densities because of Lorentz-covariance. A mean-field approximation will be used for the hadronic equation of state in Chapters 2, 3, and 4.

Recently, renormalization group techniques have been brought to bear on effective field theories [32]. In this approach, the fields in the Lagrangian are

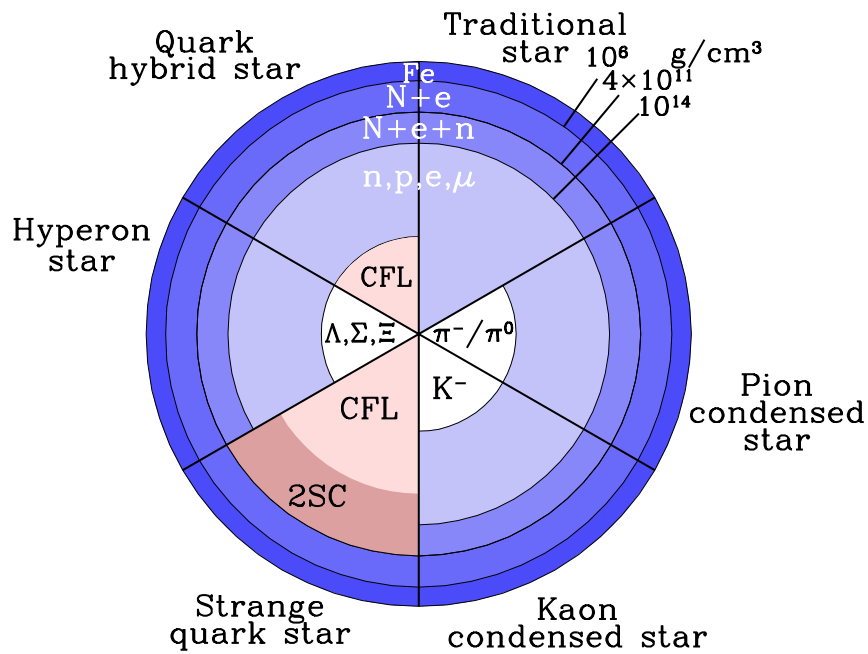

Figure 1.2: Schematic representation of the phase structure of neutron-star matter.

no longer fundamental fields. The most general Lagrangian consistent with the symmetries of the problem involving the interaction of effective fields is constructed. The constraint of renormalizability is dropped, and the theory is intended to be used at the mean-field level. A momentum cutoff is often imposed in order to integrate out the high-energy degrees of freedom that will likely not contribute at the energies of interest. Appealing to a connection to density functional theory, the energy density derived from the effective Lagrangian is viewed as providing the energy functional that is guaranteed to exist [33, 34]. This effective field theory prescription provides a scheme in which the number of coupling constants may be truncated, so as to allow for some predictive power. In the methods that we use, this scheme is valid since the meson fields are small compared to the nucleon mass in the region of interest.

Figure 1.2 displays some of the phases that may occur in the dense matter of neutron stars. Proceeding clockwise from the top, the traditional neutron star consists solely of neutrons and protons with a central density lower than that necessary to produce exotic components. Alternatively a pion or kaon condensate may appear in the core, softening the equation of state. The neutron star may transit to a "strange-quark" star consisting almost entirely of quarks. Hyperons may also appear at high densities, slowly replacing neutrons and protons with strangeness bearing hadrons. With increasing density, deconfined quark matter may appear in the core. The thrust of this work is concerned with the possible occurrence of quark matter in neutron star cores and to explore its observable consequences.

1.3 The Equation of State of Quark Matter

Quark interactions are governed by Quantum-Chromodynamics (QCD), the SU(3) gauge field theory that describes the interactions of quarks and gluons through the Lagrangian

$$\mathcal{L}_{\rm QCD} = \bar{\psi}_i \left(i \not{D}_{ij} - m_{ij} \right) \psi_j - \frac{1}{4} F^a_{\mu\nu} F^{\mu\nu a} \,, \tag{1.5}$$

where the color field-strength tensor is given by $F^a_{\mu\nu} = \partial_\mu A^a_\nu - \partial_\nu A^a_\mu - g f^{abc} A^b_\mu A^c_\nu$, and the covariant derivative is given by $\not{D}_{ij} = \gamma^\mu \delta_{ij} \partial_\mu + g \gamma^\mu A^a_\mu t^a_{ij}$. The color indices i, j in the fundamental representation take values from 1 to 3 and the color indices a, b, and c in the adjoint representation take values from 1 to 8. The input current quark masses are given in the diagonal mass matrix m. QCD is asymptotically free; at high energies (or high densities) the value of

the coupling constant is small, and perturbation theory provides an excellent description of experiment. The construction of the equation of state of quark matter at the moderate densities that are relevant for neutron star studies, however, is difficult because of non-perturbative effects. Further complicating the problem, quarks are known not to be the effective degrees of freedom of low-density matter. At low densities, quarks are "confined" into color-singlet objects: "baryons" and "mesons", and the phase transition from confined to deconfined matter occurs only at high density or temperature. Numerical simulations of QCD on the lattice, while successful at describing QCD at near zero baryon density and finite temperature, are not yet useful for densities and temperatures of relevance to neutron stars. These difficulties necessitate the use of effective theories of QCD, two of which will be discussed in detail and employed in this work: the MIT Bag model and the Nambu–Jona-Lasinio (NJL) model.

1.3.1 The bag model

The essence of the MIT bag model lies in the assumption that non-perturbative effects of QCD can be subsumed into one parameter called the bag constant [35, 36]. This bag constant, which has the dimensions of pressure, mimics the confinement of quarks into hadrons ("bags"). The pressure in the bag model is given by

$$P = -B + \sum_{i=u,d,s} \left[P_i(\mathrm{FG}) + P_i(\mathrm{Int}) \right] \tag{1.6}$$

where P_i represents the free Fermi gas (FG) contribution to the pressure from the up (u), down (d), and strange (s) quarks. (The remaining three flavors, charmed, bottom, and top quarks, are suppressed at the densities of interest, because of their large masses.) The effects of perturbative gluon exchange are also often included as $P_i(\mathrm{Int})$ [37]. These corrections can be viewed as introducing a density dependence in the bag constant B, which justifies the use of an effective bag constant B_{eff} in many calculations.

1.3.2 Chiral symmetry and the NJL model

In the limit where the bare masses of the quarks is zero, the QCD Lagrangian is invariant under the chiral transformations

$$\begin{aligned} \psi &\to \psi e^{-i\vec{\lambda}\cdot\vec{\theta}} && \text{vector} \\ \psi &\to \psi e^{-i\gamma_5\vec{\lambda}\cdot\vec{\theta_2}} && \text{axial} - \text{vector}\,, \end{aligned} \tag{1.7}$$

where ψ is a SU(3) vector made up of u,d, and s quarks, and $\vec{\lambda}$ are the SU(3) matrices. The ground state of QCD, however, is not invariant under the axial-vector transformation and therefore the ground state is said to spontaneously break chiral symmetry. As a result of this broken chiral symmetry, the quarks acquire a "dynamically generated mass". It is this dynamically generated "quark" mass which gives mass to a "hadron". At sufficiently large density or temperature, this chiral symmetry is restored and the quarks retain only their "current quark masses" which are an explicit input for the QCD Lagrangian.

The SU(3) Nambu–Jona-Lasinio (NJL) Lagrangian

$$\begin{aligned}\mathcal{L} &= \bar{q}(i\partial\!\!\!/ - \hat{m}_0)q \;+\; G\sum_{k=0}^{8}[\,(\bar{q}\lambda_k q)^2 + (\bar{q}i\gamma_5\lambda_k q)^2\,] \\ &- \; K\,[\,\det{}_f(\bar{q}(1+\gamma_5)q) + \det{}_f(\bar{q}(1-\gamma_5)q)\,] \end{aligned} \tag{1.8}$$

shares many of the same symmetries as QCD. The quark fields for the up, down, and strange quarks are denoted by the spinor q which is an SU(3) vector, λ_k are the SU(3) matrices, m_0 is a diagonal quark mass matrix, and G and K are dimensionful coupling constants. This model dynamically breaks chiral symmetry as described above. The six-fermion interaction, which mixes the flavor degrees of freedom, breaks $U_A(1)$ symmetry and is able to account for the masses of the η (547 MeV) and η' (958 MeV) [38], which are otherwise degenerate. The NJL model also qualitatively reproduces the meson mass spectrum [39]. Gluons are not explicitly considered, but can be viewed as moderating the strength of the four- and six-fermion interactions. This model is non-renormalizable, and requires the presence of a momentum cutoff; physically meaningful results are resticted to momentum scales well below this cutoff scale.

The fundamental scale of QCD, $\Lambda_{\rm QCD}$, has been estimated to be ~ 200 MeV; at this scale the strong coupling constant, g, is large. The scale for chiral symmetry breaking can be estimated to be on the order of the momentum-cutoff in the NJL Lagrangian. Above this cutoff, about 1 GeV, chiral symmetry is restored. The region between these two scales is where we expect the NJL model to be valid; in this region chiral symmetry is not yet fully restored.

1.3.3 QCD at high baryon density

At asymptotically high density, the relevant degrees of freedom in QCD are quarks and gluons. The perturbative ground state is composed of nearly free and nearly massless quarks interacting weakly through one-gluon exchange in a phase where chiral symmetry has been restored. There is a singularity

in small-angle quark scattering in perturbation theory that is regulated by the presence of a superfluid gap; quarks with equal and opposite momenta form Cooper pairs. These gaps, Δ, were first calculated in Refs. [40, 41] and estimated to be on the order of 1 MeV. Recent interest in superconductivity has been kindled by new results [42, 43] that give much larger gaps, of order 100 MeV. As in BCS theory, these gaps will weaken for $T \gtrsim \Delta/2$. If quark matter exists in neutron stars, gaps of order 100 MeV would almost certainly have an effect on the phase structure of their cores and their evolution.

In QCD with three colors and three massless quark flavors, a pair of quarks cannot be either a color or flavor singlet. The formation of Cooper pairs breaks color and flavor symmetries separately. There is, however, a combination of color and flavor symmetries which is not broken. This symmetry locks color and flavor so that a rotation in color space is canceled by a corresponding rotation in flavor space. The color-flavor-locked (CFL) phase is the most likely candidate [42] for the ground state of quark matter at asymptotically high densities. The condensate is of the form

$$\left\langle \psi_L^{\alpha a}\psi_L^{\beta b}\right\rangle \sim \Delta\epsilon^{\alpha\beta\gamma}\epsilon^{ab\gamma}\,, \tag{1.9}$$

where α and β are color indices and a and b are flavor indices, and a similar relation holds for the right-handed condensate. This condensate indirectly breaks chiral symmetry in a qualitatively different way than chiral symmetry is broken in the vacuum. The spontaneous breaking of chiral symmetry in vacuum generates a mass through the presence of quark–anti-quark pairs which modifies the quark propagator. Because of superfluidity, chiral symmetry is broken again at high density, even though the dynamical masses of the quarks may remain small.[1] The spontaneous breaking of chiral symmetry at large densities creates new Goldstone bosons [44, 45, 46, 47].

The current mass of the strange quark (~ 150 MeV) modifies this picture. When $m_s^2/2\mu \gtrsim \Delta$, the mismatch of the strange and non-strange Fermi surfaces impedes the pairing of strange and non-strange quarks. This leads to the formation of a two-flavor superconducting (2SC) phase, where up and down quarks are paired with each other and chiral symmetry is restored. (The strange quarks, in this phase, may pair among themselves, but the estimated gaps are on the order of keV, not tens of MeV). If isospin symmetry is explicitly broken, then there may be a more complicated structure to the phase diagram, since the us and ds gaps may not vanish at the same point.

[1] This is the case in the NJL model of Chapter 5. This is not the most general possibility, as the superfluid gap may also affect the dynamical mass.

The quark gaps have a small effect (of order Δ^2/μ^2) on the equation of state and the global thermodynamics of the neutron star. This may be understood in the following way: superfluidity only affects states near the Fermi surface giving a pressure of order $\mu^2\Delta^2$ while without superfluidity, the pressure is an integral over the entire Fermi sphere and of order μ^4. However, quark-matter superconductivity affects the neutrino opacities in dense matter [48], the stability of r-modes [49], the specific heat of neutron-star matter, the electrical conductivity and magnetic properties of matter [50], and the moment of inertia of the neutron star [51]. Because of the color structure of the condensate in Eq. (1.9), the equation of state must be constructed to ensure that there is no local color density in neutron star matter. A local color-density would generate a large color-electric field and matter would reorganize itself to make this field vanish. In models which do not account for the explicit effects of gluons, we must enforce color neutrality through an external condition, as detailed in Chapter 5.

1.3.4 The phase diagram of QCD

The phase diagram of QCD at finite density and temperature is shown schematically in Figure 1.3. At low densities and temperatures, the ground state of matter is confined into hadrons. At large temperatures, the ground state consists of nearly-free quarks and gluons often referred to as the "Quark-Gluon Plasma" (QGP). The low-density transition from hadronic matter to the QGP is known through lattice calculations to occur at around 150-200 MeV and is thought to be second order in nature. Deconfined quark matter is disfavored by the presence of neutrinos and so this temperature rises in the presence of a neutrino chemical potential. At low temperatures, the transition between these two phases is altered by the presence of superfluid phases. When quarks become deconfined, they acquire a gap in their energy spectra. The low-density quark phase is likely either the CFL phase or the 2SC phase. The details of this picture depend strongly on the strength of pairing interactions, which is not well understood because of the non-perturbative nature of QCD. The sensitivity of the phase diagram to the strength of the pairing interactions is studied in detail in Chapter 5. As the density increases further, the CFL phase is favored (the strange quark mass becomes much smaller than μ) and persists as $\mu \to \infty$. The order of the transition between the 2SC phase and the CFL phase is likely to be first order at low temperatures and may become second order as the temperature increases. The CFL phase also contains more structure due to different patterns of meson condensation [52], and we ignore this structure in Figure 1.3 for simplicity. At sufficiently high temperatures,

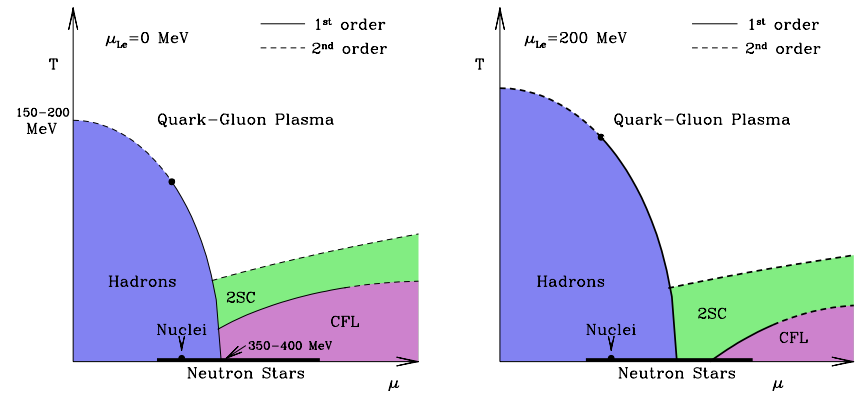

Figure 1.3: The phase diagram of QCD in the $\mu_B - T$ plane.

the gap between up and down quarks in the 2SC phase melts, and there is a second order phase transition to the QGP. Neutron stars inhabit the cold (compared to heavy-ion collisions) and dense region in Figure 1.3 illustrated by the thick black line.

1.4 Mixed Phase Thermodynamics and Electro-Weak Interactions

Since the deconfinement phase transition is not sufficiently well understood to predict its basic thermodynamic properties, we construct a first-order phase transition from hadronic matter to quark matter by following Gibbs' phase rules. A Gibbs construction between phases I and II guarantees that matter is in mechanical, thermal, and chemical equilibrium, i.e.

$$P_I = P_{II}, \qquad T_I = T_{II}, \qquad \text{and} \qquad \mu_{i,I} = \mu_{i,II}\,, \tag{1.10}$$

where μ_i are the chemical potentials corresponding to all conserved charges. In the lowest-order approximation, one can assume that the Coulomb interactions with leptons are negligible and treat them as massless degenerate Fermi gases. Including the Coulomb interactions results, at the lowest order, in heterogeneous structures which appear in the mixed phase [53, 54, 55, 56] analogous to the structures that appear in the phase transition between nuclei and nuclear

matter mentioned above. The tau leptons are not present because of their large mass, but all other leptons can contribute.

Weak interactions enforce β-equilibrium on a time scale shorter than the evolutionary time scales mentioned above. The resulting conditions on the chemical potentials take the form:

$$\mu_i = b_i \mu_n - q_i(\mu_l - \mu_{\nu_\ell}) \,, \tag{1.11}$$

where b_i is the baryon number of particle i and q_i is its charge.

To lowest order, the entropy per baryon and the lepton number of the core of the neutron star at Stage 2 in Figure 1.1 may be taken to be constant as a function of density. This is because even as neutrinos are lost from the surface layers with an attendant loss in its entropy, neutrino absorption and scattering processes in the core heat up the interior [10, 11, 12, 57]. We will utilize this approximation in Chapters 2 and 3 to outline the short-term evolution of a neutron star that permits quark matter in its core. This approximation is relaxed in Chapter 4 where a full proto-neutron star evolution is performed, beginning with a composition and temperature profile taken from modern supernova simulations.

1.5 Effects of Quark Matter on Neutron Star Structure

A transition to quark matter, like phase transitions to hyperonic or Bose condensate matter, generally softens the equation of state; it makes the pressure increase more slowly with increasing density compared to the case in which a phase transition is absent. This typically lowers the maximum mass and increases the radius and central density of the maximum mass configuration. The decrease in maximum mass associated with the softening of the equation of state leads to one of the most promising signals for quark matter in neutron star evolution: metastability [9, 58]. If the neutron star maximum mass decreases below the mass of the neutron star as a result of the appearance of a softening component, such as quark matter, the neutron star will collapse into a black hole in tens of seconds. This has been confirmed in detailed proto-neutron star evolution calculations for neutron stars with hyperons [12], and kaon condensates [13]. Chapter 4 gives an account of a similar phenomenon occurring in neutron stars with quarks in their core in addition to comparisons with other possible scenarios.

1.6 Strange Quark Stars

Witten [59] proposed that matter containing strange quarks might be absolutely stable, i.e. the energy per baryon of three flavor quark matter may be lower than the energy per baryon of ordinary nuclear matter. This leads to the notion of a self-bound strange quark star which consists almost entirely of quark matter. The energy density of the strange quark star is approximately uniform throughout the star which leads to the relation $M \sim R^3$. This mass- radius behavior is characteristic of strange quark stars and differs considerably from the usual neutron star equation of state in which the radius is nearly independent of mass for $M \sim 1.4$ $\mathrm{M}_\odot$ [60].

One of the primary gaps in our present understanding of strange quark stars is the story of their short-term evolution. The evolution of a strange star might proceed as follows: (1) A supernova explosion creates a neutron star with a central density high enough to create deconfined quark matter. (2) In order to maintain beta-equilibrium, strange quarks are created via the weak interaction. (3) This strange quark matter, because it is absolutely stable, causes the nuclear matter near the phase transition to convert to strange quark matter. (4) This conversion flows out to the stellar surface. The understanding of the details of how strange quark stars are formed is necessary in order to validate any conclusions concerning their behavior. In addition, the question of what happens at the surface of strange quark stars is the subject of recent investigation. A strange quark matter core remains hot and is unable to cool through photons because of the large plasma frequency of quark matter. The long-term evolution is therefore characterized by a slower cooling than a normal neutron star. However, as explored in Ref. [61], the surface may cool through pair production at the surface, which is more efficient. Such stars may appear rather different that "normal" neutron stars because of their non-thermal, high-energy radiation. Strange quark stars will not be directly addressed here.

1.7 Neutrino Interactions in Quark Matter

In a proto-neutron star, neutrino scattering and absorption dominate the evolution and cooling. Neutrino cross sections in quark matter are generally smaller than hadronic matter for two reasons: (i) the vector and axial-vector coupling constants are nearly equal for quarks and tend to cancel each other in the matrix element, and (ii) relativistic effects. As discussed in Chapter 2, since cross sections scale with T^2, this effect is magnified by the relatively high specific heat of quark matter. Constant adiabats of quark matter then have

lower temperature than those of hadronic matter.

Since the relevant energies in neutron stars are much less than the mass of the electroweak gauge bosons, neutrino cross sections are well described by the four-fermion model of electro-weak interactions which is given by

$$\mathcal{L} = \frac{G_F}{\sqrt{2}} \left(\overline{\psi}_{p_1}(1-\gamma_5)\psi_{p_3}\right) \left(\overline{\psi}_{p_2}(\mathcal{V}-\mathcal{A}\gamma_5)\psi_{p_4}\right) + \text{H.C.} \tag{1.12}$$

where $\mathcal{V}$ and $\mathcal{A}$ are the vector and axial-vector coupling constants for the process $p_1 + p_2 \to p_3 + p_4$. At lowest order, neutrino cross sections can be calculated from Fermi's Golden Rule:

$$\begin{aligned} \frac{\sigma}{V} &= \frac{g}{2E_1} \int \frac{d^3p_2}{2E_2\,(2\pi)^3} \int \frac{d^3p_3}{2E_3\,(2\pi)^3} \int \frac{d^3p_4}{2E_4\,(2\pi)^3} \left[\langle M_{fi}\rangle^2 \right. \\ & \left. f_2\,(1-f_3)\,(1-f_4)\,(2\pi)^4\,\delta^4\,(p_1+p_2-p_3-p_4)\right] , \end{aligned} \tag{1.13}$$

These cross sections are calculated in Chapter 3. Here, diffusion coefficients are used to estimate the effect of quark matter on neutrino transport in proto-neutron star evolution. Corrections to these results due to strong and electromagnetic correlations may be calculated using the techniques of linear response theory [62].

Quark superfluidity suppresses these cross sections by a factor of order $\exp(-\Delta/T)$. Since temperatures in neutron stars are never larger than 40 MeV, this suppression factor is large. The effects of this suppression and the effects due to the Goldstone bosons in the CFL phase are studied in Refs. [48, 63, 64].

1.8 Time and Length Scales

There are several length and time scales relevant to proto-neutron star evolution which can be easily estimated. The neutrino mean free path in the center of the neutron star was estimated in Eq. (1.1) to be $\lambda_\nu \sim 2$ cm. Taking the velocity of neutrinos to be c, gives an average time between collisions of 6×10^{-9} s. Using an estimate for the neutron star radius of about 12 km, this gives the time scale of neutrinos to leave the star (the "deleptonization" time scale) of $\tau_d \approx R^2/(c\lambda_\nu) \sim 24$ s. Because the time between collisions is so much smaller than the deleptonization time, the neutrinos can be treated as degenerate. The cooling time is slightly larger $\tau_c \sim (1-2)\tau_d$ [10], so the star cools only after the neutrinos leave. For comparison, black hole formation proceeds according to the free-fall time $\tau_{bh} \approx \sqrt{2GMR/c^2} \sim 10^{-5}$ s. This is much faster than

any other time scale and is therefore essentially instantaneous. Because the time scales for the strong and weak interactions are much smaller than τ_d, neutrinos interact frequently enough that the evolution of the proto-neutron star is approximately hydrostatic [10, 11, 12, 57].

1.9 Organization

In Chapter 2, the equation of state of neutron-star matter with quarks and hyperons will be calculated using a mean-field approximation for the hadronic equation of state and using the NJL model or the bag model for the quark equation of state [15]. New results for finite temperature with and without trapped neutrinos are presented and summarized in a phase diagram. Using this work, the neutrino opacities in neutron-star matter are presented in Chapter 3. The cross sections of neutrino scattering and absorption in neutron-star matter with quarks including consistently the effects of finite temperature and in-medium effects of the equation of state from Chapter 2 are given [16]. The goal here is the calculation of appropriate diffusion coefficients, a necessary ingredient for proto-neutron star evolution calculations. The evolution calculation is summarized in Chapter 4 which simulates the first minute of a neutron star with quark matter [14]. The neutrino signal from a proto-neutron star is calculated, along with the expected detector response assuming that a galactic supernova is detected with SNO, SuperK, or the proposed detector, UNO. This is the first calculation of metastability times for neutron stars containing quarks and allows comparison to metastability times for other softening components. In Chapter 5, the effects of quark superfluidity will be considered [65]. This chapter presents the first calculation of the phase structure of neutron star matter at finite temperature and neutrino chemical potential which consistently treats the diquark interaction to all orders in the strange quark mass and enforces color neutrality. The gaps and dynamical masses are computed as a function of density, and the CFL and 2SC phases are compared in order to construct a phase diagram of quark matter relevant for proto-neutron stars. Chapter 6 contains conclusions, discussion, and outlook. The work in Chapter 4 was chosen to be a Physical Review Focus article in June 2001 and this article is reproduced in the Epilogue. Appendix A contains a sketch of the derivation of the mean-field approximation to the thermodynamic potential for the hadronic EOS used in Chapter 2, Appendix B presents a detailed discussion of neutrino-quark scattering and some useful integrals used in Chapter 3, and Appendix C gives the derivation of the thermodynamic potential in the mean-field approximation used in Chapter 5.

Chapter 2

Quark-Hadron Phase Transitions in Young and Old Neutron Stars

In this chapter, we analyze the structure of young and old neutron stars that contain quarks and indicate what effect quarks might make on observations, in particular, observations of neutrino emissions. When a neutron star is born, the neutrinos produced by electron capture in the beta-equilibrated matter are prevented by their short mean free paths from leaving the star on dynamical timescales. The number of leptons per baryon that remain trapped is approximately 0.4, the precise value depending on the efficiency of electron capture reactions during the gravitational collapse of the progenitor star. On a timescale of 10–20 seconds, the neutrinos diffuse from the star, but leave behind much of their energy which causes significant heating of the ambient matter [11, 57]. Entropies per baryon of about 2 (in units of the Boltzmann constant k_B), and temperatures in the range 30–50 MeV, can generally be achieved in the inner 50% of the star's core. This is to be compared to core entropies of approximately 1 which exist in the initial configuration. Following the heating, the star cools by radiating neutrino pairs of all flavors, and temperatures fall to below 1 MeV within minutes. Recent calculations [12, 66] have verified this general scenario for a variety of equations of state (EOS) and assumptions about the composition of high-density matter.

Compared to cold neutron stars, the appearance of quarks is suppressed in a proto-neutron star (PNS) because of its high lepton number content [9]. As the neutrinos leak out of a PNS, however, the central density of the star increases and the threshold density for the appearance of quarks decreases. Previous studies [9] have shown that the maximum mass supported by neutrino-rich matter is larger than that supported by neutrinoless matter if quarks appear. This gives rise to the possibility that some PNSs might become metastable [10, 58, 67], which would occur if the PNS mass lies within this range of maximum

masses. When the maximum mass decreases below the PNS mass, after most of the neutrinos have diffused from the star, a collapse to a black hole ensues.

The new features of our study are to 1) include both the effects of trapped neutrinos and finite temperature, 2) examine the role of the quark model by employing both the traditional MIT bag model and the Nambu–Jona-Lasinio (NJL) quark Lagrangian, 3) explore the effects of stiffness of the hadronic interactions on the quark-hadron transition, 4) study the effect of hyperons, and 5) delineate the phase diagram in the lepton number–baryon number density plane, appropriate for PNS studies.

2.1 Thermodynamics

2.1.1 Hadronic phase

To model the hadronic phase, we use a field-theoretical description, in which baryons interact via the exchange of σ-, ω-, and ρ- mesons, extended to include hyperons. Specifically, we follow the approach of Müller and Serot [32] (hereafter MS). For densities lower than 0.08 fm^{-3}, we use the zero-temperature EOS of Negele and Vautherin [21], and for densities lower than 0.001 fm^{-3} we use the Baym-Pethick-Sutherland zero-temperature EOS [25]. Since the maximum mass and central densities of neutron stars depend only marginally on the low-density EOS, the assumption of zero-temperature for this low-density matter is satisfactory. The MS Lagrangian is

$$\begin{aligned}
\mathcal{L} &= \sum_B \bar{B}\left(i\gamma^\mu\partial_\mu - g_{\omega B}\gamma^\mu\omega_\mu - g_{\rho B}\gamma^\mu \mathbf{b}_\mu\cdot\mathbf{t} - M_B + g_{\sigma B}\sigma - \mu_B\gamma_0\right)B \\
&- \frac{1}{2}m_\sigma^2\sigma^2 + \frac{1}{2}\partial_\mu\sigma\partial^\mu\sigma - \frac{\kappa}{3!}\sigma^3 - \frac{\lambda}{4!}\sigma^4 \\
&+ \frac{1}{2}m_\omega^2\omega^\mu\omega_\mu - \frac{1}{4}F_{\mu\nu}F^{\mu\nu} + \frac{\zeta}{4!}g_\omega^4\left(\omega^\mu\omega_\mu\right)^2 \\
&+ \frac{1}{2}m_\rho^2\mathbf{b}^\mu\mathbf{b}_\mu - \frac{1}{4}\mathbf{B}_{\mu\nu}\mathbf{B}^{\mu\nu} + \frac{\xi}{4!}g_\rho^4\left(\mathbf{b}^\mu\mathbf{b}_\mu\right)^2 + \mathcal{L}_\ell\,, \qquad (2.1)
\end{aligned}$$

where the sum over B is a sum over all nucleons and hyperons, and $\mathcal{L}_\ell$ represents the sum of the Dirac Lagrangians for all of the leptons (electrons, muons and neutrinos). The values of κ, λ, $g_{\rho N}$, $g_{\sigma N}$, and $g_{\omega N}$ are set by matching the equilibrium nuclear density ($n_0 = 0.16$ fm^{-3}), binding energy ($E_b = -16$ MeV), compressibility ($K_0 = 250$ MeV), nucleon effective mass ($M_0^* = 0.6M$), and symmetry energy ($e_{sym} = 35$ MeV) at n_0. The remaining two parameters, ξ and ζ, associated with non-linear vector and isovector interactions, control the stiffness of the hadronic EOS at supernuclear densities. Larger values of

either parameter tend to soften the EOS. The acceptable ranges for ζ and ξ, based on considerations of naturalness, are $0 \leq \xi \leq 1.5$ and $0 \leq \zeta \leq 0.06$ [32].

We include the Λ, Σ^+, Σ^0, Σ^-, Ξ^0, and Ξ^- hyperons and ignore the heavier Δ baryon which is too massive to affect our results. We assume that all six hyperon coupling constants with a particular vector meson are equal. Furthermore, the hyperon coupling constants are related to the nucleon–vector meson coupling constants by

$$g_{\sigma H} = x_\sigma \; g_{\sigma N} \,, \qquad g_{\rho H} = x_\rho \; g_{\rho N} \,, \qquad g_{\omega H} = x_\omega \; g_{\omega N} \,. \tag{2.2}$$

Following Glendenning and Moszkowski [68] we assume $x_\rho = x_\sigma = 0.8$. We also take $x_\omega = 0.895$, which follows from the binding energy, -28 MeV, of the Λ hyperon in nuclei [69].

The mean field thermodynamical potential corresponding to the Lagrangian in Eq. (2.1) is given in Appendix A.

2.1.2 Quark phase

The thermodynamic potential of the quark phase is $\Omega = \Omega_{\rm FG} + \Omega_{\rm Int}$, where

$$\frac{\Omega_{\rm FG}}{V} = 2N_c T \sum_{i=u,d,s} \int \frac{d^3p}{(2\pi)^3} \left[\ln\left(1 - f_i\right) + \ln\left(1 - \bar{f}_i\right) \right] \tag{2.3}$$

denotes the Fermi gas contribution arising from quarks. We consider three flavors, $i = u, d, s$ and three colors, $N_c = 3$, of quarks. The distribution functions of fermions and anti-fermions are $f_i = [1 + \exp(\beta(E_i - \mu_i))]^{-1}$ and $\bar{f}_i = [1 + \exp(\beta(E_i + \mu_i))]^{-1}$, where E_i and μ_i are the single particle energy and chemical potential, respectively, of quark of species i. To explore the sensitivity of the quark model, we contrast the results of the MIT bag and the Nambu–Jona-Lasinio (henceforth NJL) models for $\Omega_{\rm Int}$.

In the MIT bag model, the Fermi gas contribution is calculated using current, as opposed to dynamical, quark masses. We will restrict ourselves to the simplest bag model and keep only the constant cavity pressure term. The results are qualitatively similar to what is obtained by including perturbative corrections, if the bag constant B is slightly altered [70].

Several features of the Lagrangian of Quantum Chromo-Dynamics (QCD), including the spontaneous breakdown of chiral symmetry, are exhibited by the Nambu–Jona-Lasinio (NJL) model, which shares many symmetries with QCD. In its commonly used form, the NJL Lagrangian reads

$$\begin{aligned} \mathcal{L} \;=\; & \bar{q}(i\partial\!\!\!/ - \hat{m}_0)q \;+\; G\sum_{k=0}^{8}[\,(\bar{q}\lambda_k q)^2 + (\bar{q}i\gamma_5\lambda_k q)^2\,] \\ & - \; K\,[\,\det{}_f(\bar{q}(1+\gamma_5)q) + \det{}_f(\bar{q}(1-\gamma_5)q)\,]\,. \end{aligned} \tag{2.4}$$

The quark fields for the up, down, and strange quarks are denoted by the spinor q which is an SU(3) vector. The determinant operates over flavor space, $\hat{m}_0$ is the 3×3 diagonal current quark mass matrix, λ_k represents the 8 generators of SU(3), and λ_0 is proportional to the identity matrix. The four-fermion interactions stem from the original formulation of this model [71], while the flavor mixing, determinantal interaction is added to break $U_A(1)$ symmetry [38]. Since the coupling constants G and K are dimensionful, the quantum theory is non-renormalizable. Therefore, an ultraviolet cutoff Λ is imposed, and results are considered meaningful only if the quark Fermi momenta are well below this cutoff. The coupling constants G and K, the strange quark mass $m_{s,0}$, and the three-momentum ultraviolet cutoff parameter Λ, are fixed by fitting the experimental values of f_π, m_π, m_K, and $m_{\eta'}$. We use the values of Ref. [72], namely $\Lambda = 602.3$ MeV, $G\Lambda^2 = 1.835$, $K\Lambda^5 = 12.36$, and $m_{0,s} = 140.7$ MeV, obtained using $m_{0,u} = m_{0,d} = 5.5$ MeV. The subscript "0" denotes current quark masses. Results of the gross properties of PNSs obtained by the alternative parameter sets of Refs. [73] and [39] are similar to the results quoted below. The effects of quark superconductivity in the NJL model will be investigated in Chapter 5.

The vector interactions inherent in the NJL model become evident upon a Fierz transformation of the four-fermion interaction. The strength of these four fermion interactions can be varied as an additional parameter [74]. An increase in the strength of the vector interactions tends to soften the equation of state [75]. Because the contribution to the meson masses from the vector interactions is significantly smaller than that of the original four-fermion interaction [76], the parameters above are often assumed to not change significantly when varying the vector interactions.

In the mean field approximation at finite temperature and at finite baryon density, the thermodynamic potential due to interactions among quarks is given by [39]:

$$\begin{aligned} \frac{\Omega_{\rm Int}}{V} \;=\; & -2N_c \sum_{i=u,d,s} \int \frac{d^3p}{(2\pi^3} \left(\sqrt{m_i^2 + p^2} - \sqrt{m_{0,i}^2 + p^2} \right) \\ & + \; 2G\langle\bar{q}_i q_i\rangle^2 - 4K\langle\bar{q}_u q_u\rangle\langle\bar{q}_d q_d\rangle\langle\bar{q}_s q_s\rangle\,. \end{aligned} \tag{2.5}$$

The derivation of $\Omega_{\rm Int}$ is contained within the results for the thermodynamic potential of superconducting quark matter presented in Eq. (5.5) and derived in Appendix C. In both Eqs. (2.3) and (2.5) for the NJL model, the quark masses are dynamically generated as solutions of the gap equation obtained

by requiring that the potential be stationary with respect to variations in the quark condensate $\langle \bar{q}_i q_i \rangle$:

$$m_i = m_{0,i} - 4G\langle \bar{q}_i q_i \rangle + 2K \langle \bar{q}_j q_j \rangle \langle \bar{q}_k q_k \rangle \ , \tag{2.6}$$

(q_i, q_j, q_k) representing any permutation of (u, d, s). The quark condensate $\langle \bar{q}_i q_i \rangle$ and the quark number density $n_i = \langle q_i^\dagger q_i \rangle$ are given by:

$$\begin{aligned} \langle \bar{q}_i q_i \rangle &= -2N_c \int \frac{d^3p}{(2\pi)^3} \frac{m_i}{E_i} \left[1 - f_i - \bar{f}_i \right] \\ n_i = \langle q_i^\dagger q_i \rangle &= 2N_c \int \frac{d^3p}{(2\pi)^3} \left[f_i - \bar{f}_i \right] . \end{aligned} \tag{2.7}$$

A comparison between the MIT bag and NJL models is facilitated by defining an effective bag pressure in the NJL model to be [77] $B_{eff} = \Omega_{\rm int}/V - B_0$ with $B_0 V = \Omega_{\rm int}|_{n_u=n_d=n_s=0}$ a constant value which makes the vacuum energy density zero. In this way, the thermodynamic potential can be expressed as $\Omega = B_{eff} V + \Omega_{\rm FG}$ which is to be compared to the MIT bag result $\Omega = BV + \Omega_{\rm FG}$. Note, however, that Ω_{FG} in the NJL model is calculated using the dynamical quark masses from Eq. (2.6).

2.1.3 Proto-neutron star matter

Both PNS and neutron star matter are in beta equilibrium, which together with charge conservation implies

$$\mu_e - \mu_{\nu_e} = \mu_\mu - \mu_{\nu_\mu} \, ; \qquad \mu_B = b_i \mu_n - q_i \mu_e + q_i \mu_{\nu_e} \ , \tag{2.8}$$

where b_i and q_i are the baryon number and charge, respectively, of the hadron or quark species i. The initial PNS contains trapped neutrinos, so the electron and muon lepton numbers may be assumed fixed: $Y_{Le} = (n_e + n_{\nu_e})/n_B = 0.4$ and $Y_{L\mu} = (n_\mu + n_{\nu_\mu})/n_B = 0$. We consider three approximate entropies per baryon and lepton concentrations to represent the thermodynamic conditions in an evolving PNS: the initial state ($s = 1, Y_{L_e} = 0.4$), the maximally heated star ($s = 2, Y_{\nu_e} = 0$), and the cold, catalyzed star ($s = 0, Y_{\nu_e} = 0$). Of course, treating the PNS as a monolithic structure of fixed entropy and composition is an oversimplification, and full evolutionary calculations are required to confirm these estimates.

Quarks are assumed to appear by forming a mixed phase with the hadrons satisfying Gibbs' rules for phase equilibrium [53]. Matter in this mixed phase

is in thermal, mechanical and chemical equilibrium, so that

$$\begin{aligned} T^I &= T^{II} , \qquad \mu_i^I = \mu_i^{II} , \text{and} \\ P^I &= P^{II} ; \qquad \mu_n = 2\mu_d + \mu_u \, , \end{aligned} \tag{2.9}$$

where I and II denote the hadronic and quark phases, respectively. The restriction that the pure phases I and II are independently charge neutral is replaced by the condition of global charge neutrality [53]

$$\chi n_c^I + (1 - \chi) n_c^{II} = 0 \, , \tag{2.10}$$

where n_c is the charge density and χ is the volume fraction of the hadronic phase. The energy and entropy densities in the mixed phase can be expressed in terms of the corresponding quantities in the hadronic and quark phases. We ignore surface and Coulomb effects for the structure in the mixed phase so the leptons are everywhere free Fermi gases.

2.2 Results

The EOS for matter with hadrons is constructed with the MS model, and we considered models both with and without hyperons. In addition, we considered models incorporating a range of parameters ζ and ξ. Two quark Lagrangians were selected, the NJL model with parameters given by [72] and the MIT bag model with $150 \leq B/(\text{MeV fm}^{-3}) \leq 250$. The main effects of increasing ζ and ξ are to decrease the maximum mass and radius, but to increase the extent of the mixed phase. However, the choice $\zeta = \xi = 0$ maximizes the quark content of matter *at a given density*, since the hadronic EOS is stiffest for this case. This is illustrated in the left panels of Figure 2.1, which shows the hadron volume fraction χ as a function of density for three representative hadronic parameter sets (neglecting hyperons) for cold matter without neutrinos. The NJL (MIT) quark model is shown in the upper (lower) panel. However, for a given stellar mass, the quark content of a neutron star is actually maximized for the softest parameter set $\zeta = 0.06, \xi = 1.5$, as shown in the right panels of Figure 2.1. This counterintuitive behavior occurs because the central densities achieved for a given stellar mass are greater for a softer EOS. Note that the maximum mass decreases with increasing softness of the hadronic EOS, which is as expected.

A more intuitive behavior results from variations in the parameters of the quark Lagrangian. The parameters of the NJL model are relatively tightly constrained by meson properties in vacuum. However, the MIT bag model

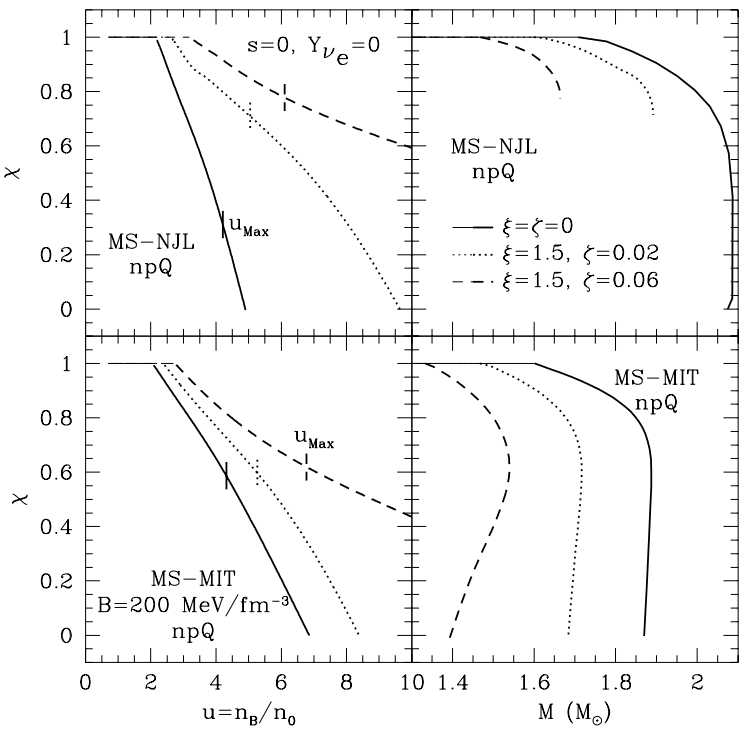

Figure 2.1: Left panels: The volume fraction of hadrons as a function of density in units of n_0 within the quark-hadron mixed phase for cold, catalyzed matter ($s = 0, Y_{\nu_e} = 0$) without hyperons (npQ). Three choices for the parameters ζ and ξ in the Müller-Serot (MS) hadronic Lagrangian are illustrated, and the upper panel refers to the Nambu–Jona-Lasinio (NJL) model and the lower panel to the MIT bag model with $B = 200$ MeV fm^{-3}. The short vertical lines denote the central densities of the maximum mass configuration. The center of the 1.4 $M_\odot$ star is always in a pure hadronic phase. Right panels: The volume fraction of hadrons in the star's center as a function of stellar mass for the same configurations and quark models.

parameter B is only constrained by the requirement that the quark-hadron transition not occur too close to n_0, which implies that B is larger than about 125-150 MeV fm^{-3}. Smaller values for B result in a larger quark content at a given density, a larger quark content for a given stellar mass, and a smaller maximum mass. There is little qualitative change produced by including hyperons.

In the remainder of this chapter, we choose $\zeta = \xi = 0$ for the hadronic parameters and $B = 200$ MeV fm^{-3} for the MIT bag constant. We shall consider in detail four EOSs: hadrons with and without hyperons for the NJL and MIT quark models. The mixed phase of quarks and hadrons can exist in neutron stars at least in the range of 1.2–2 $M_\odot$, depending on the model. Ref. [78] concluded that the mixed phase is unlikely to exist in neutron stars with masses around 1.4 $M_\odot$ neutron stars, using the NJL Lagrangian. However, this result appears to be dependent upon the hadronic interactions.

The pressure of matter as a function of the density in units of n_0, $u = n_B/n_0$, is shown in Figure 2.2 for these four cases. The mixed phase, indicated by thick lines, is marked by a pronounced softening of the EOS, observable as a large decrease in the incompressibility $\partial P/\partial n$ of matter. The introduction of hyperons, or a large trapped neutrino fraction, suppresses the appearance of quarks for both quark models. The reason for this is that the additional contribution to the pressure from the neutrinos or the hyperons is more than canceled by the addition of a degree of freedom to the system. A decrease in the pressure of the hadronic EOS forces the mixed phase to higher densities, because the hadronic pressure is not sufficient to match that of the quark phase until a higher density. Large amounts of trapped neutrinos produce a pronounced net increase in the pressure, however, because the (EOS-softening) transition is shifted to higher densities in all cases.

It is worth noting that the increase in pressure normally observed for finite-temperature matter compared to zero-temperature matter [10, 12] is reversed in the mixed phase produced by quarks. This reversal, which does not occur for a mixed phase with kaon condensation [13], originates in the fact that the phase transition begins at a lower density at finite temperature, so that the EOS softens at an earlier density. Even a small change in the threshold density of appearance for the mixed phase results in a significant net decrease of pressure at a fixed density.

The temperature as a function of baryon density for fixed entropy and net lepton concentration is presented in Figure 2.3, which compares the cases ($s = 1, Y_{L_e} = 0.4$) and ($s = 2, Y_{\nu_e} = 0$) both including and ignoring quarks. The temperature for a multicomponent system in a pure phase can be analyzed

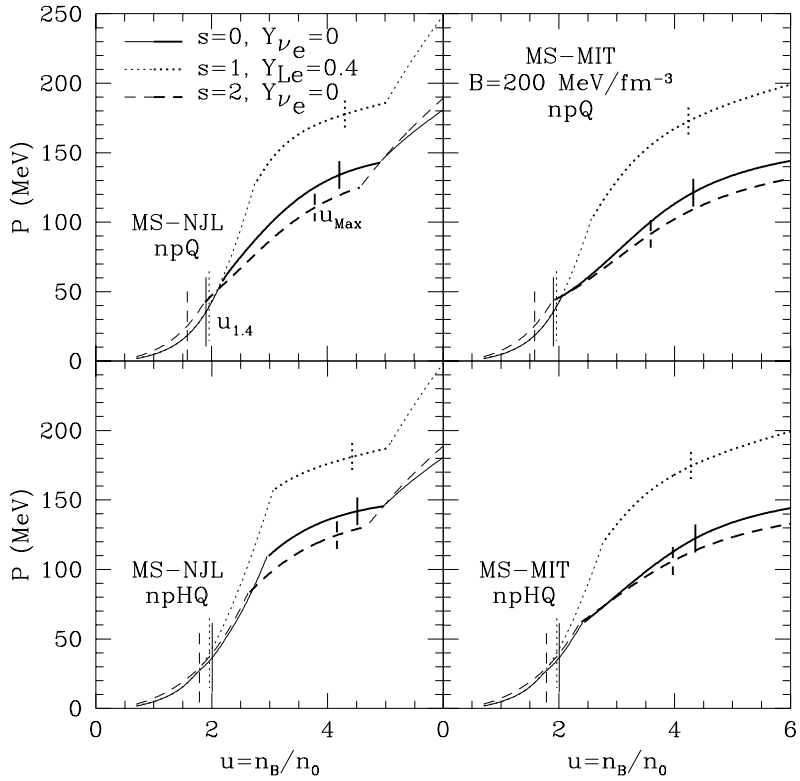

Figure 2.2: Pressure versus density in units of n_0 for three representative snapshots during the evolution of a proto-neutron star. The top (bottom) panels display results without (with) hyperons, and the left (right) panels utilize the NJL (MIT bag) quark EOS. The parameters $\zeta = \xi = 0$ in the Müller-Serot (MS) hadronic Lagrangian are chosen. Bold curves indicate the mixed phase region. The long vertical lines indicate the central densities of a 1.4 $M_\odot$ star and the short vertical lines indicate the central density of the maximum mass star.

with the relation for degenerate Fermi particles

$$T = \frac{s}{\pi^2}\left(\sum_i \frac{\sqrt{p_{F,i}^2 + (m_i^*)^2}}{p_{F,i}^2}\right)^{-1}, \tag{2.11}$$

where m_i^* and p_{F_i} are the effective mass and the Fermi momentum of component i, respectively. This formula is quite accurate since the hadron and quark Fermi energies are large compared to the temperature. The introduction of hyperons or quarks lowers the Fermi energies of the nucleons and simultaneously increases the specific heat of the matter, simply because there are more components. In the case of quarks, a further increase, which is just as significant, occurs due to the fact that quarks are rather more relativistic than hadrons. The combined effects for quarks are so large that, in the case $M_0^* = 0.6M$ shown in Figure 2.3, an actual reduction of temperature with increasing density occurs along an adiabat. The effect is not necessarily as dramatic for other choices of M_0^*, but nevertheless indicates that the temperature will be smaller in a PNS containing quarks than in stars without quarks. The large reduction in temperature might also influence neutrino opacities, which are generally proportional to T^2. However, the presence of droplet-like structures in the mixed phase, not considered here, will modify the specific heat. In addition, these structures may dominate the opacity in the mixed phase [55]. However, a PNS simulation is necessary to consistently evaluate the thermal evolution, since the smaller pressure of quark-containing matter would tend to increase the star's density and would oppose this effect.

The particle concentrations as functions of density are displayed in Figures 2.4 and 2.5 for the four EOSs considered here. The major difference that the choice of quark models produces concerns the concentration of the strange quark. The strange quark (dynamical) mass in the NJL model is much larger, by a factor of 2 to 3, than that assumed in the MIT bag model. This noticeably reduces its chemical potential, and hence its concentration, in the NJL model. The inclusion of hyperons does not produce significant changes to the nucleon or electron concentrations, although the electron concentration begins to fall at the threshold density for the appearance of hyperons which is lower than the low-density boundary of the mixed phase region. The muon concentration is generally much smaller than that of the electron and is omitted from the figures for the sake of clarity. By moving the mixed phase region to higher densities, the inclusion of hyperons, somewhat reduces the width of the mixed phase region. This is not apparent in the figures for the MIT bag case, however, because the mixed phase extends to rather large densities.

The mass-radius trajectories, computed from the standard relativistic stel-

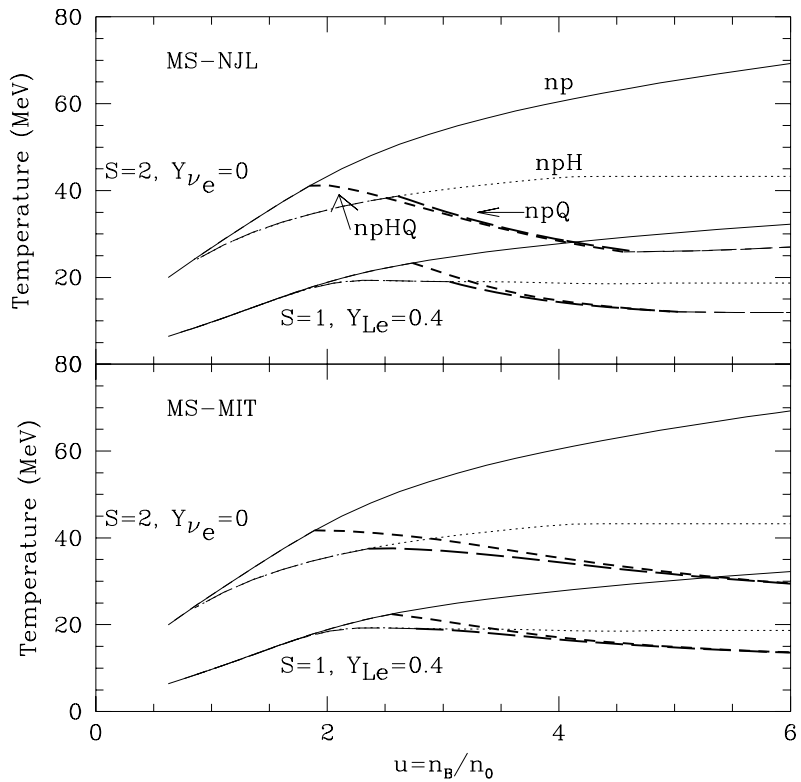

Figure 2.3: Temperature versus density in units of n_0 for two PNS evolutionary snapshots. The upper (lower) panel displays results for the NJL (MIT bag) Lagrangian. The parameters $\zeta = \xi = 0$ in the Müller-Serot (MS) hadronic Lagrangian are chosen. Results are compared for matter containing only nucleons (np), nucleons plus hyperons (npH), nucleons plus quarks (npQ) and nucleons, hyperons and quarks (npHQ). Bold curves indicate the mixed phase region.

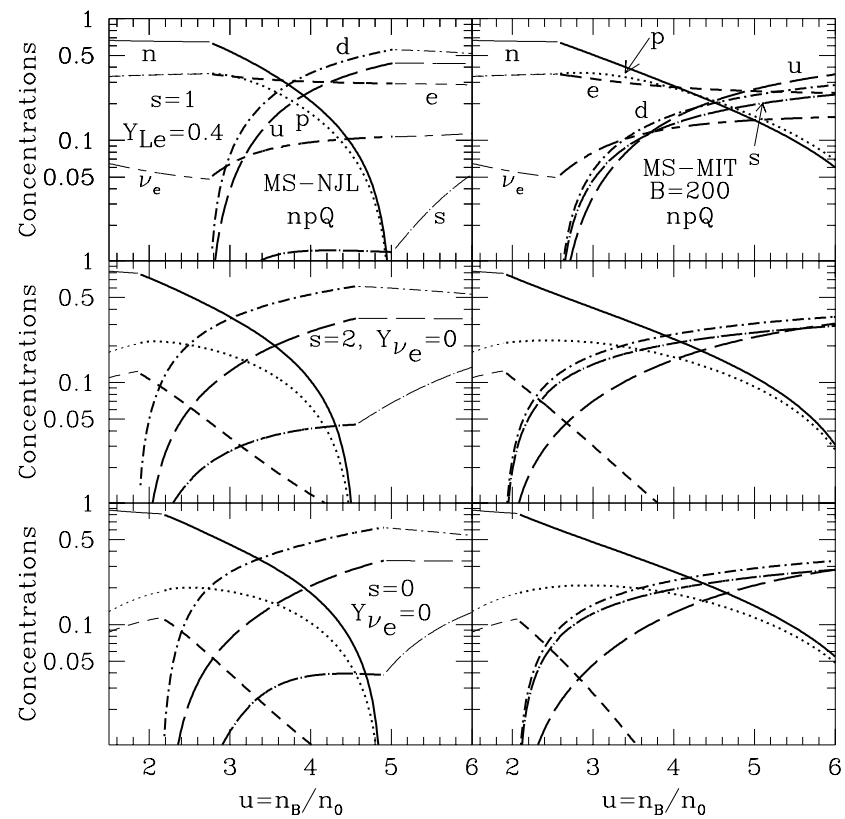

Figure 2.4: The concentrations of hadrons, quarks, and leptons as functions of density in units of n_0. Three representative snapshots during the evolution of a proto-neutron star are displayed. Matter is assumed to contain nucleons and quarks (npQ). The parameters $\zeta = \xi = 0$ in the Müller-Serot (MS) hadronic Lagrangian are chosen. Bold curves indicate the mixed phase region.

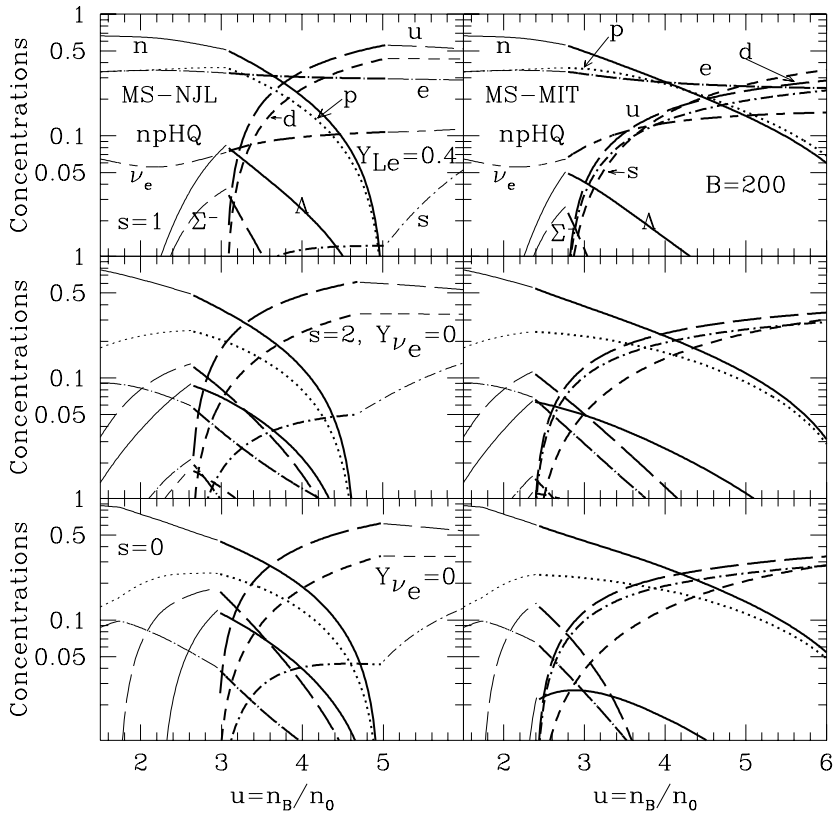

Figure 2.5: The same as Figure 2.4, except that hyperons are included (npHQ).

lar structure equations, are displayed in Figure 2.6 for the four EOSs and for the set of three thermodynamic conditions. Configurations in which the center of the star is in the mixed phase region are shown as bold lines. Although the results displayed are for a single parameterization of the hadronic matter, it is clear that neutron stars containing a mixed phase have a moderate range of masses. This range could be enhanced by altering either the hadronic or the quark matter EOS. The range of masses of stars containing a mixed phase appears to be diminished in the case that hyperons exist, as noted in Refs. [9, 78], but this result is somewhat dependent upon the hyperon coupling constants in addition to the hadronic and quark matter EOSs.

Coinciding with the result in Figure 2.2 that the quark-hadron transition at finite temperature occurs at a lower density than at zero temperature, and thereby reduces the pressure in the mixed-phase region, the neutrino-free stars with $s = 2$ have smaller maximum masses than those for cold $s = 0$ stars. Nevertheless, the pressure in the range $n_0 < n < 1.5n_0$ increases with entropy. This increase in pressure results in larger stellar radii for stars below the maximum mass. The difference of pressures between the $(s = 0, Y_{L_e} = 0.4)$ and $(s = 1, Y_{\nu_e} = 0)$ cases is much smaller, and produces relatively less of a radius change.

It is immediately apparent that in all cases shown, a range of masses are metastable, a condition which exists if the initial PNS configuration has a greater maximum mass than the final configuration [9]. This result was foreshadowed by the results presented in Figure 2.2, in which the pressure for the lepton-rich configuration was much larger in the mixed phase than for the other configurations. In addition, as the neutrinos diffuse from the star, the mixed phase shifts to lower densities and so a greater proportion of the center of the star is in the mixed phase. In the cases shown, the maximum mass occurs when the star's central density is in the mixed phase region.

This last point is highlighted in Figure 2.7 which shows phase diagrams for the mixed phase in the baryon density-neutrino fraction plane. The upper and lower boundaries of the mixed phase region are displayed as bold lines, while the central densities of the maximum mass configurations are shown as light lines. The high-density phase boundaries are always well above the central densities. While in the optimum case, in which the parameters of both the hadronic and quark EOSs are fine-tuned, it is possible for a pure quark core to form if $B < 150$ MeV fm^{-3}, the maximum mass decreases below 1.44 $M_\odot$ if $B < 145$ MeV fm^{-3}. This narrow window, which further decreases or disappears completely if the hadronic EOS is altered, suggests that configurations with pure quark cores may be unlikely. Strange quark stars, in which the pressure of quark matter vanishes at non-zero density,

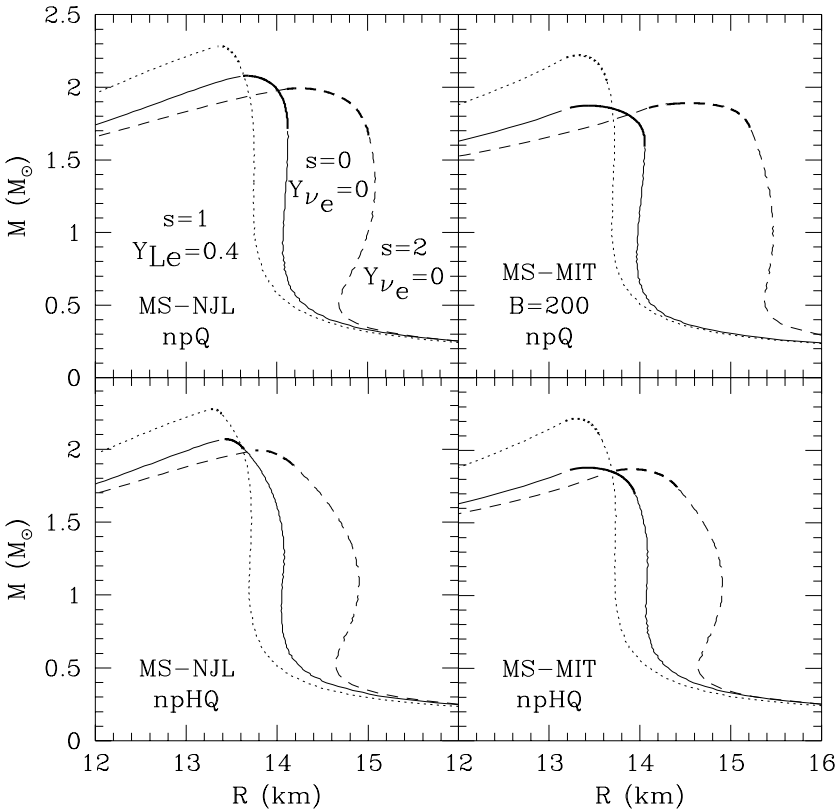

Figure 2.6: The gravitational mass versus radius, for three representative snapshots during the PNS evolution. The left (right) panels are for the NJL (MIT bag) quark EOS, and hyperons are (are not) included in the bottom (top) panels. The parameters $\zeta = \xi = 0$ in the Müller-Serot (MS) hadronic Lagrangian are chosen. Bold lines indicate configurations with a mixed phase at the star's center.

unless the bag constant is very small.

By allowing the parameters of our hadronic EOS to vary within their experimental uncertainties (as for example, using $K = 300$ MeV, $E_{sym} = 30$ MeV, and $n_0 = 0.153$ fm^{-3} and lowering the bag constant to 150 MeV/fm^3), it is possible to construct a neutron star with a pure quark core. In this case, a maximum mass of 1.46 M$_\odot$ is obtained. Pure quark cores result only upon fine-tuning the parameters, and inevitably lead to small maximum masses. Given the constraint that any EOS must be able to support at least 1.44 M$_\odot$, the most accurately measured of the neutron star masses, we conclude that it is unlikely for neutron stars to contain a pure quark core.

2.3 Discussion

In summary, it is possible for a mixed phase to exist in a neutron star of virtually any mass above 1.4 M$_\odot$. Depending upon the EOSs, a mixed phase is more likely to exist in stars larger than 1.5 M$_\odot$. The precise stellar mass above which a mixed phase containing quarks might exist depends on the "softness" of the hadronic EOS and the effective bag pressure of the quark model. Although the quark content of matter at a given density is maximized for stiffer hadronic equations of state, the extent of the mixed phase region in a neutron star of a given mass is maximized for softer hadronic EOSs. We have shown that only in extreme cases could result in star with a pure quark core.

The mixed phase is delayed until most neutrinos have diffused from the star, leading to the possible metastability of PNSs, a robust result which depends only on the existence of quarks in dense matter. Finite temperature permits the quark-hadron transition to occur at slightly lower densities than at zero temperature, but in a newly-formed PNS this effect is swamped by the large trapped neutrino fraction which has the opposite tendency. Furthermore, $\partial T/\partial n \lesssim 0$ along adiabats in the quark-hadron mixed phase, a behavior opposite to that generally found in a mixed phase region containing a kaon condensate. This implies that core temperatures may be significantly lower in stars containing quarks than in those not containing quarks. Neutrino opacities, which are sensitive to temperature, will be affected, but the implications for the emitted neutrino fluxes and temperatures can only be reliably evaluated in the context of a full PNS simulation.

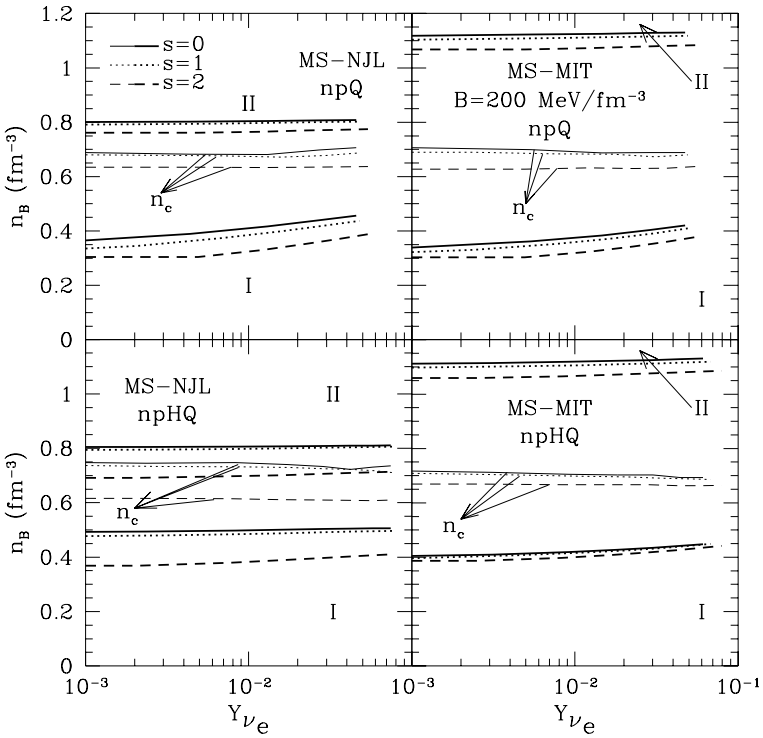

Figure 2.7: The phase diagram of the quark-hadron transition in the baryon number density - neutrino concentration plane for three representative snapshots during the evolution of a proto-neutron star. The left (right) panels are for the NJL (MIT bag) quark EOS, and hyperons are (are not) included in the bottom (top) panels. The parameters $\zeta = \xi = 0$ in the Müller-Serot (MS) hadronic Lagrangian are chosen. The lower- and upper-density boundaries of the mixed phase are indicated by bold curves. The central densities of maximum mass configurations are shown by thin curves.

Chapter 3

Diffusion of Neutrinos in Proto-Neutron Star Matter with Quarks

A general picture of the early evolution of a proto–neutron star (PNS) is becoming well established [10, 11, 12, 66, 79, 80]. Neutrinos are produced in large quantities by electron capture as the progenitor star collapses, but most are temporarily prevented from escaping because their mean free paths are considerably smaller than the radius of the star. During this trapped-neutrino era, the entropy per baryon s is about 1 through most of the star and the total number of leptons per baryon $Y_L = Y_e + Y_{\nu_e} \simeq 0.4$. The neutrinos trapped in the core strongly inhibit the appearance of exotic matter, whether in the form of hyperons, a Bose (pion or kaon) condensate or quarks, due to the large values of the electron chemical potential. As the star cools, the neutrino mean free path increases, and the neutrinos eventually leak out of the star, on a timescale of 20-60 s. During deleptonization, neutrino diffusion heats the matter to an approximately uniform entropy per baryon of 2. If the strongly interacting components consist only of nucleons, the maximum supportable mass increases. In the case that hyperons, a Bose condensate (pion, kaon) or quarks appear in the core as the neutrinos leave, the maximum mass decreases with decreasing leptonic content. Neutron stars which have masses above the maximum mass for completely deleptonized matter are thus metastable, and will collapse into a black hole during deleptonization. Alternatively, if the mass of the neutron star is sufficiently small, the star remains stable and cools within a minute or so to temperatures below 1 MeV as the neutrinos continue to carry energy away from the star.

The way in which this picture is modified when the core of a PNS contains deconfined quark matter is only beginning to be investigated [9, 10, 15, 48]. In his seminal paper, Iwamoto [81] noted that the non-degenerate ν mean free path in cold quark matter is about ten times larger than in nucleonic mat-

ter. We find that in PNS matter, in which quarks appear towards the end of deleptonization, similarly large enhancements persist even up to the largest relevant temperatures ($\sim 30-40$ MeV [15]), inasmuch as quarks remain largely degenerate. On this basis, it can be anticipated that the presence of quark matter increases the neutrino fluxes while simultaneously decreasing the deleptonization time, relative to matter without quarks. In Chapter 4, we explore the possibility that such a change might be detected from a Galactic supernova in current and planned neutrino detectors. This has direct implications for the theoretical understanding of the high-density regime of QCD which is inaccessible to high energy Relativistic Heavy-Ion Collider experiments, and, currently, to lattice QCD calculations at finite baryon density.

To perform detailed simulations of the neutrino signal from a PNS containing quark matter, as has already been done for matter containing nucleons, hyperons and/or a kaon condensate [10, 11, 12, 66, 79, 80], consistent calculations of neutrino interactions in hot lepton-rich matter containing quarks are required. It is most likely that quarks exist in a mixed phase with hadrons [9, 15, 53]. Chapter 2 demonstrated that the temperature of an adiabat decreases as a function of density in a mixed phase of quarks and nucleons. Because $\nu-$cross sections usually scale with T^2, this suggests that the presence of quark matter might influence the neutrino signal of a PNS with quarks. The effects of color superfluidity will be addressed here in Chapter 6.

In this chapter, we calculate the diffusion coefficients of neutrinos in a mixed phase of hadrons and quarks for the temperatures, neutrino degeneracies, and lepton contents likely to be encountered in the evolution of a PNS with quarks. We demonstrate that the cross sections for scattering and absorption of neutrinos by nucleons, leptons, and quarks are reduced to two integrals, whose integrands are products of simple polynomials and thermal distribution functions. The limiting behaviors of the cross sections, for non-degenerate and degenerate neutrinos, respectively, are compared with previous calculations [81] in the case of pure quark matter. For simulations of PNS evolution using the diffusion approximation, diffusion coefficients, which are energy weighted averages of neutrino cross sections, are required for matter in which quarks exist in a mixed phase with hadrons. We examine the relevant diffusion coefficients for two thermodynamic conditions especially germane to PNS evolution. The first situation is when neutrinos are trapped, $s \approx 1$, and the total lepton content of the matter $Y_L = Y_e + Y_{\nu_e}$ (which measures the concentrations of the leptons per baryon) is approximately 0.4. We also consider the situation when neutrinos have mostly left the star and the matter has been diffusively heated ($Y_\nu \approx 0, s \approx 2$). We discuss the impact these results might have upon the evolution of a PNS which contains quarks in a mixed phase.

3.1 Theory

3.1.1 Standard model cross sections

For the $\nu-$energies of interest, the neutral and charged current $\nu-$interactions with the matter in a PNS are well described by a current-current Lagrangian [82]

$$\mathcal{L} = \frac{G_F}{\sqrt{2}} \left(\overline{\psi}_\nu(1)(1-\gamma_5)\psi_{p_3}(3)\right) \left(\overline{\psi}_{p_2}(2)(\mathcal{V}-\mathcal{A}\gamma_5)\psi_{p_4}(4)\right) + \text{H.C.}\,, \tag{3.1}$$

where $\mathcal{V}$ and $\mathcal{A}$ are the vector and axial–vector coupling constants (See Table 1) and $G_F \simeq 1.17$ GeV^{-2} is the Fermi weak coupling constant. The subscripts $i = 1, 2, 3$, and 4 on the four-momenta p_i denote the incoming neutrino, the incoming lepton, baryon or quark, the outgoing neutrino (or electron), and the outgoing lepton, baryon or quark, respectively. The charged current reactions contribute to absorption of neutrinos by baryons or quarks and scattering of neutrinos with leptons of the same generation. The neutral current interactions contribute to scattering of neutrinos with leptons and baryons or quarks. The charged current contribution to neutrino–lepton scattering in the same generation can be transformed into the neutral current form, which modifies the constants $\mathcal{V}$ and $\mathcal{A}$ for that case. For completeness, the values of $\mathcal{V}$ and $\mathcal{A}$ for electron neutrinos are given in Table 1. The corresponding values for reactions with electron anti-neutrinos are obtained by the replacement $\mathcal{A} \to -\mathcal{A}$.

From Fermi's golden rule, the cross section per unit volume (or inverse mean free path) is

$$\begin{aligned} \frac{\sigma}{V} &= g \int \frac{d^3p_2}{(2\pi)^3} \int \frac{d^3p_3}{(2\pi)^3} \int \frac{d^3p_4}{(2\pi)^3} \left[W_{fi} f_2 (1-f_3)(1-f_4)\right. \\ &\quad \left. (2\pi)^4 \delta^4(p_1+p_2-p_3-p_4)\right]\,, \end{aligned} \tag{3.2}$$

where the degeneracy factor g is 6 (3 colors $\times$ 2 spins) for reactions involving quarks while it is 2 (2 spins) for baryons of a single species. The Fermi–Dirac distribution functions are denoted by $f_i = \left[1+\exp\left(\frac{E_i-\mu_i}{T}\right)\right]^{-1}$, where E_i and μ_i are the energy and chemical potential of particle i. The transition probability W_{fi}, summed over the initial states and averaged over the final states, is

$$\begin{aligned} W_{fi} &= \frac{G_F^2}{E_1E_2E_3E_4} \left[(\mathcal{V}+\mathcal{A})^2 (p_1\cdot p_2)(p_3\cdot p_4) + (\mathcal{V}-\mathcal{A})^2 (p_1\cdot p_4)(p_3\cdot p_2)\right. \\ &\quad \left. - \left(\mathcal{V}^2-\mathcal{A}^2\right)(p_1\cdot p_3)(p_4\cdot p_2)\right]\,. \end{aligned} \tag{3.3}$$

	$1+2 \to 3+4$	$\mathcal{V}$	$\mathcal{A}$
	$\nu_e + \mu^- \to \nu_\mu + e^-$	1	1
Charged	$\nu_l + n \to l^- + p$	$\frac{1}{2}\cos\theta_C$	$\frac{1}{2}g_A\cos\theta_C$
current	$\nu_l + d \to l^- + u$	$\cos\theta_C$	$\cos\theta_C$
	$\nu_l + s \to l^- + u$	$\sin\theta_C$	$\sin\theta_C$
	$\nu_e + e^- \to \nu_e + e^-$	$\frac{1}{2} + 2\sin^2\theta_W$	$\frac{1}{2}$
	$\nu_e + \mu^- \to \nu_e + \mu^-$	$-\frac{1}{2} + 2\sin^2\theta_W$	$\frac{1}{2}$
	$\nu_e + n \to \nu_e + n$	$-\frac{1}{2}$	$-\frac{1}{2}g_A$
Neutral	$\nu_e + p \to \nu_e + p$	$\frac{1}{2} + 2\sin^2\theta_W$	$\frac{1}{2}g_A$
current	$\nu_e + u \to \nu_e + u$	$\frac{1}{2} - \frac{4}{3}\sin^2\theta_W$	$\frac{1}{2}$
	$\nu_e + d \to \nu_e + d$	$\frac{1}{2} + \frac{2}{3}\sin^2\theta_W$	$-\frac{1}{2}$
	$\nu_e + s \to \nu_e + s$	$\frac{1}{2} + \frac{2}{3}\sin^2\theta_W$	$-\frac{1}{2}$

Table 3.1: The standard model charged and neutral current vector and axial–vector couplings of neutrinos to leptons, baryons, and quarks; θ_C is the Cabbibo angle ($\cos\theta_C = 0.973$), θ_W is the weak mixing angle ($\sin\theta_W = 0.231$), and $g_A = 1.23$ is the baryon axial–vector coupling constant.

Utilizing $d^3p_i = p_i^2\, dp_i d\Omega_i = p_i E_i\, dE_i d\Omega_i$ and integrating over E_4, Eq. (3.2) may be cast in the form

$$\begin{aligned} \frac{\sigma}{V} &= \frac{gG_F^2}{32\pi^5}\int_{M_2}^{\infty} dE_2 \int_0^{\infty} dE_3\; S\; \frac{E_3}{E_1}|\vec{p}_2||\vec{p}_4|\; \Big[(\mathcal{V}+\mathcal{A})^2 I_a + \\ &\quad (\mathcal{V}-\mathcal{A})^2 I_b + \left(\mathcal{V}^2 - \mathcal{A}^2\right) I_c\Big]\,, \end{aligned} \tag{3.4}$$

where $S = f_2\,(1-f_3)\,(1-f_4)$, M_i is the mass of particle i, and

$$I_a = \int d\Omega_2 d\Omega_3 d\Omega_4\;\; \delta^3\left(p_1+p_2-p_3-p_4\right)(p_1\cdot p_2)\,(p_3\cdot p_4)\,. \tag{3.5}$$

The integrals I_b and I_c are defined similarly to I_a and are given in Appendix B. Explicitly,

$$\begin{aligned} I_a &= \frac{\pi^2}{5p_1p_2p_3p_4}\Big[3\left(P_{\max}^5 - P_{\min}^5\right) - 10\,(A+B)\left(P_{\max}^3 - P_{\min}^3\right) + \\ &\quad 60AB\,(P_{\max} - P_{\min})\Big]\,, \end{aligned} \tag{3.6}$$

where

$$\begin{aligned} 2A &= 2E_1E_2 + p_1^2 + p_2^2,\;\; 2B = 2E_3E_4 + p_3^2 + p_4^2, \\ P_{\min} &= \max\left(|p_1-p_2|, |p_3-p_4|\right),\;\; P_{\max} = \min\left(p_1+p_2, p_3+p_4\right)\,. \end{aligned} \tag{3.7}$$

In the above expression, $p_i \equiv \vec{p}_i$. I_b and I_c are defined to be the same as I_a, but with appropriate replacements:

$$I_b \equiv I_a(p_2 \leftrightarrow p_4, E_2 \leftrightarrow -E_4)\,, \qquad I_c \equiv I_a(p_2 \leftrightarrow p_3, E_2 \leftrightarrow E_3)\,. \tag{3.8}$$

In Eqs. (3.7) and (3.8), $E_4 = E_1 + E_2 - E_3$ and $|\vec{p}_4| = \sqrt{(E_1+E_2-E_3)^2 - M_4^2}$. Eqs. (3.4) through (3.8) are the principal results of this chapter and enable us to compute, for arbitrary conditions of neutrino degeneracy and matter's temperature, the neutrino diffusion coefficients required in simulations of PNSs containing quark matter. We note that similar techniques were employed to calculate $\nu-$emissivities in cold catalyzed neutron stars in Refs. [83, 84].

In limiting cases when the neutrinos are either degenerate or non-degenerate, and the quarks, which are always degenerate in PNSs, are massless, simple analytical expressions for the cross section may be obtained by replacing momenta by Fermi momenta and energies by chemical potentials in the integrals I_a, I_b, and I_c. For the sake of comparing such limits with the general results obtained from Eq. (3.4), we record various limiting forms obtained

earlier in Refs. [81, 85]. In the case of neutrino scattering, explicit derivations and further extensions of these results are given in Appendix B.

(1) *Scattering of degenerate neutrinos:* The result is the same as for neutrino-electron scattering:

$$\frac{\sigma_S}{V} = \frac{G_F^2\mu_2^3}{5\pi^3}\left[(E_1-\mu_1)^2+\pi^2T^2\right]\left(\frac{xE_1}{\mu_2}\right)^{1/2}\times \left[\left(\mathcal{V}^2+\mathcal{A}^2\right)\left(10+x^2\right)+5\left(2\mathcal{V}\mathcal{A}\right)x\right], \tag{3.9}$$

where $x = \min(\mathrm{E}_1,\mu_2)/\max(\mathrm{E}_1,\mu_2)$. Here, and in the following, we have removed the factor $1-f_1 = \left(1+e^{-(E_1-\mu_1)/T}\right)^{-1}$ from [81, 85] to obtain transport mean free paths.

(2) *Scattering of non-degenerate neutrinos:* The inverse scattering mean free path is

$$\frac{\sigma_S}{V} = \frac{G_F^2E_1^3\mu_2^2}{5\pi^3}. \tag{3.10}$$

when it is additionally assumed that μ_2 is large compared to E_1.

(3) *Absorption of degenerate neutrinos*:

$$\frac{\sigma_A}{V} = \frac{2G_F^2\mu_3^3}{5\pi^3\mu_1^2}\left(10\mu_4^2+5\mu_4\mu_3+\mu_3^2\right)\left[(E_1-\mu_1)^2+\pi^2T^2\right]. \tag{3.11}$$

(4) *Absorption of non-degenerate neutrinos*: The general result is greatly simplified by additionally assuming that the quark chemical potentials are modified by perturbative gluon exchange:

$$\frac{\sigma_A}{V} = \frac{16}{\pi^4}\alpha_c G_F^2 p_{F_2}p_{F_3}p_{F_4}\left[E_1^2+\pi^2T^2\right]. \tag{3.12}$$

Representative cross sections from Eq. (3.4) are compared with the limiting forms in Eqs. (3.9)–(3.12) in Fig. 3.1. Degenerate neutrinos are assumed in this figure to have $\mu_\nu \gg T$ and non-degenerate neutrinos are assumed to have $\mu_\nu \approx 0$. In the regions where they were expected to be valid, namely $E_\nu/T \gg 1$ for degenerate absorption and scattering, and also non-degenerate scattering, and $E_\nu \approx T$ for non-degenerate absorption, the limiting forms give adequate representations of the general results. However, significant deviations occur in the cases of non-degenerate absorption when $E_\nu \neq T$, and for degenerate absorption and non-degenerate scattering when $E_\nu \ll T$. The deviation for non-degenerate absorption is due to the neglect of p_ν in the momentum conservation condition in Eq. (3.2) in Ref. [81] (which is appropriate for cold catalyzed stars, but not for hot matter in PNSs), which limits its applicability to the region $E_\nu \approx T$. The other two deviations are simply due to the assumption in Ref. [81] that $E_\nu \gg T$.

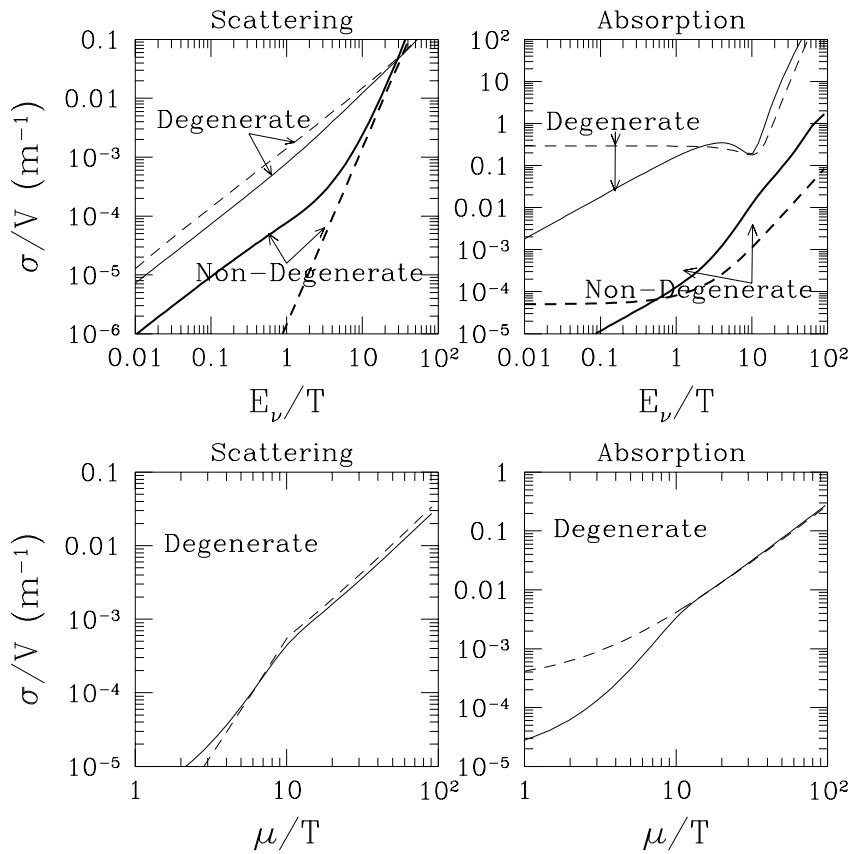

Figure 3.1: ν_e cross sections per unit volume in pure quark matter, for $T = 5$ MeV. Solid lines show complete results from Eq. (3.4), and dashed lines indicate limiting forms from [81]. The labels "Degenerate" and "Non-Degenerate" refer to neutrinos. Upper panels show results for two times nuclear matter density, and the lower panels show results for a neutrino energy of 50 MeV (μ is the chemical potential of the incoming quark).

3.1.2 Diffusion coefficients

The weak interaction timescales of neutrinos are much smaller than the dynamical timescale of PNS evolution, which is on the order of seconds. Thus, until neutrinos enter the semi-transparent region, they remain close to thermal equilibrium in matter. Hence, neutrino propagation may be treated in the diffusion approximation with the differential equations for the flux of energy (F_ν) and lepton number (H_ν) [12]:

$$\begin{aligned} H_\nu &= -\frac{T^2 e^{-\Lambda-\phi}}{6\pi^2}\left[D_4\frac{\partial\left(Te^{\phi}\right)}{\partial r}+\left(Te^{\phi}\right)D_3\frac{\partial\eta(r)}{\partial r}\right] \qquad \text{and} \\ F_\nu &= -\frac{T^3 e^{-\Lambda-\phi}}{6\pi^2}\left[D_3\frac{\partial\left(Te^{\phi}\right)}{\partial r}+\left(Te^{\phi}\right)D_2\frac{\partial\eta(r)}{\partial r}\right], \end{aligned} \tag{3.13}$$

where Λ and ϕ are general relativistic metric functions, $\eta = \mu_\nu/T$ and D_2, D_3, and D_4 are diffusion coefficients decomposed as

$$D_2 = D_2^{\nu_e} + D_2^{\bar{\nu}_e}, \qquad D_3 = D_3^{\nu_e} - D_3^{\bar{\nu}_e}, \qquad D_4 = D_4^{\nu_e} + D_4^{\bar{\nu}_e} + 4D_4^{\nu_\mu}\,. \tag{3.14}$$

The transport of μ and τ neutrinos and anti-neutrinos are well approximated [11] by assuming that they contribute equally to D_4 and are represented by D^{ν_μ}. These coefficients are defined in terms of the energy dependent diffusion coefficient $D^p(E_\nu)$ by

$$D_n^p = \int_0^\infty dx\; x^n D^p(E_1) f(E_1)\left[1-f(E_1)\right]\,, \tag{3.15}$$

where $x = E_1/T$, and the superscript p denotes either the electron neutrino, the anti-electron neutrino, or the μ and τ neutrinos and their antineutrinos. In turn, the energy dependent diffusion coefficient is obtained directly from the cross sections per unit volume through

$$\left(D^p(E_1)\right)^{-1} = \frac{1}{1-f_1}\left[\sum_{\mathrm{r=(p,L)}}\frac{\sigma_r}{V} + \chi\sum_{\mathrm{r=(p,H)}}\frac{\sigma_r}{V} + (1-\chi)\sum_{\mathrm{r=(p,Q)}}\frac{\sigma_r}{V}\right], \tag{3.16}$$

where the (p, L), (p, H), and (p, Q) represent the sum over all the reactions of particle p with leptons, hadrons, or quarks, respectively. The factor $(1-f_1)^{-1}$ ensures detailed balance, and χ is the volume fraction of matter in the hadronic phase.

Note that in the case of scattering, the Pauli blocking factor corresponding to the outgoing neutrino is omitted, since the neutrino distribution function

is not always known a priori unless a full transport scheme is employed. It is possible, however, to devise a simplified scheme [12] in which the dependence on the neutrino distribution function is minimized. Such a scheme is valid only when scattering from light particles (either electrons or quarks) does not dominate the opacity. Our results below show that this requirement is indeed met, because absorption dominates over scattering by a factor of 2 to 5 at all densities interior to the central densities of PNSs investigated here.

3.1.3 EOS of neutron star matter with quarks

We describe neutron star matter at finite density and temperature using the Gibbs phase rules [15, 53]. The conditions of baryon number density and charge conservation in the mixed phase are

$$n_B = \chi n_B^H + (1-\chi)\, n_B^Q, \qquad 0 = \chi n_c^H + (1-\chi)\, n_c^Q + n_c^L\,, \tag{3.17}$$

where n_B and n_c are the baryon number and charge densities, respectively; H, Q, and L denote hadrons, quarks, and leptons. Since the dynamical time scale is much longer than the weak interaction time scale, beta equilibrium implies that the various chemical potentials satisfy the relations

$$\mu_e - \mu_{\nu_e} = \mu_\mu - \mu_{\nu_\mu}\,; \qquad \mu_B = b_i\mu_n - q_i(\mu_e - \mu_{\nu_e})\,, \tag{3.18}$$

where b_i and q_i are the baryon number and electric charge of the hadron or quark of species i. When the neutrinos are trapped, the electron lepton number $Y_L = (n_e + n_{\nu_e})/n_B$ is initially fixed at a value $\simeq 0.4$ as suggested by collapse calculations.

Hadronic matter is described using a field-theoretical description in which nucleons interact via the exchange of σ, ω, and ρ mesons. The meson-nucleon couplings and the couplings of the σ self-interaction terms are determined by reproducing the empirical properties of nuclear matter, $E_B = -16.0$ MeV, $M^*/M = 0.6$, $K = 250$ MeV, $a_{sym} = 32.5$ MeV, and $n_0 = 0.16$ fm^{-3}. Quark matter is described using the MIT Bag model, with a bag constant of $B = 200$ MeV/fm^3. (Similar results are obtained with four-quark interactions in the Nambu–Jona-Lasinio model [15].) The mixed phase is assumed to be homogeneous. For more details of the calculation of the EOS, see Chapter 2.

3.2 Results

3.2.1 Cross sections of neutrino-quark reactions

The cross sections per unit volume (or inverse mean free paths) for ν_e scattering and absorption are shown in Fig. 3.2 for the two stages of PNS evolution described before. It is important to recall that these curves are drawn under conditions of fixed entropy. (Constant entropy adiabats shown in Fig. 2.3 of Chapter 2 are helpful to gain insights into the behavior of the cross sections shown here.) The individual contributions from the different reactions in the pure nucleon and quark phases (thin lines) and in the mixed phase (thick lines) are marked in this figure. The vertical dashed lines show the central densities of $1.4\mathrm{M}_\odot$ and the maximum mass configurations, respectively. Notice that quarks exist only in the mixed phase; the pure quark phase occurs at densities above the central densities of maximum mass stars in all cases shown here.

In general, for a given density and temperature, the pure quark-phase opacity (or equivalently the cross section per unit volume) is less than that of hadrons due to the former's smaller matrix elements sampled by a relativistic phase space. In addition, for a given entropy and density, pure quark matter favors a lower temperature than hadronic matter [15]. It is natural, therefore, that within the mixed phase region of hadrons and quarks, the net cross section per unit volume either flattens or decreases with increasing density. The reduction of opacities from that of the pure hadronic phase is enhanced in the $\nu-$free case, reflecting the more extreme decrease of temperature across the mixed phase region in that case [15]. The precise density dependence of the net neutrino opacity depends upon the details of the mixed phase.

Note that the total absorption cross section is larger than the scattering cross section for both degenerate and nondegenerate situations. As discussed above, this justifies our approximate treatment of scattering in the calculation of the diffusion coefficients.

The diffusion coefficients most relevant for the PNS simulations, in matter with and without a mixed phase of hadrons and quarks, are D_2 and D_4, and these are shown in Fig. 3.3. Insofar as absorption dominates scattering, the behavior of these coefficients can be understood qualitatively by utilizing the limiting forms for neutrino absorption in the degenerate (Eq. (3.11)) and nondegenerate (Eq. (3.12)) cases, respectively. The actual behavior is somewhat more complicated, but this assumption will suffice for a qualitative interpretation of Fig. 3.3. In this case, the leading behaviors may be extracted to

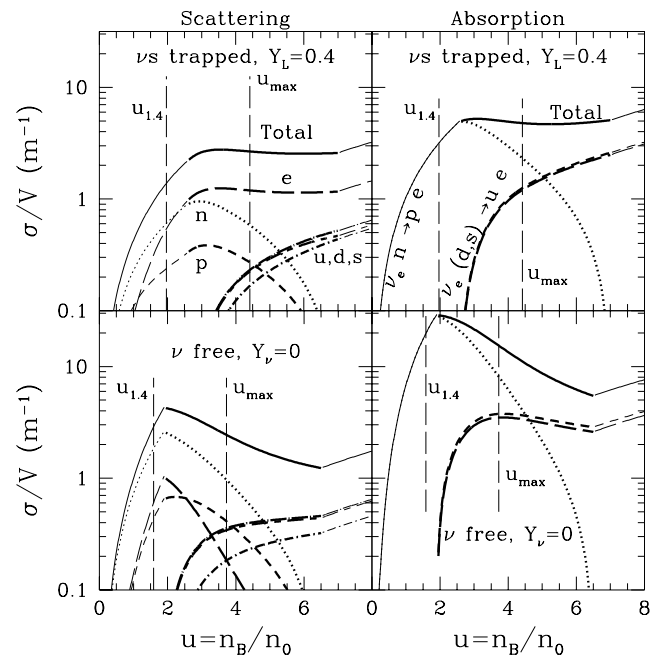

Figure 3.2: ν_e cross sections with various particles in matter containing a mixed phase of quarks and hadrons ($n_0 = 0.16$ fm^{-3}). The left panels show scattering cross sections for neutrinos with the indicated incoming hadrons, quarks, or leptons. Thick lines show the extent of the mixed phase region. The right panels show absorption cross sections on nucleons and quarks. The upper panels correspond to the neutrino-trapped era when $s = 1$ and $Y_L = 0.4$, and the lower panels to the time following deleptonization when $s = 2$ and $Y_\nu = 0$. The vertical dashed lines labelled $u_{1.4}$ and u_{max} indicate the central densities of a $M_G = 1.4$ M$_\odot$ star and the maximum mass star ($M_G = 2.22$ M$_\odot$ for the upper panels and $M_G = 1.89$ M$_\odot$ for the lower panels), respectively.

be

$$D_2 \propto \lambda(\mu_\nu/T)(\mu_\nu/T)^2 \qquad \text{and} \qquad D_4 \propto \lambda(\mu_\nu/T=0)\,, \tag{3.19}$$

where the mean free path $\lambda = (\sigma/V)^{-1}$. In these equations, D_2 is evaluated under conditions of extreme neutrino degeneracy and D_4 is evaluated assuming that $\mu_\nu = 0$. Thus, both D_2 and D_4 should simply reflect the inverse behavior of the cross section per unit volume, which decreases with increasing density in the pure phases, but increases within the mixed phase region.

Concerning the evolution of a PNS, we expect that the initial star, which is lepton rich, will not have an extensive mixed phase region. Only after several seconds of evolution will quark matter appear. In the newly-formed mixed phase region, the neutrino opacity will be substantially smaller than in the case in which a mixed phase region does not appear. However, due to the large $\nu-$optical depth of the PNS, neutrinos remain trapped, and no significant effect on emergent neutrino luminosities is expected at early times. As the star evolves, however, the relatively larger increase in opacity (note the increases in D_4 relative to D_2) and the growing extent of the mixed phase region eventually allows a larger flux of neutrinos, and thereby a more rapid evolution.

In summary, we have calculated neutrino opacities for matter containing quarks for the temperatures, neutrino degeneracies and lepton contents relevant for PNS simulations, employing Gibbs phase rules to construct a mixed hadron-quark phase. We find that, in the presence of quarks, neutrinos have a significantly smaller opacity and hence larger diffusion coefficients than those in purely hadronic matter at similar densities. These differences may have an observable impact on the neutrino flux from PNSs containing quark matter, but these differences are not expected to become apparent until the PNS is 10–20 s old. Simulations of PNSs with a mixed phase of hadrons and quarks are under investigation [80]. The influence of heterogeneous structures [54, 55] and superfluidity [48] in matter will be addressed in future work.

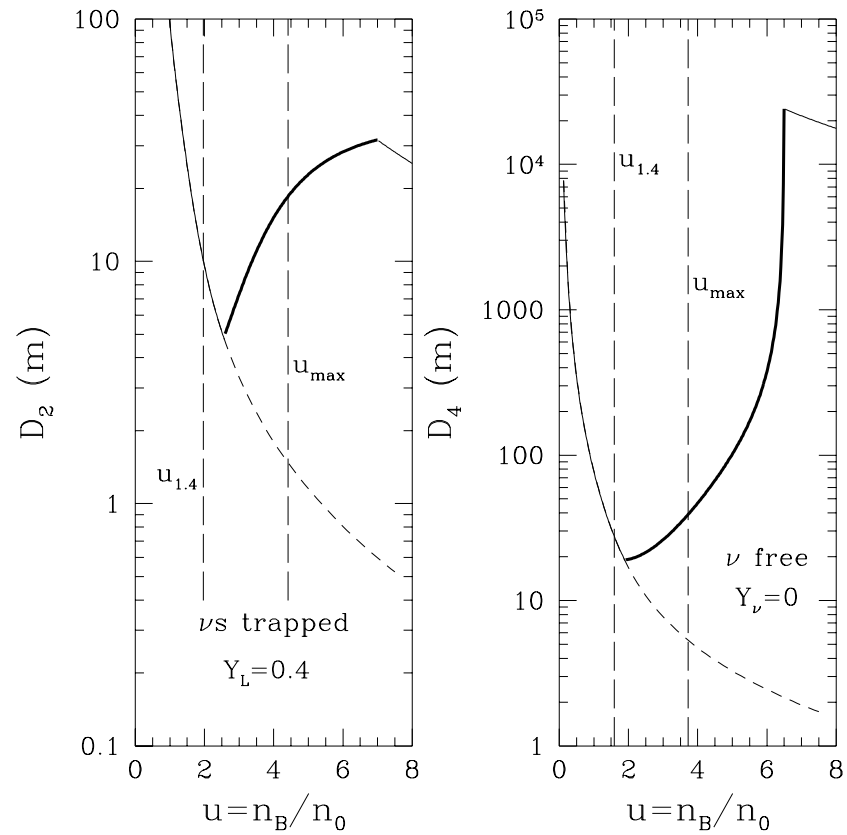

Figure 3.3: Diffusion coefficients for the neutrino-trapped era (left panel) and hot deleptonized era (right panel). Thick lines show the extent of the mixed phase. Solid lines correspond to matter with a mixed phase, and dashed lines to matter containing only nucleons. The vertical dashed lines have the same meaning as in Fig. 2.

Chapter 4

Evolution of Quark Proto-Neutron Stars with Quarks

A proto-neutron star (PNS) is born following the gravitational collapse of the core of a massive star, in conjunction with a successful supernova explosion. During the first tens of seconds of evolution, nearly all ($\sim 99\%$) of the remnant's binding energy is radiated away in neutrinos of all flavors [11, 12, 80]. The $\nu-$luminosities and the evolutionary timescale are controlled by several factors, such as the total mass of the PNS and the $\nu-$opacity at supranuclear density, which depends on the composition and equation of state (EOS). One of the chief objectives in modeling PNSs is to infer their internal compositions from $\nu-$signals detected from future supernovae like SuperK, SNO and others under consideration, including UNO [86].

4.1 Exotic Phases in Dense Matter

In their landmark paper, Collins and Perry [87] noted that the superdense matter in neutron star cores might consist of weakly interacting quarks rather than of hadrons, due to the asymptotic freedom of QCD [88, 89, 90]. The appearance of quarks causes a softening of the EOS which leads to a reduction of the maximum mass and radius [91]. In addition, quarks would alter $\nu-$emissivities and thereby influence the surface temperature of a neutron star [92] during the hundreds of thousands or millions of years that they might remain observable with such instruments as HST, Chandra and XMM. Quarks would also alter the spin-down rates of neutron stars [93].

Many calculations of dense matter predict the appearance of other kinds of exotic matter in addition to quarks: for example, hyperons or a Bose (pion, kaon) condensate [10, and references therein]. An important question is whether or not ν observations from a supernova could reveal the presence

of such exotic matter, and further could unambiguously point to the appearance of quarks. The detection of quarks in neutron stars would go a long way toward the delineation of QCD at finite baryon density which would be complementary to current Relativistic Heavy Ion Collider experiments, which largely address the finite temperature, but baryon-poor, regime. It would have dramatic consequences for strong interaction physics in determining the EOS and transport properties of dense matter.

4.2 Metastability and Black Hole Formation

An important consequence of the existence of exotic matter in neutron stars (in whatever form, as long as it contains a negatively charged component), is that a sufficiently massive PNS becomes metastable [9, 10, 58, 67, 94, 95, 96]. After a delay of up to 100 s, depending upon which component appears, a metastable PNS collapses into a black hole [12, 80]. The collapse to a black hole proceeds on a free-fall timescale of less than a millisecond [12, 97], much shorter than ν diffusion times, and the neutrinos still trapped in the inner regions cannot escape. Such an event should be straightforward to observe as an abrupt cessation of ν flux when the instability is triggered [98].

The evolution of the PNS in the so-called Kelvin-Helmholtz phase, during which the remnant changes from a hot, $\nu-$trapped, and lepton-rich object to a cold and $\nu-$free star, occurs in near-hydrostatic equilibrium. The $\nu-$matter interaction timescales are much smaller than the dynamical timescale of PNS evolution, which is of the order of seconds. Thus, until neutrinos enter the semi-transparent region at the edge of the star, they remain close to thermal equilibrium with matter, and may be treated in the diffusion approximation [11, 12, 80].

In this chapter we provide a benchmark calculation with quarks by solving the general relativistic ν transport and hydrostatic equations (see [12, 80]), and then compare our results with those of our previous work in which other compositions were studied. In addition, we assess the prospects of observing PNS metastability and its subsequent collapse to a black hole through observations in current and planned detectors.

4.3 Equation of State and Neutrino Opacity

The essential microphysical ingredients in our study are the EOS of dense matter and its associated ν opacity. We begin by considering two generic

compositions: charge-neutral, beta equilibrated matter containing (i) nucleons only (np) and (ii) nucleons with quark matter (npQ). In the npQ case, a mixed phase of baryons and quarks (pure quark matter exists only for very large baryon densities, except for extreme choices of model parameters) is constructed by satisfying Gibbs' phase rules for mechanical, chemical and thermal equilibrium [53]. The EOS of baryonic matter is calculated using a field-theoretic model at the mean field level [32]. The results reported with this EOS are quite general, as we verified by alternatively using a potential model approach [10]. The quark matter EOS is calculated using a MIT bag-like model (similar results are obtained with the Nambu–Jona-Lasinio quark model). The details of the EOS are given in Chapter 2. We use ν opacities [16, 62] consistent with the EOS (see Chapter 3). When quarks appear, the ν absorption and scattering cross sections dramatically decrease, the precise reduction being sensitive to the thermodynamic conditions in the mixed phase.

4.4 Examples of Results

Fig. 4.1 shows the evolutions of some thermodynamic quantities at the center of npQ stars of various, fixed, baryonic masses (M_B). In the absence of accretion, M_B remains constant during the evolution, while the gravitational mass M_G decreases. With the EOS utilized, stars with $M_B \lesssim 1.1$ $M_\odot$ do not contain quarks and those with $M_B \gtrsim 1.7$ $M_\odot$ are metastable. The latter value is ~ 0.05 $M_\odot$ larger than the maximum mass for cold, catalyzed npQ matter, because the maximum mass of cold $\nu-$free npQ matter is this much less than that of hot $\nu-$trapped matter [16]. Generally, due to the high lepton (ν) content initially present in the PNS, the electron chemical potential at the center is too large for quarks to exist. For sufficiently massive stars, quarks eventually appear after a certain amount of ν loss occurs. For the $M_B = 1.6$ $M_\odot$ star, for example, quarks appear after about 15 s (indicated by a diamond). Thereafter, the star's central density increases for a further 15-20 s, until a new stationary state with a quark-hadron mixed phase core is reached (for stable stars) or for $M_B \gtrsim 1.7$ $M_\odot$, instability occurs (indicated by asterisks). It is interesting that for this EOS the lifetimes for all masses are restricted to the range 10–30 s, and slowly decrease with increasing mass. The appearance of quarks is accompanied by an increase in Y_ν because of the depletion of electrons; for the largest masses, the increase is very large.

To point out the major differences one might observe between the np and npQ cases, we have estimated the $\bar{\nu}_e$ count rate in the SuperK detector in

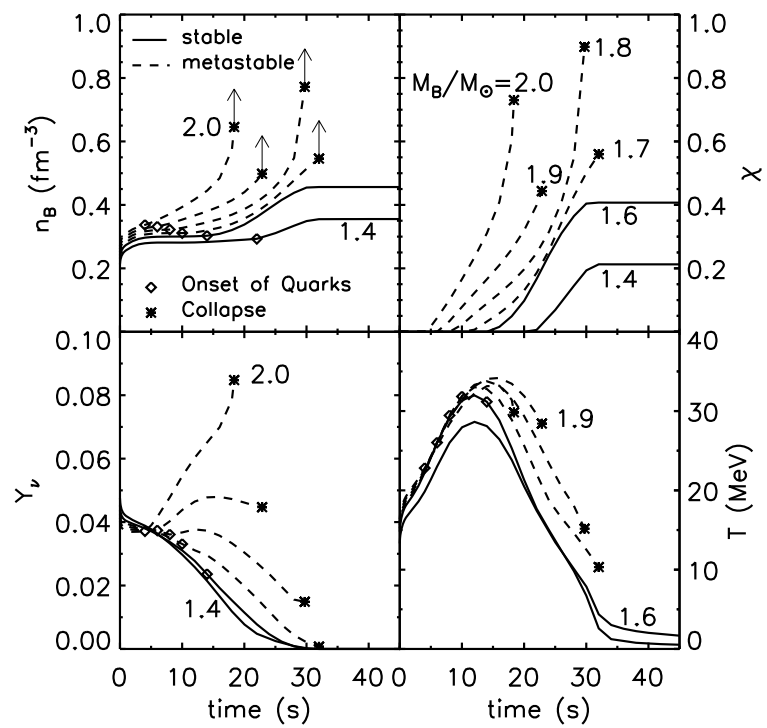

Figure 4.1: Evolutions of the central baryon density n_B, ν concentration Y_ν, quark volume fraction χ and temperature T for different baryonic masses M_B. Solid lines correspond to stable stars; stars with larger masses are metastable (dashed lines). Diamonds indicate when quarks appear at the star's center, and asterisks denote when metastable stars become gravitationally unstable.

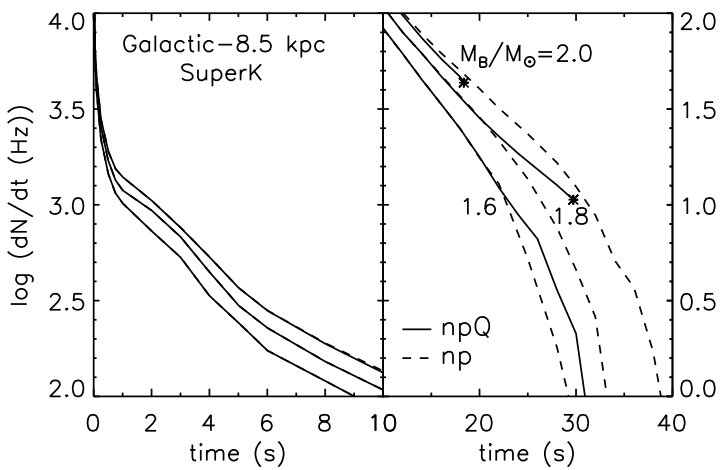

Figure 4.2: A comparison of $\bar{\nu}_e$ count rates expected in SuperK from a PNS containing either *np* or *npQ* matter. The left panel shows times less than 10 s, while the right panel shows times greater than 10 s.

Figure 4.2. For this estimate, we assumed the total ν luminosity from a PNS at 8.5 kpc distance, corresponding to a Galactic supernova, was equally divided among the six ν species. The ν energy spectra were assumed to be Fermi-Dirac with zero chemical potential and a temperature corresponding to the matter temperature in the PNS where the ν optical depth was approximately unity. The precise procedure is described in Refs. [12, 80]. It is difficult to discern much difference in the early ($t < 10$ s) count rates from *np* and *npQ* stars. For stars with $M_B < 1.7$ $M_\odot$, this is because quarks have not yet appeared. For more massive stars, the fact that neutrinos are strongly trapped inhibits any discriminatory signal from reaching the surface before this time. The signals at later times ($t \lesssim 25$s), however, are substantially larger for the *npQ* case, due to the decrease in $\nu-$opacity of *npQ* matter and the increased binding energy of *npQ* stars. Most importantly, the $\nu-$signal from metastable *npQ* stars halts abruptly when the instability occurs. Qualitatively, these features are also found for *npH* and *npK* stars [12, 80].

We compare ν signals observable with different detectors in Fig. 4.3, which displays the ν light curves as a function of M_B for *npQ* stars. The two upper shaded bands correspond to estimated SN 1987A (50 kpc distance) detection limits with KII and IMB, and the lower bands correspond to estimated detection limits in SNO, SuperK, and UNO, for a Galactic supernova (8.5 kpc distance). The detection limits have been set to a count rate $dN/dt = 0.2$ Hz [80]. It is possible that this limit is too conservative and could be lowered with identifiable backgrounds and knowledge of the direction of the signal. The width of the bands represents the uncertainty in the $\bar{\nu}_e$ average energy due to the flux-limited diffusion approximation [12, 80]. We conclude that it should be possible to distinguish between stable and metastable stars, since the luminosities when metastability is reached are always above conservative detection limits.

The drop in ν luminosity for stable stars is associated with the end of the Kelvin-Helmholtz epoch when the PNS is becoming optically thin. This portion of the ν light curve is approximate due to the breakdown of the diffusion approximation. It is an apparent coincidence that this occurs simultaneously with the collapse of the lower mass metastable stars.

Our choice of bag constant, $B = 150$ MeV fm^{-3}, in conjunction with the baryonic EOS we used, was motivated to maximize the extent of the quark matter phase in a cold neutron star, and was limited by the necessity of producing a maximum mass cold star in line with accurate observational constraints ($M_G = 1.444$ $M_\odot$). Increasing B, or employing an alternative quark EOS that otherwise produces a larger maximum mass, delays the appearance of quarks and raises the metastability window to larger stellar masses. Necessarily, this

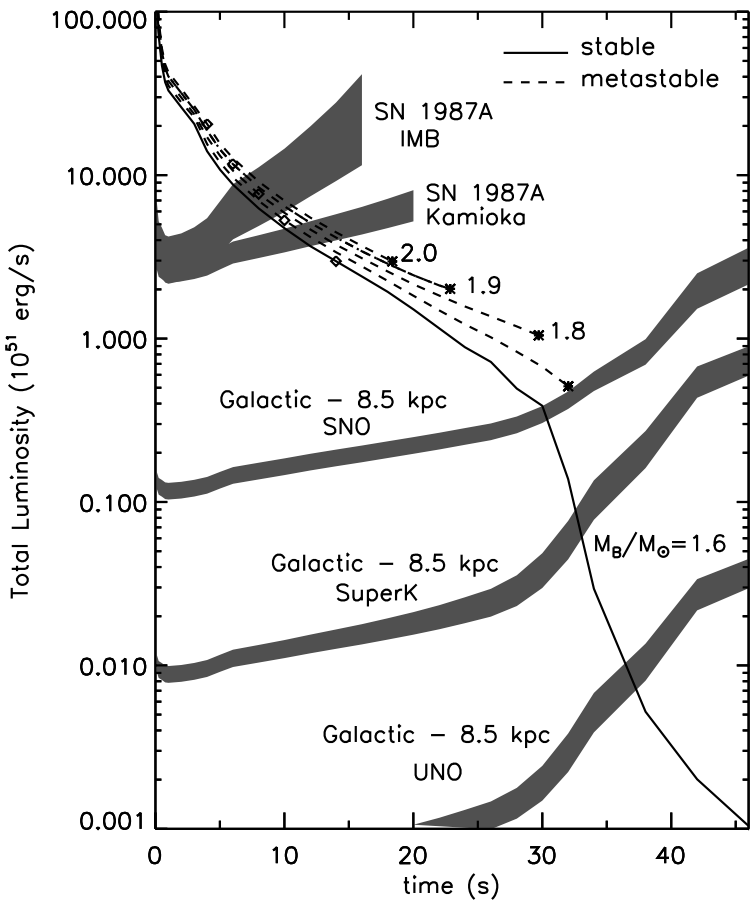

Figure 4.3: The total ν–luminosity for npQ stars of various baryon masses. Shaded bands illustrate the limiting luminosities corresponding to count rates of 0.2 Hz for the indicated supernovae in some detectors.

results in an increased timescale for metastability for a given mass, and a lower ν luminosity when metastability occurs. Fig. 4.4 shows the relation between time to instability and M_B for the original case ($B = 150$ MeV fm^{-3}, thick solid curve) and a case with $B = 200$ MeV fm^{-3} (thin solid curve), in which the maximum gravitational mass of a cold neutron star is about 1.85 $M_\odot$. For the latter case, the metastability timescales lie in a narrow range 40–45 s. These, and the metastability masses, are both larger than obtained for $B = 150$ MeV fm^{-3} and have narrower ranges. Further increases in B diminish the size of the instability window, because the appearance of quarks is shifted to progressively larger densities.

Figure 4.4 also compares the metastability time-M_B relation found for matter containing hyperons (npH, dashed lines [12]) or matter with kaons (npK, dotted line [80]) instead of quarks. All three types of strange matter are suppressed by trapped neutrinos [10, 15], but hyperons always exist in npH matter at finite temperatures and the transition to quark matter can occur at lower densities than that for very optimistic kaon cases [80]. Thus, the metastability timescales for npH matter can be very short, and those for npK matter are generally larger than for npQ matter. Note the relatively step dependence of the metastability time with M_B for npH stars, which decreases to very small values near the maximum mass limit of hot, lepton-rich, stars. The thick npH and npQ lines, as well as the npK line, represent minimum metastability times for a given M_B as discussed above. The thin npQ and npH lines are for EOSs with larger cold, catalyzed maximum mass.

4.5 Implications

Clearly, the observation of a single case of metastability, and the determination of the metastability time alone, will not necessarily permit one to distinguish among the various possibilities. Only if the metastability time is less than 10–15 s, could one decide on this basis that the star's composition was that of npH matter. However, as in the case of SN 1987A, independent estimates of M_B might be available [99, 100]. In addition, the observation of two or more metastable neutron stars might permit one to differentiate among these models.

We have focused on times longer than approximately 1 s after core bounce, after which effects of dynamics and accretion become unimportant. Studies of the ν signal during the first second, during which approximately 1/3 of the energy is emitted, and at late times, as the star becomes optically thin to neutrinos, requires more accurate techniques for ν transport. In addition,

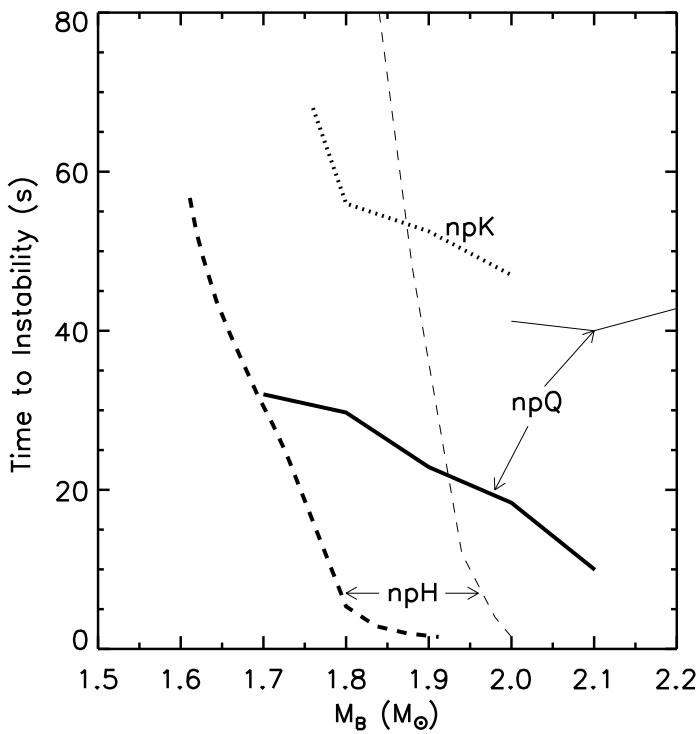

Figure 4.4: Lifetimes of metastable stars versus the PNS M_B for various assumed compositions. Thick lines denote cases in which the maximum masses of cold, catalyzed stars are near $M_G \simeq 1.45$ $M_\odot$, which minimizes the metastability lifetimes. The thin lines for the *npQ* and *npH* cases are for EOSs with larger maximum masses ($M_G = 1.85$ and 1.55 $M_\odot$, respectively).

the earliest time periods require the incorporation of hydrodynamics [101, 102, 103, 104, 105].

Our conclusions are that (1) the metastability and subsequent collapse to a black hole of a PNS containing quark matter, or other types of matter including hyperons or a Bose condensate, are observable in current and planned ν detectors, and (2) discriminating among these compositions may require more than one such observation. This highlights the need for breakthroughs in lattice simulations of QCD at finite baryon density in order to unambiguously determine the EOS of high density matter. In the meantime, intriguing possible extensions of PNS simulations with *npQ* matter include the consideration of heterogeneous structures [54], quark matter superfluidity [48] and coherent ν scattering on droplets [55].

Chapter 5

Color-Neutral Superconducting Quark Matter

5.1 Introduction

Studies of QCD at high baryon density have led to the expectation that quark matter is a color superconductor in which the pairing gaps of unlike quarks (ud, us, and ds) are as large as 100 MeV. For three massless flavors, a symmetric ground state called the Color-Flavor-Locked (CFL) phase, in which BCS-like pairing involves all nine quarks, is favored [106, 107]. At lower density and for physically relevant values of the strange current quark mass ($100 < m_s/\text{MeV} < 300$), a less symmetric (2SC) phase in which only the light up and down quarks ($m_{u,d} \leq 10$ MeV) pair is expected [42, 43]. For recent reviews, see Refs. [108, 109].

With the exception of the work by Iida and Baym [110], and more recently by Alford and Rajagopal [111], little attention has been paid to the issue of color neutrality in superconducting quark phases. These works are the primary motivation for this study. The issues addressed here are similar to those addressed by Alford and Rajagopal [111] who perform a model independent analysis that is valid when $m_s \ll \mu$ and $\Delta \sim m_s^2/\mu$, where Δ is the pairing gap and μ is the quark number chemical potential. We employ an extended version of the the Nambu-Jona-Lasinio model (NJL hereafter), which shares many symmetries with QCD including the spontaneous breaking of chiral symmetry, and calculate the thermodynamic potentials, Ω, and pairing gaps, Δ, self-consistently in the CFL and 2SC phases. Our analysis leads to results that complement some of the conclusions in Ref. [111]. There are, however, several aspects in which we go further. First, we employ a self-consistent model which uniquely determines both the diquark and the quark-anti quark condensates. Second, since the realization of color and electric charge neutrality becomes non-trivial only for physically relevant values of m_s, we retain terms to all orders in m_s in our calculation of Ω. As noted in Ref. [111], this is

particularly important for understanding the phase structure of quark matter at densities (or equivalently, μ) of relevance to neutron stars, since m_s/μ is not small compared to unity. In addition, we establish the phase structure of superconducting color-neutral quark matter at finite temperature and lepton content which was not considered in [110, 111], but is relevant for studies of proto-neutron stars.

5.1.1 Charges, chemical potentials, and color neutrality

Bulk, homogeneous matter must be neutral with respect to charges which interact through the exchange of massless gauge bosons. Otherwise, the free energy density cost would be infinite. In the CFL phase, diquark condensation breaks color symmetry and all eight gluons become massive via the Higgs mechanism. Similarly, in the 2SC phase, $SU(3)_c$ is broken down to $SU(2)_c$ and five of the eight gluons become massive. In both the CFL and 2SC phases, however, an $U(1)$ gauge symmetry remains unbroken [106]. The associated charge is called $\tilde{Q}$. The generator for this charge in the CFL phase is a linear combination of the usual electric charge Q and a combination of color generators T_3 and T_8, and is given by

$$\tilde{Q} = Q - \frac{1}{2}\, T_3 - \frac{1}{2\sqrt{3}}\, T_8\,, \tag{5.1}$$

where $Q = diag(2/3, -1/3, -1/3)$ in flavor space, and $T_3 = diag(1, -1, 0)$ and $T_8 = diag(1/\sqrt{3}, 1/\sqrt{3}, -2/\sqrt{3})$ in color space.

The color superconducting phase is, by construction, neutral with respect to $\tilde{Q}$ charge. Why then should we impose, in addition, local color neutrality? As noted earlier, gluons become massive in the superconducting phase and the free energy density cost of realizing a non-zero color density in bulk matter need not be infinite. Further, although a finite sample embedded in the normal state must be a color singlet, this alone does not require local color neutrality since color singletness is a global constraint. Hence a heterogenous phase with colored domains of typical size similar to the color Debye screening length is a possibility. However, in a homogeneous and color conducting medium a color charge density in the bulk is unstable as it generates a chromo-electric field resulting in the flow of color charges [111]. Color neutrality is therefore a requirement for the homogeneous phase. Neutrality with respect to charges associated with T_3 and T_8 is achieved by introducing appropriate chemical potentials μ_3 and μ_8 in analogy with the charge chemical potential μ_Q. As noted in Refs. [111, 112], color neutrality is a prerequisite for color singletness,

but the additional free energy density cost involved in projecting out the color singlet state is negligible for large samples.

The superconducting ground state breaks both color and electromagnetic gauge symmetries. It would therefore seem that excitations above the condensate can only be characterized by the unbroken $\tilde{Q}$ charge. At first sight, this would imply that electrons and unpaired quarks carry only $\tilde{Q}$ charge and must therefore be assigned only a $\mu_{\tilde{Q}}$ chemical potential. If this were indeed the case, it would be impossible to neutralize the 2SC phase in the bulk. This is because the condensate is $\tilde{Q}$ neutral, but has color and electric charge that cannot be neutralized by particles with only $\tilde{Q}$ charge. The resolution to this puzzle lies in noting that our expectation to assign only those charges that are unbroken by condensation to excitations applies only to excitations above a charge-neutral ground state. In this case, charges associated with broken gauge symmetries are easily delocalized and transported to the surface by the condensate. It is however important to note that only the excess broken charge resides on the surface. In describing particles that make up the charge neutral ground state we must use vacuum quantum numbers. In this case, the individual charges are localized on the particles in the bulk. Therefore, in what follows we treat electrons and unpaired quarks as carrying their vacuum charges in our description of the neutral ground state.

5.2 Thermodynamics

We begin with the NJL Lagrangian [15, 71, 72, 77, 113, 114] supplemented by both a diquark interaction and the t'Hooft six-fermion interaction which reproduces the anomalous $\mathrm{U_A}(1)$ symmetry breaking present in QCD [38]. Explicitly,

$$\begin{aligned}
\mathcal{L} \;=\;& \bar{q}_{i\alpha}\left(i\partial\!\!\!/\delta_{ij}\delta_{\alpha\beta} - m_{ij}\delta_{\alpha\beta} - \mu_{ij,\,\alpha\beta}\gamma^0\right) q_{j\beta} \\
&+G_S\sum_{a=0}^{8}\left[\left(\bar{q}\lambda_f^a q\right)^2 + \left(\bar{q}i\gamma_5\lambda_f^a q\right)^2\right] \\
&-G_D\left[\det{}_{ij}\,\bar{q}_{i\alpha}\left(1+i\gamma_5\right)q_{j\beta} + \det{}_{ij}\,\bar{q}_{i\alpha}\left(1-i\gamma_5\right)q_{j\beta}\right]\delta_{\alpha\beta} \\
&+G_{DIQ}\sum_k\sum_\gamma\left[\left(\bar{q}_{i\alpha}\epsilon_{ijk}\epsilon_{\alpha\beta\gamma}q^C_{j\beta}\right)\left(\bar{q}^C_{i'\alpha'}\epsilon_{i'j'k}\epsilon_{\alpha'\beta'\gamma}q_{j'\beta'}\right)\right. \\
&\qquad\left.+\left(\bar{q}_{i\alpha}i\gamma_5\epsilon_{ijk}\epsilon_{\alpha\beta\gamma}q^C_{j\beta}\right)\left(\bar{q}^C_{i'\alpha'}i\gamma_5\epsilon_{i'j'k}\epsilon_{\alpha'\beta'\gamma}q_{j'\beta'}\right)\right]\,, \qquad (5.2)
\end{aligned}$$

where m_{ij} is the diagonal current quark matrix, and the spinor $q^C = C\bar{q}^T$, where C is the Dirac charge conjugation matrix. We use α, β, γ for color (r= red, b= blue, and g= green) indices, and i, j, k for flavor (u= up, d= down, and s= strange) indices throughout. The chemical potential matrix is diagonal in flavor and color, and is given by

$$\mu_{ij,\,\alpha\beta} = (\mu\delta_{ij} + Q_{ij}\mu_Q)\delta_{\alpha\beta} + \delta_{ij}\left(T_{3\alpha\beta}\mu_3 + T_{8\alpha\beta}\mu_8\right)\,, \qquad (5.3)$$

where μ is the quark number chemical potential. Since the couplings G_S, G_D, and G_{DIQ} are dimensionful, we impose an ultra-violet three-momentum cutoff, Λ, and results are considered meaningful only if the quark Fermi momenta are well below this cutoff. The values of the couplings are fixed by reproducing the experimental vacuum values of f_π, m_π, m_K, and $m_{\eta'}$ as in Ref. [72]. For the most part, we discuss results obtained using

$$\begin{aligned}
m_{0u} \;=\;& m_{0d} = 5.5\ \mathrm{MeV}\,, \qquad m_{0s} = 140.7\ \mathrm{MeV}\,, \qquad \Lambda = 602.3\ \mathrm{MeV}\,, \\
G_S\Lambda^2 \;=\;& 1.835\,, \qquad G_D\Lambda^5 = 12.36\,, \qquad \text{and} \qquad G_{DIQ} = 3G_S/4\,. \qquad (5.4)
\end{aligned}$$

We note that, in vacuum, the effective four-fermion interaction in the qq and $\bar{q}q$ channels are related by a Fierz transformation which yields $G_{DIQ} = 3G_S/4$. Because the mean-field approximation breaks this Fierz invariance, these terms must be treated separately and each carry independent couplings. We also discuss results for $G_{DIQ} = G_S$, and provide a brief discussion on the sensitivity of the results to acceptable changes in the couplings in our conclusions. Note that Eq. (5.2) does not include the possible presence of a six-fermion interaction due to diquark ($\langle qq\rangle$) condensates; such interactions have been assumed to result only in a renormalization of the four-fermion diquark interaction. In the mean field approximation, the thermodynamic potential per unit volume (see sections C.1 and C.2 in Appendix C) is given by

$$\begin{aligned}
\Omega \;=\;& -2G_S\sum_{i=u,d,s}\langle\bar{q}_i q_i\rangle^2 + 4G_D\langle\bar{u}u\rangle\left\langle\bar{d}d\right\rangle\langle\bar{s}s\rangle + \sum_k\sum_\gamma\frac{\left|\Delta^{k\gamma}\right|^2}{4G_{DIQ}} \\
&-\frac{1}{2}\int\frac{d^3p}{(2\pi)^3}\sum_{i=1}^{72}\left[\frac{\lambda_i}{2} + T\ln\left(1+e^{-\lambda_i/T}\right)\right] + \Omega_0\,, \qquad (5.5)
\end{aligned}$$

where $\langle\bar{q}_i q_i\rangle$ ($i = u, d, s$) is the quark condensate, and the term Ω_0 ensures that the zero density pressure, $P = -\Omega$, of non-superconducting matter is zero:

$$\Omega_0 = 2G_S\sum_{i=u,d,s}\langle\bar{q}_i q_i\rangle_0^2 - 4G_D\langle\bar{u}u\rangle_0\left\langle\bar{d}d\right\rangle_0\langle\bar{s}s\rangle_0 + 2N_cN_f\sum_i\int\frac{d^3p}{(2\pi^3)}\sqrt{m_i^2+p^2}\,, \qquad (5.6)$$

where $< \bar{q}_i q_i >_0$ denotes the value of the quark condensate at zero density. The gap matrix

$$\Delta^{k\gamma} = 2G_{DIQ} \left\langle \bar{q}_{i\alpha} i\gamma_5 \varepsilon^{ijk} \varepsilon^{\alpha\beta\gamma} q^C_{j\beta} \right\rangle \tag{5.7}$$

features three non-vanishing elements. Using the standard notation of denoting $\Delta^{k\gamma}$ through the flavor indices i and j, we have

$$\Delta_{ds} \equiv \Delta^{ur}, \qquad \Delta_{us} \equiv \Delta^{dg}, \qquad \text{and} \qquad \Delta_{ud} \equiv \Delta^{sb}. \tag{5.8}$$

This corresponds to the ansatz in Ref. [107], except that color sextet gaps (symmetric in both color and flavor) are ignored. Inclusion of the sextet gaps modifies our results only slightly, because such gaps are small [107]. Note, however, that we have removed the degeneracy between Δ_{us} and Δ_{ds} in order to explore phases in which these gaps may not be equal.

The quasiparticle energies λ_i may be obtained by diagonalizing the inverse propagator. Equivalently, λ_i are the eigenvalues of the (72×72) matrix

$$D = \begin{bmatrix} -\gamma^0 \vec{\gamma} \cdot \vec{p} - M_i \gamma^0 + \mu_{i\alpha} & \Delta i \gamma^0 \gamma_5 C \\ \gamma^0 C i \gamma_5 \Delta & -\gamma^0 \vec{\gamma}^T \cdot \vec{p} + M_i \gamma^0 - \mu_{i\alpha} \end{bmatrix}, \tag{5.9}$$

where M_i are the dynamically generated quark masses and Δ is given by

$$\Delta = \Delta_{ud} \varepsilon^{3ij} \varepsilon^{3\alpha\beta} + \Delta_{us} \varepsilon^{2ij} \varepsilon^{2\alpha\beta} + \Delta_{ds} \varepsilon^{1ij} \varepsilon^{1\alpha\beta}. \tag{5.10}$$

Equations (5.2) through (5.10) enable a consistent model calculation of the thermodynamics of superconducting quark matter as a function of the chemical potentials μ, μ_Q, μ_3, and μ_8 at arbitrary temperatures. For a given set of these chemical potentials, the dynamical (or constituent-like) masses M_i and the gaps Δ_{ij} are determined by the solutions of equations that result from extremizing Ω with respect to $\langle \bar{q}_i q_i \rangle$ and Δ_{ij}, respectively.

The phases are labeled according to which of the three gaps are non-zero: (1) Normal phase: all gaps zero, (2) 2SC phase: only Δ_{ud} is non-zero, and (3) CFL phase: all gaps are non-zero. Where needed, we add electrons simply by noting that $\mu_e = -\mu_Q$, and include their free Fermi gas contribution to Ω.

Recall that the ground state is $\tilde{Q}$ neutral, i.e., $n_{\tilde{Q}} = -\partial\Omega/\partial\mu_{\tilde{Q}} = 0$, which is a consequence of the fact that the condensates are $\tilde{Q}$ neutral. Quasiparticles carrying $\tilde{Q}$ charge are massive with $m \sim \Delta$. In addition, the $\tilde{Q}$ susceptibility $\chi_{\tilde{Q}} = \partial n_{\tilde{Q}}/\partial\mu_{\tilde{Q}} \simeq 0$; in fact, the free energy density is independent of $\mu_{\tilde{Q}}$ at zero temperature. This is because to generate $\tilde{Q}$ charge in the ground state, we must break a pair and the energy cost is of $O[\Delta]$. In contrast, the free energy density depends on μ_Q, μ_3, and μ_8, and, the corresponding individual susceptibilities do not vanish. For a physical m_s of order 100 MeV, there is no apriori reason to expect equal numbers of u, d, and s quarks in the CFL phase. The pairing ansatz in Eq. (5.8) and the arguments of Rajagopal and Wilczek [115], however, guarantee that

$$n_{rd} = n_{gu}\,, \qquad n_{bd} = n_{gs}\,, \qquad \text{and} \qquad n_{rs} = n_{bu}\,, \tag{5.11}$$

or equivalently, that

$$n_u = n_r\,, \qquad n_d = n_g\,, \qquad \text{and} \qquad n_s = n_b\,, \tag{5.12}$$

where $n_{\alpha i}$ is the number density of quarks with color α and flavor i, and n_α (n_i) is the net number density of color α (flavor i). Pairing by itself does not enforce either color or electric charge neutrality. The strange quark mass induces both color and electric charge in the CFL phase. We are, however, at liberty to adjust the chemical potentials μ_3 and μ_8 to enforce color neutrality. Moreover, since the pairing ansatz enforces $\tilde{Q}$ neutrality, enforcing color neutrality automatically enforces electric charge neutrality at $\mu_Q = 0$. In contrast, the 2SC phase requires a finite μ_Q to satisfy electric charge neutrality and hence admits electrons.

5.3 Results for $G_{DIQ} = 3G_S/4$

5.3.1 Zero temperature and zero neutrino chemical potential

We turn now to discuss results, beginning with those at temperature $T = 0$. The color densities for the chemical potentials μ_3 and μ_8 are defined as

$$n_3 \equiv -\frac{\partial\Omega}{\partial\mu_3} \qquad \text{and} \qquad n_8 \equiv -\frac{\partial\Omega}{\partial\mu_8}. \tag{5.13}$$

The NJL model results for these densities are shown in Figure 5.1 for matter which is *not* color or electrically neutral. The color density corresponding to the "3" gluon is zero at zero temperature in both the CFL and 2SC phases, since $\mu_3 = 0$ as discussed in the analytical results below. The color density corresponding to the "8" gluon is clearly non-zero and demands a non-zero value of μ_8 to ensure color neutrality.

In Figure 5.2, we show the dynamically generated or constituent d and s quark masses M_i (left panel) and the pairing gaps Δ_{ij} (right panel) as functions

of μ in the CFL and 2SC phases. The u quark mass, which tracks the trend of the d quark, is not shown for the sake of clarity. The dark (light) curves refer to the case in which color and electric charge neutrality is (is not) imposed. All masses decrease with increasing μ, since all of the $\langle\bar{q}q\rangle$ condensates decrease with μ. Note that the requirement of color and charge neutrality has a larger effect on the s quark mass in the 2SC phase than in the CFL phase. This is because neutrality in the 2SC phase requires a large and negative electric charge chemical potential. In the discussion that follows, we will show that $\mu_Q \sim -m_s^2/2\mu$ in the 2SC phase. Further, since $\mu_s = \mu - \mu_Q/3$, a large and negative μ_Q enhances the strange quark density which in turn suppresses the $\langle\bar{s}s\rangle$ condensate.

The right panel of Figure 5.2 shows the various gaps in the CFL and 2SC phases. Imposing color neutrality reduces Δ_{ud}, since the numbers of red and green quarks (equivalently of u and d quarks) are reduced relative to the colored case (see the analytical analysis below). For the same reason, color neutrality increases the gaps involving strange quarks. These trends are broken only when μ begins to approach the ultra-violet cutoff Λ. The strong increase of the Δ_{ud} gap as μ decreases for matter in which neutrality is not imposed is due to the strong decrease in the gaps involving strange quarks.

In Figure 5.3, we show the chemical potentials μ_8 and μ_Q (as functions of μ) required to achieve color and electric charge neutrality in the CFL and 2SC phases. The solid curves refer to results of the NJL model calculations. The left panel of Figure 5.4 shows the pressure P versus μ at $T = 0$. Here the dark (light) curves refer to the case in which color and electric charge neutrality is (is not) imposed. Note that the pressure of the color and electrically neutral normal phase falls below that of the 2SC phase for all μs shown. The pressure differences ΔP or the free energy density cost necessary to ensure color and electric charge neutrality in the CFL and 2SC phases are shown in the right panel of Figure 5.4. Here also the solid curves refer to results of the NJL model calculations.

In order to gain a qualitative understanding of the results in Figures 5.3 and 5.4, we undertake an analytical analysis of a simpler model also considered in Ref. [111]. In this analysis, we consider u and d quarks as massless, and include corrections due to the s quark mass m_s at leading order as a shift in its chemical potential. This does not properly account for the shift in energy due the strange quark mass for states far away from the Fermi surface, but is a consistent approximation in this context since we are primarily interested in the leading order cost of enforcing neutrality. Further, we assume that all

gaps, including those involving the s quark, are independent of m_s,[1] and that both the gaps and m_s are weak functions of the chemical potentials. With these assumptions, and to leading order in Δ

$$\begin{aligned}
\Omega_{\rm CFL} &= \Omega_{\rm rgb} + \Omega_{\rm rg} + \Omega_{\rm rs} + \Omega_{\rm gs}\,, \\
\Omega_{\rm rgb} &= -\frac{1}{12\pi^2}\left(\mu_1^4 + \mu_2^4 + \mu_3^4 + 3\Delta^2(\mu_1^2 + \mu_2^2 + 4\mu_3^2)\right)\,, \\
\Omega_{\rm rg} &= -\frac{1}{6\pi^2}\left(\mu_{\rm rg}^4 + 3\Delta^2\mu_{\rm rg}^2\right)\,, \\
\Omega_{\rm rb} &= -\frac{1}{6\pi^2}\left(\mu_{\rm rb}^4 + 3\Delta^2\mu_{\rm rb}^2\right)\,, \qquad \text{and} \\
\Omega_{\rm gb} &= -\frac{1}{6\pi^2}\left(\mu_{\rm gb}^4 + 3\Delta^2\mu_{\rm gb}^2\right)\,,
\end{aligned} \tag{5.14}$$

where we have written the free energy of the CFL phase in terms of the 3×3 block involving $ru - gd - bs$ quarks, and three 2×2 blocks involving $rd - gu$, $rs - bu$ and $gs - bd$ quarks, respectively. Each of the three 2×2 blocks is rigid in the sense that the free energy is unaffected by differences in chemical potentials of quarks that pair in a given block [115]. The free energy depends only on the average chemical potential. The 3×3 block does not exhibit this rigidity; here, the quasi-particle energies depend on the splitting between the chemical potential characterizing the ru, gd and bs quarks. Chemical potentials that characterize the free energy of the 3×3 block are given by

$$\mu_1 = \mu + \frac{\mu_8}{\sqrt{3}}\,, \qquad \mu_2 = \mu - \frac{\mu_8}{\sqrt{3}} - \frac{m_s^2}{3\mu}\,, \qquad \text{and} \qquad \mu_3 = \mu - \frac{m_s^2}{6\mu}\,, \tag{5.15}$$

and the common chemical potentials that appear in the free energy expressions of the 2×2 blocks are given by

$$\mu_{\rm rg} = \mu + \frac{\mu_8}{\sqrt{3}}\,, \quad \mu_{\rm rb} = \mu - \frac{\mu_8}{2\sqrt{3}} - \frac{m_s^2}{4\mu}\,, \quad \text{and} \quad \mu_{\rm gb} = \mu - \frac{\mu_8}{2\sqrt{3}} - \frac{m_s^2}{4\mu} \tag{5.16}$$

We note that, in general, pairing between particles with dissimilar masses does not require a common chemical potential. Maximal BCS-like pairing requires that the distribution of the pairing partners be identical in momentum space. Since we treat the u and d quarks as massless particles and account for the effects of the s quark mass through a shift in the chemical potential in

[1] Corrections to Δ due to m_s arise at $O[m_s^2/\mu]$; for a detailed discussion, see Ref. [116].

our analytic analysis, a common chemical potential within each pairing block ensures that the aforementioned pairing criterion is satisfied.

In the CFL phase, the stress induced by the strange quark mass generates color charges. In the limit of nearly equal and vanishing light quark masses, the CFL scheme in Eq. (5.12) indicates that we will require only a non-zero μ_8 to achieve color neutrality. This justifies why we neglect μ_Q and μ_3 in Eqs. (5.15) and (5.16). To leading order in the parameter m_s^2/μ, and assuming that the differences between the various gaps are small and μ, m_s-independent, we find that

$$\mu_8(CFL) = -\frac{1}{2\sqrt{3}}\frac{m_s^2}{\mu} + O\left[\frac{m_s^4}{\mu^3}, \frac{m_s^2\Delta^2}{\mu^3}\right] \tag{5.17}$$

by requiring $\partial\Omega_{CFL}/\partial\mu_8 = 0$. Since $n_u = n_d$ and hence $n_r = n_g$ when there are no electrons, $\mu_3(CFL) = 0$ identically in the CFL phase at zero temperature. Naively, Eq. (5.17) would imply that the free energy density cost of enforcing color neutrality in the CFL phase is of $O[m_s^2\mu^2]$. However, we find that such contributions are absent due to cancellations. This result (see the lower-most dotted curve in Figure 5.3), with m_s and Δ of the NJL model as inputs, provides an excellent approximation to the exact NJL result. Utilizing Eq. (5.17), we find an analytic estimate for the free energy density cost in the CFL phase:

$$\Delta\Omega_{CFL} = \Omega_{CFL}(\mu_8) - \Omega_{CFL}(0) = \frac{5m_s^4}{72\pi^2} + O\left[\frac{m^6}{\mu^2}, \frac{m^4\Delta^2}{\mu^2}\right]. \tag{5.18}$$

The lower dotted curve in the right panel of Figure 5.4 shows that this result is in quantitative agreement with the NJL model calculation.

In the 2SC phase, the pairing phenomenon itself gives rise to color charges. The 2SC thermodynamic potential, to leading order in the gap and consistent with the approximation scheme described earlier, is

$$\begin{aligned}
\Omega_{2SC} &= \Omega_{\rm rugd} + \Omega_{\rm free}\,, \\
\Omega_{\rm rugd} &= -\frac{1}{3\pi^2}\left(\mu_{\rm rugd}^4 + 3\Delta^2\mu_{\rm rugd}^2\right)\,, \\
\Omega_{\rm free} &= -\frac{1}{12\pi^2}\left(\mu_{\rm bu}^4 + \mu_{\rm bd}^4 + \mu_{\rm bs}^4 + \mu_{\rm rs}^4 + \mu_{\rm gs}^4 + \mu_Q^4\right)\,.
\end{aligned} \tag{5.19}$$

The chemical potentials appearing above are defined by

$$\mu_{\rm rugd} = \mu + \frac{\mu_8}{\sqrt{3}} + \frac{\mu_Q}{6}\,, \qquad \mu_{\rm bu} = \mu - \frac{2\mu_8}{\sqrt{3}} + \frac{2\mu_Q}{3}\,,$$

$$\begin{aligned}
\mu_{\rm bd} &= \mu - \frac{2\mu_8}{\sqrt{3}} - \frac{\mu_Q}{3}\,, \mu_{\rm bs} = \mu - \frac{2\mu_8}{\sqrt{3}} - \frac{\mu_Q}{3} - \frac{m_s^2}{2\mu}\,, \qquad \text{and} \\
\mu_{\rm rs} &= \mu_{\rm gs} = \mu + \frac{\mu_8}{\sqrt{3}} - \frac{\mu_Q}{3} - \frac{m_s^2}{2\mu}\,.
\end{aligned} \tag{5.20}$$

The condition to ensure color neutrality, $\partial\Omega_{2SC}/\partial\mu_8 = 0$, yields

$$\mu_8(2SC) = -\frac{1}{3\sqrt{3}}\frac{\Delta^2}{\mu} + O\left[\frac{\Delta^4}{\mu^3}\right], \tag{5.21}$$

where we have used a common value of Δ (independent of μ) in the analytical analysis. Note that $\mu_8(2SC)$ does not depend on m_s at leading order. Since pairing in the 2SC phase involves red and green quarks, it does not induce a color 3-charge; hence $\mu_3(2SC) = 0$. However, electric charge neutrality in the 2SC phase requires an adjustment due to the magnitude of m_s. At leading order in a $1/\mu$ expansion, we find

$$\begin{aligned}
\mu_Q(2SC) &= -\frac{1}{2}\frac{m_s^2}{\mu} - \frac{1}{3}\frac{\Delta^2}{\mu} \\
&\quad + O\left[\frac{m_s^4}{\mu^3}, \frac{\Delta^2 m_s^2}{\mu^3}\right]
\end{aligned} \tag{5.22}$$

by setting $\partial\Omega_{2SC}/\partial\mu_Q = 0$. As in the CFL phase, the free energy density cost of enforcing color neutrality in the 2SC phase is small, because $O[\Delta^2\mu^2]$ terms cancel and the free energy density begins to change at $O[\Delta^4]$. Similarly, we find that there is no cost for enforcing electric charge neutrality in the 2SC phase at $O[\mu^2]$. Using the results in Eqs. (5.21) and (5.22), the free energy density cost of enforcing color and electric charge neutrality becomes

$$\begin{aligned}
\Delta\Omega_{2SC} &= \Omega_{2SC}(\mu_8, \mu_Q) - \Omega_{2SC}(0,0) = \frac{1}{8\pi^2}\left(m_s^4 + \frac{4\Delta^2 m_s^2}{3} + \frac{4\Delta^4}{3}\right) \\
&\quad + O\left[\frac{m_s^6}{\mu^2}, \frac{\Delta^6}{\mu^2}, \frac{\Delta^2 m_s^4}{\mu^2}\right].
\end{aligned} \tag{5.23}$$

Although the free energy density costs of enforcing color neutrality in the CFL and 2SC phases are of the same order, the cost in the 2SC phase is numerically larger. This is in part due to the larger strange quark mass in the 2SC phase and because the free energy density cost due to Δ and m_s dependent terms add in the 2SC phase. The analytical results in Eqs. (5.21), (5.22), and (5.23), shown as dotted curves in Figures 5.3 and 5.4, compare well with the results of the NJL model.

5.3.2 Phase diagram at finite temperature and lepton content

In the proto-neutron star context, matter is subject to stresses induced by finite temperature and lepton number chemical potentials [10]. Since electrons have both electric and lepton number charges,

$$\mu_e = -\mu_Q + \mu_{Le}\,, \tag{5.24}$$

where $\mu_{Le} = \mu_{\nu_e}$ is the chemical potential for electron lepton number. In order to explore the effects of a finite neutrino chemical potential and finite temperature on the superconducting phases, we employ the NJL model, Eq. (5.5) with extensions to include neutrinos and electrons.

Figure 5.5 shows representative cross-sectional views of the $T-\mu-\mu_{\nu_e}$ phase diagram. The left panel displays results at fixed $\mu = 460$ MeV. With increasing temperature, a first order transition occurs from the CFL phase to the 2SC phase with ud pairing. For $\mu_{Le} = 0$, the transition occurs at $T \simeq 17$ MeV. The corresponding baryon densities are $n_B = (n_u + n_d + n_s)/3 = 1.06$ fm^{-3} in the CFL phase and $n_B = 0.94$ fm^{-3} in the 2SC phase. At zero neutrino chemical potential, an analytic estimate of the critical temperature T_c for the CFL-2SC transition can be obtained by assuming that the gaps in the 2SC and CFL phases are nearly equal to each other and to their zero temperature values. We find that

$$\begin{aligned} T_c &= \frac{\sqrt{2}}{\pi}\Delta_0 \left[1 - \frac{4}{5}\frac{\delta\Delta}{\Delta_0}\,\xi_{\rm BCS}^2 + \frac{9}{20}\frac{m_s^2}{\Delta_0^2}\frac{\delta m_s}{m_s}\right]\,\xi_{\rm BCS} \qquad \text{with} \\ \xi_{\rm BCS} &= \left(1 + 2\frac{\Delta_0^2}{\pi^2 T_{\rm BCS}^2}\right)^{-1}, \end{aligned} \tag{5.25}$$

where Δ_0 is the zero temperature gap, $\delta\Delta$ and δm_s are the differences between the gaps and the strange quark masses in the 2SC and CFL phases, respectively. $T_{\rm BCS}$ is the temperature at which the gap in the CFL phase would vanish, assuming that $\Delta(T) = \Delta_0\sqrt{1-(T/T_{\rm BCS})^2}$. Note that, in general, gaps involving strange quarks do not vanish at the transition, i.e, the phase transition is first order. This is because at leading order, the critical temperature $T_c \sim \Delta_0/2.22$ is less than that for the second order BCS transition, $T_{\rm BCS} \simeq \Delta_0/1.76$. It is clear from Eq. (5.25) that contributions to T_c due to $\delta\Delta$ and δm_s can easily alter this, allowing for a BCS like second order transition. If the magnitude of the gap in the 2SC phase is larger than that in the CFL phase, T_c is lowered and the transition becomes more strongly first order.

Accommodating a finite lepton number in the CFL phase is expensive, because the requirement of color and electric charge neutrality in this phase excludes electrons. At $T = 0$, the transition from the CFL to 2SC phase occurs at $\mu_{Le} \simeq 150$ MeV. The latent heat density, $T\Delta(\partial P/\partial T)$, lies in the range (2–15) MeV/fm^3 along the boundary of the first order phase transition. With increasing temperature, the critical lepton chemical potential at which the CFL-2SC transition occurs decreases. This is because the gaps in the CFL phase decrease with increasing T; consequently, unlocking occurs at smaller μ_{ν_e}.

The right panel in Figure 5.5 shows the phase boundaries at fixed $\mu_{\nu_e} = 200$ MeV. For this neutrino chemical potential, the CFL phase is preferred above $\mu = 460$ MeV at $T = 0$. For low (high) values of μ, the region of the CFL phase shrinks (expands) progressively to lower (higher) values of T and μ_{ν_e}. In contrast, the 2SC-Normal phase boundary is relatively unaffected by increasing values of μ (in the range relevant for proto-neutron star studies), although minor variations do occur. Note that with increasing temperature, the phase transition switches from first to second order. This switch is due to the fact that the Δ_{us} and Δ_{ds} gaps decrease along the first order phase transition line. When these gaps vanish (at $T \sim 25$ MeV for $\mu_{\nu_e} = 200$ MeV), the phase transition becomes second order. In Figure 5.5, contours of constant baryon density are shown by the dotted curves in both panels. Notice that, for the values of μ and μ_{ν_e} chosen for display, the 2SC phase supports lower baryon densities than the CFL phase. Across the first order phase transition, the density contours are discontinuous. We wish to add that the phase in which $\Delta_{us} \neq \Delta_{ds}$ was found to be thermodynamically disfavored in the range of T, μ, and μ_{ν_e} explored here.

In this chapter, we have not considered the role of Goldstone bosons in the CFL phase. The K^+ meson is expected to be the lightest positively charged meson in the CFL phase [117]. The inclusion of Goldstone bosons in the excitation spectrum can alter some of the above results as found in Ref. [52]. In particular, charged kaon condensation can allow for the presence of electrons at finite μ_{Le} and lower the free energy density cost for accommodating lepton number. This will likely affect the results in Figure 5.5 quantitatively, but we expect the generic trends to remain intact at the qualitative level.

The consequences of requiring local color neutrality in superconducting quark matter with and without neutrinos at both zero and finite temperatures are our principal findings. Quantitative results, especially those for quark number chemical potentials approaching the ultra-violet cut-off in the NJL model used, should be viewed with some caution. Notwithstanding this, the basic qualitative features concerning the phase transitions appear to be generic,

insofar as similar trends are found in our analytic analysis that employed a simplified model without a cutoff. We also wish to emphasize that the phase diagram in Figure 5.5 requires revision at low values of μ (or low baryon densities) for which a hadronic phase is more likely to be favored.

5.3.3 Sensitivity of Results to G_{DIQ}

In order to assess the extent to which the results depend on the strength of the diquark coupling, G_{DIQ}, we show results with $G_{DIQ} = G_S$ in Figures 5.6 through 5.9; in order, these results should be compared with those for $G_{DIQ} = 3G_S/4$ in Figures 5.2 through 5.5. Figure 5.6 displays the effective masses (left panel) and the superconducting gaps (right panel) as a function of density for the 2SC and CFL phases at zero temperature. The dark (light) curves refer to matter in which color and electric neutrality is (is not) imposed. In the left panel, the up quark masses are equal to the down quark masses and are not plotted for the sake of clarity. In color neutral matter, the strange quark mass is larger for the larger coupling at high density (compare Figures 5.2 and 5.6). This is likely an artifact of the three-momentum cutoff at high density. As expected, the gaps are larger for the larger G_{DIQ}, but the density dependence is similar. The large increase (as a function of decreasing density) in the Δ_{ud} gap for matter which is not neutral is due to the strong decrease in the gaps involving strange quarks.

Results from the analytical expressions in Eqs. (5.17), (5.21), and (5.22) are compared with the exact results in Figure 5.7. The level of agreement between these two results is unchanged from the case of the smaller diquark coupling constant shown in Figure 5.3.

The pressure at zero temperature as a function of chemical potential μ is shown in the left panel of Figure 5.8. The 2SC phase is favored up to 420 MeV, which is somewhat lower than the critical chemical potential for the case of $G_{DIQ} = 3G_S/4$ (see Figure 5.4). The right panel displays the pressure difference between matter in which color and electric neutrality are imposed and the case in which color and electric neutrality are not imposed. The extent of the low density region in which a 2SC phase is favored over the CFL phase is not greatly changed from the case of $G_{DIQ} = 3G_S/4$ and the 2SC phase continues to be favored over the normal phase, except at low μ where we expect hadrons to dominate. The dotted lines in Figure 5.8 are the approximations of Eqs. (5.23) and (5.18) and the solid line is from the NJL model calculation.

Figure 5.9 shows the phase diagram in the $\mu_{\nu_e} - T$ plane for fixed μ (left panel) and the phase diagram in the $\mu - T$ plane for fixed μ_{ν_e} (right panel).

This figure is slightly different from the phase diagram for $G_{DIQ} = 3G_S/4$ in Figure 5.5 inasmuch as the chemical potential for the left hand panel is 430 MeV, in contrast to 460 MeV. The transition between the 2SC and CFL phases in the left panel becomes second order as the temperature becomes large. The phase transition in the right panel becomes second order at about 58 MeV. Because of the larger diquark coupling, the critical temperature is nearly a factor of three higher than in Figure 5.5, where the phase transition became second order at 22 MeV. The larger coupling constant also causes the the transition to ungapped quark matter from the 2SC phase to occur at a higher temperature.

5.4 Astrophysical implications

The $T - \mu - \mu_{\nu_e}$ phase diagram offers clues about the possible phases encountered by a neutron star from its birth as a proto-neutron star (in which neutrinos are trapped) in the wake of a supernova explosion to its neutrino-poor catalyzed state with ages ranging from hundreds of thousands to million years. In earlier work, some aspects of how a phase transition from the normal to the 2SC phase would influence neutrino transport in a newly-born neutron star were explored [48]. To date, detailed calculations of the evolution of a proto-neutron star with quarks have been performed for the case in which only the normal phase was considered [14]. Our findings indicate that the core of a proto-neutron star may well encounter a 2SC phase first when matter is hot and neutrino-rich before passing over to a CFL phase.

5.5 Conclusions

Color and electric charge neutrality in the superconducting quark phases requires the introduction of chemical potentials for color and electric charge. The magnitudes of these chemical potentials are sub-leading in μ. The corresponding free energy density costs are small and independent of μ at leading order with the free energy density cost for neutrality in the 2SC phase being significantly larger than that in the CFL phase. Consequently, and in agreement with Ref. [111], we find that the bulk 2SC phase is less likely to occur in compact stars at $T = 0$ and $\mu_{\nu_e} = 0$. In the NJL model, a small 2SC window does exist at relatively low baryon density. However, since this window occurs at very low density it is likely to be shut by the hadronic phase. If homogeneous quark matter were to occur in neutron stars, it seems likely that

with increasing μ a sharp interface would separate hadronic matter and CFL quark matter [51]. We note, however, that we have only considered homogeneous phases in this study and it is possible that less symmetric heterogenous phases may well be favored for chemical potentials of relevance to neutron stars. Examples include the CFL-Hadron mixed phase [51] and crystalline superconductivity [118]. These possibilities alleviate the cost of enforcing color neutrality, since in these cases it is only a global constraint. In such phases, however, energy costs associated with gradients in particle densities must be met.

At finite temperature and neutrino chemical potential, the CFL phase becomes less favored both because of its small specific heat and because of its exponentially suppressed (by the factor $\exp(-\Delta/T)$) electron number density, which makes the free energy density cost of accommodating lepton number large. In contrast, the 2SC phase has a larger specific heat and easily accommodates electron number, and is therefore the favored phase at finite temperature and lepton number. We expect that the inclusion of Goldstone bosons in the CFL phase will tend to extend the region in the $T - \mu_{\nu_e}$ plane where the CFL phase is favored, since Goldstone bosons contribute significantly to the specific heat and also allow for the presence of electrons. In the absence of Goldstone bosons, a first order unlocking transition occurs from the CFL phase to the less symmetric 2SC phase with increasing lepton chemical potential. When the temperature is sufficiently high, the phase transition switches from first to second order due to the fact that the Δ_{us} and Δ_{ds} gaps decrease along the first order phase transition line and eventually vanish.

As discussed above, different phases of color superconducting quark matter are likely to be traversed by the inner core of a proto-neutron star during its early thermal evolution. The task ahead is to study how these phases and transitions between them influence observable aspects of core collapse supernova, neutron star structure, and thermal evolution.

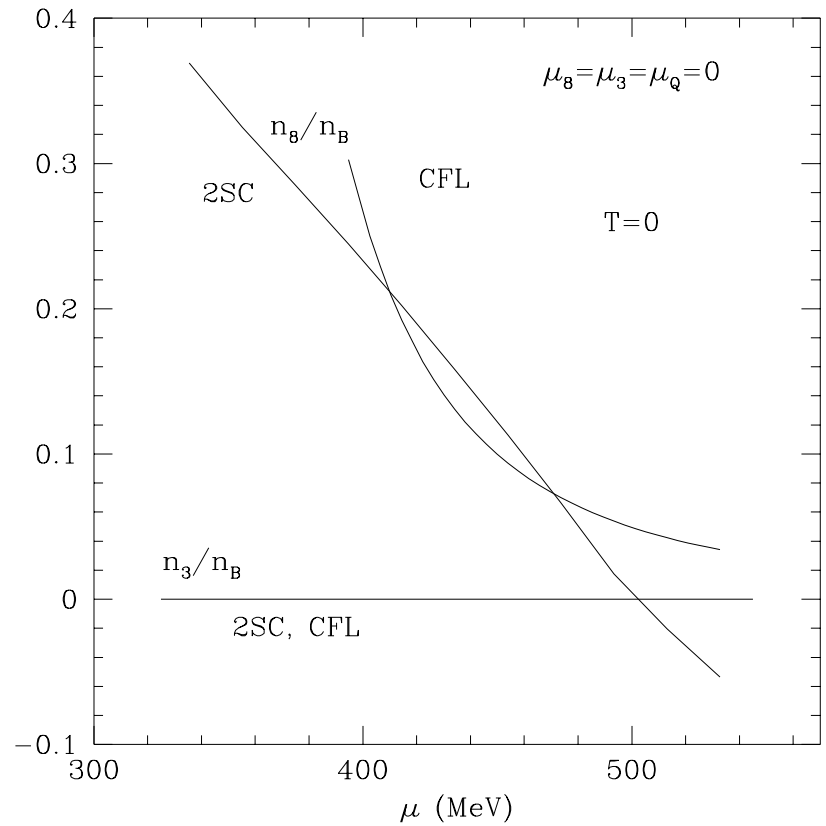

Figure 5.1: Color densities for matter with $\mu_3 = \mu_8 = 0$ in the NJL model as a function of quark number chemical potential μ at zero temperature.

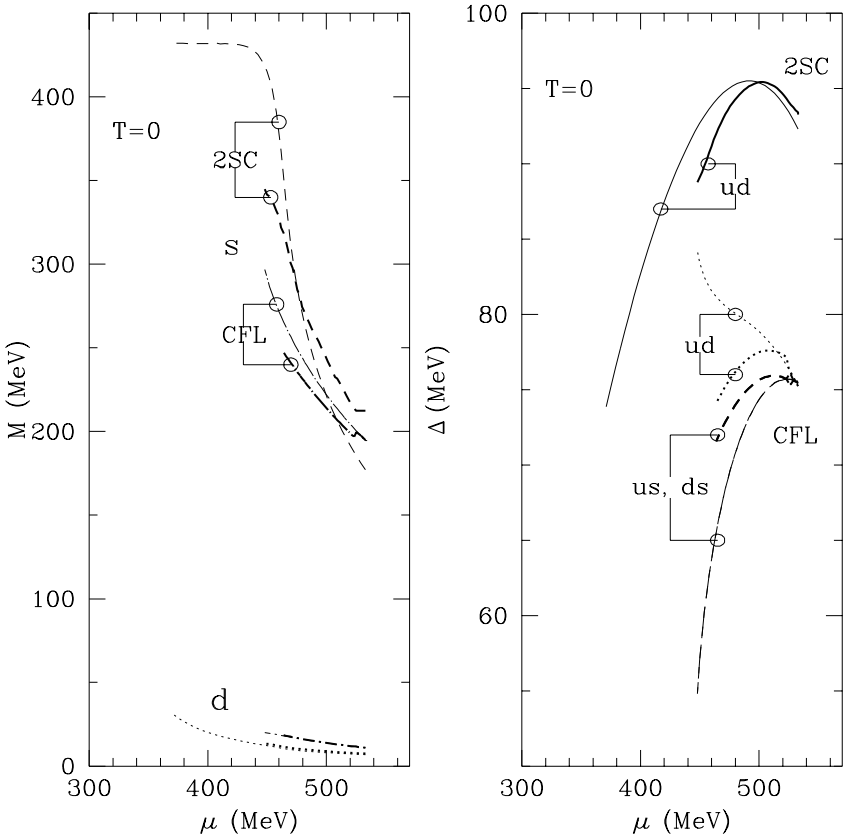

Figure 5.2: Dynamically generated masses and pairing gaps in the CFL and 2SC phases at zero temperature from NJL model calculations. Dark (light) curves refer to results when color and electric charge (C & Q) neutrality is (is not) imposed.

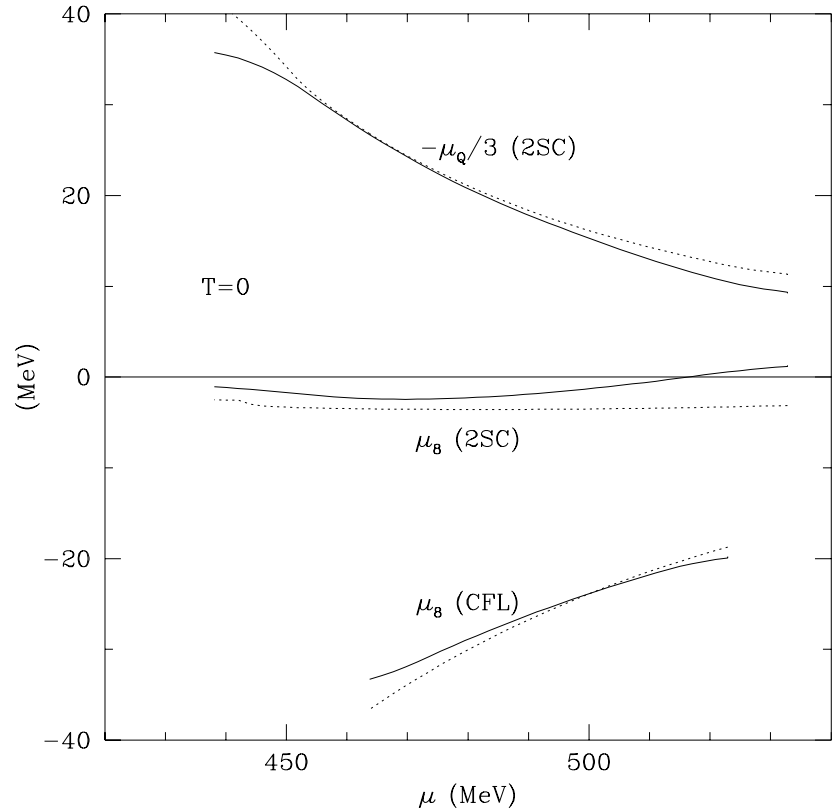

Figure 5.3: Chemical potentials μ_8 and μ_Q that ensure color and electric charge neutrality in the CFL and 2SC phases as functions of the quark number chemical potential μ at temperature $T = 0$. Solid (dashed) curves refer to results of the NJL (simplified) model.

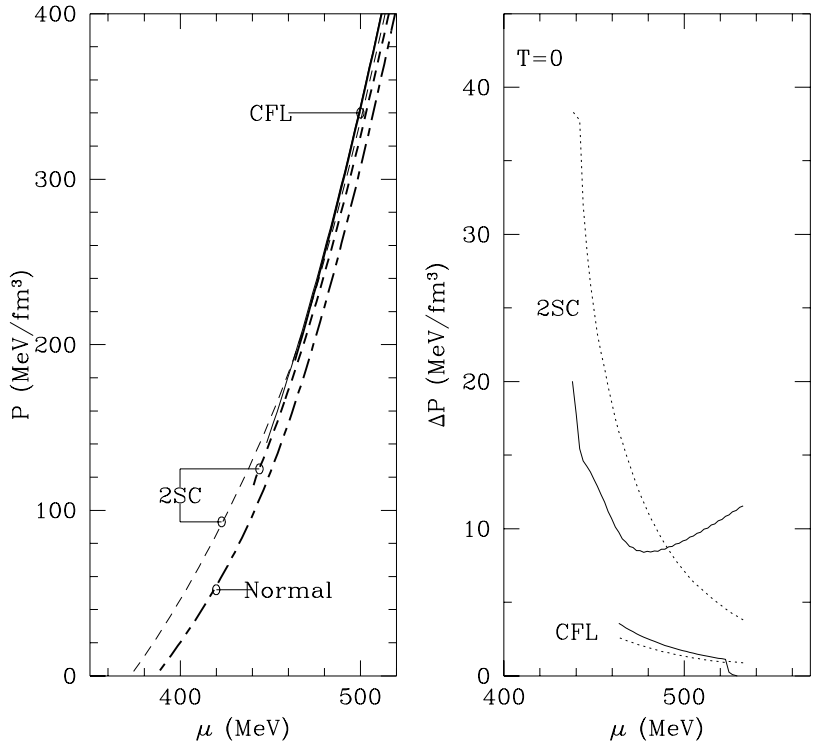

Figure 5.4: Left panel: The pressure P versus quark number chemical potential μ in the CFL, 2SC, and normal phases at temperature $T = 0$. Dark (light) curves refer to the case in which color and electric charge (C & Q) neutrality is (is not) imposed. Right panel: Pressure differences ΔP or the free energy density cost required to ensure C & Q neutrality in the CFL and 2SC phases at $T = 0$. Solid (dotted) curves are results of the NJL (simplified) model calculations.

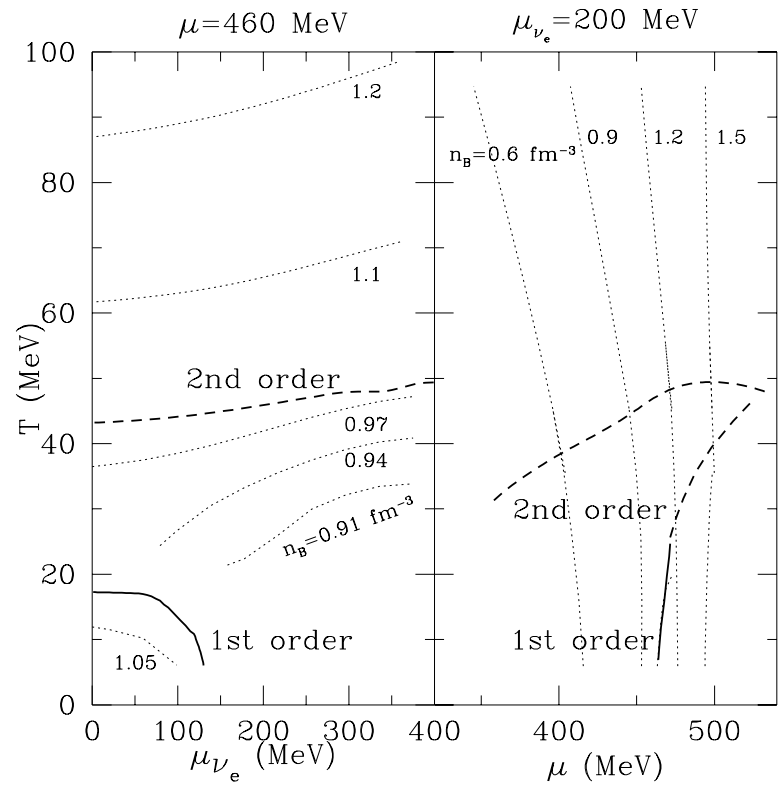

Figure 5.5: Cross-sectional views of the $T - \mu - \mu_{\nu_e}$ phase diagram at the indicated values of μ and μ_{ν_e}. In both panels, the dark curves show the phase boundaries, while the dotted curves show contours of constant baryon density.

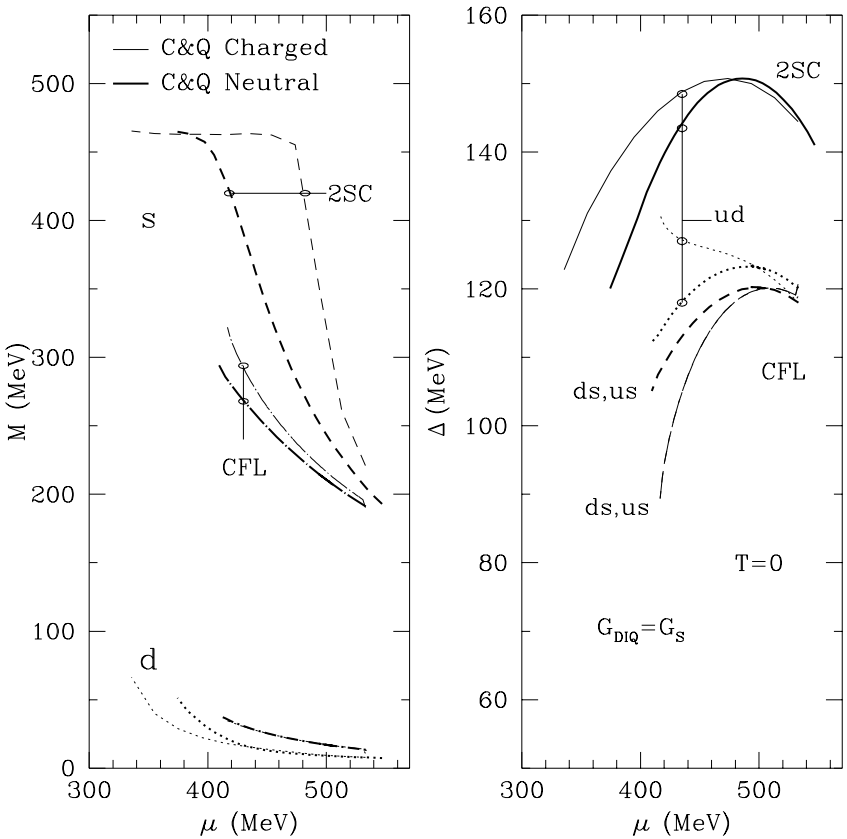

Figure 5.6: Same as Figure 5.2, but with $G_{DIQ} = G_S$.

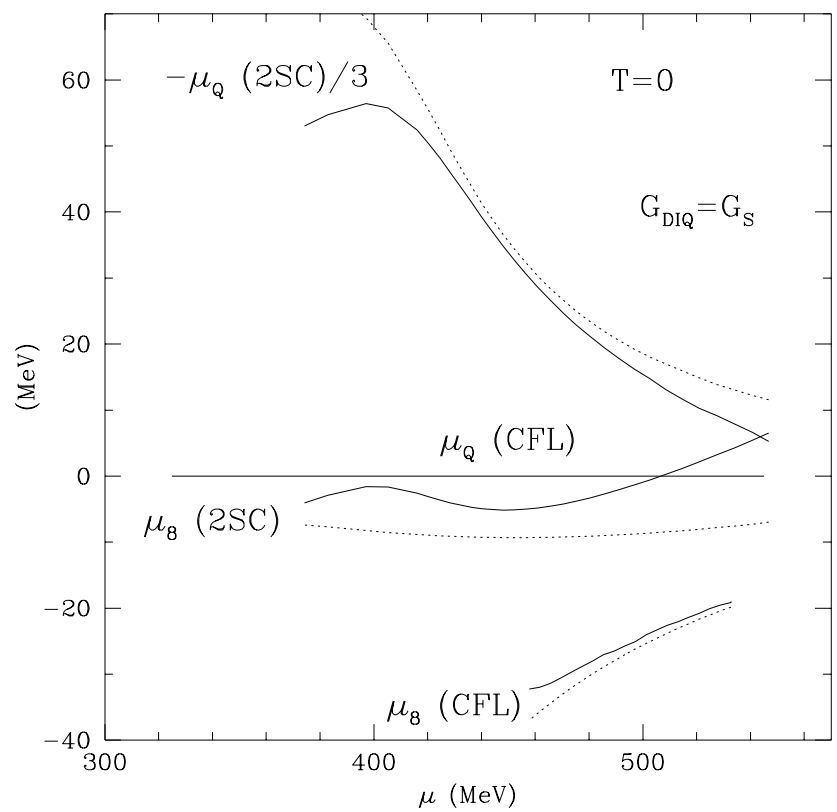

Figure 5.7: Same as Figure 5.3, but with $G_{DIQ} = G_S$.

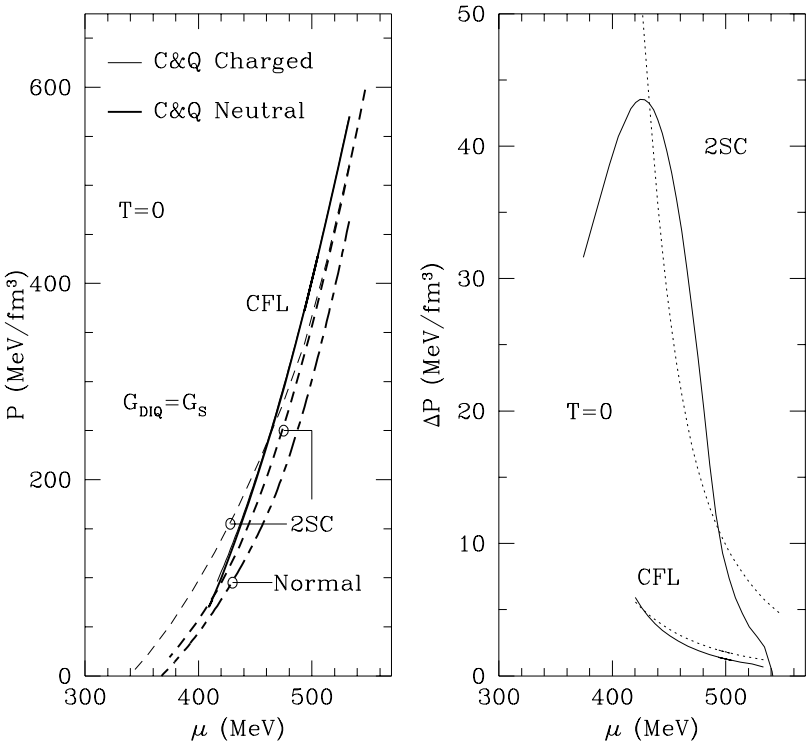

Figure 5.8: Same as Figure 5.4, but with $G_{DIQ} = G_S$.

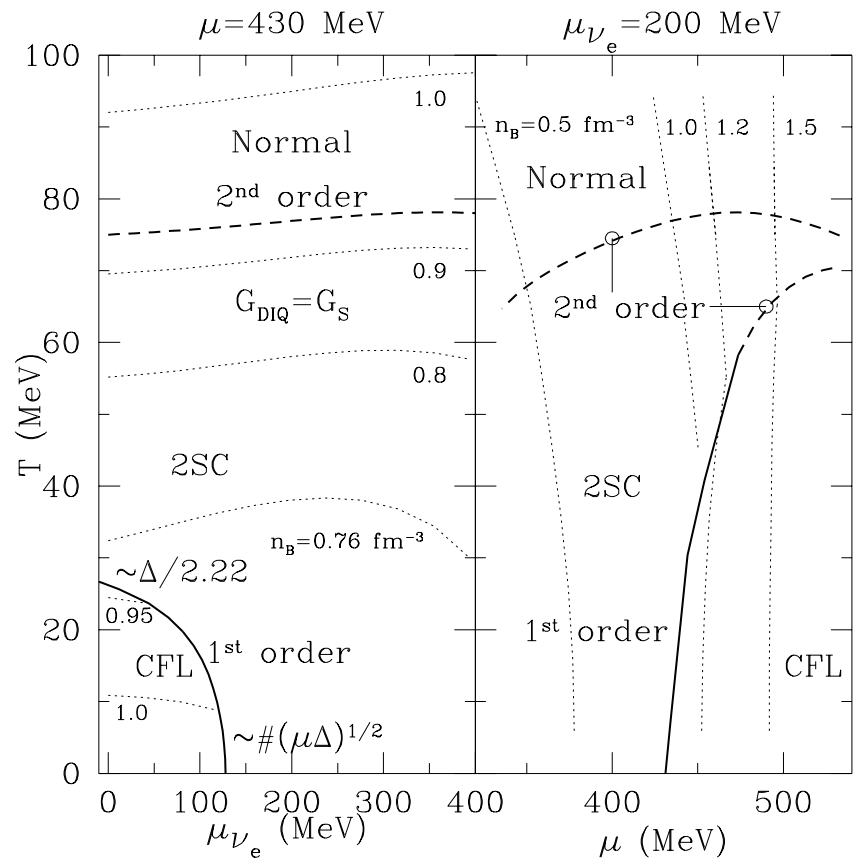

Figure 5.9: Same as Figure 5.5, but with $G_{DIQ} = G_S$ and with a chemical potential of 430 MeV in the left panel.

Chapter 6

Conclusions and Outlook

The primary goal of this work was to explore the effects of the presence of deconfined quark matter on the structure and thermal evolution of neutron stars. To this end,

1. The first calculation of the equation of state of quark matter using dynamically generated quark masses at finite temperature and finite neutrino chemical potential was performed. This equation of state was applied to the study of neutron star structure (Chapter 2).

2. Utilizing the results of Chapter 2, the mean free paths of neutrinos in quark matter were calculated under conditions relevant for proto-neutron stars in order to provide a self-consistent assessment of the effect of quark matter on neutrino propagation in proto-neutron star evolution (Chapter 3).

3. In Chapter 4, a complete picture of the macrophysical evolution of a proto-neutron star with quark matter was presented with the *only* detailed and self-consistent calculation using modern microphysical ingredients, namely, the equation of state of quark matter and its associated neutrino opacities (Chapters 2 and 3). Metastability times were calculated for quark matter and compared with other softening components. The feasibility of detecting quark matter in existing and planned neutrino observatories was discussed.

4. The first calculation of the phase diagram of color-superconducting quark matter at finite temperature and neutrino chemical potential was presented using a model in which the gaps and the dynamical quark masses were calculated self-consistently. The analysis included a new assessment of the cost of enforcing both color and electric neutrality (Chapter 5).

In order of the presentation in Chapters 2 through 5, the conclusions that emerge from this study are:

1. That it is possible for a mixed phase to exist in a neutron star of virtually any mass above 1.4 $M_\odot$. Depending upon the EOS, a mixed phase is more likely to exist in stars larger than 1.5 $M_\odot$. The precise stellar mass above which a mixed phase containing quarks might exist depends on the "softness" of the hadronic EOS and the effective bag pressure of the quark model. Although the quark content of matter at a given density is maximized for stiffer hadronic equations of state, the extent of the mixed phase region in a neutron star of a given mass is maximized for softer hadronic EOSs. Only extreme cases result in a star with a pure quark core.

   This mixed phase is delayed until most neutrinos have diffused from the star, leading to the possible metastability of proto-neutron stars (PNSs), a robust result which depends only on the existence of quarks in dense matter. Finite temperature permits the quark-hadron transition to occur at slightly lower densities than at zero temperature, but in a newly-formed PNS this effect is swamped by the large trapped neutrino fraction which has the opposite tendency. Furthermore, temperature decreases with increasing density along adiabats in the quark-hadron mixed phase, a behavior opposite to that generally found in a mixed phase region containing a kaon condensate. This implies that core temperatures may be significantly lower in stars containing quarks than in those not containing quarks. Neutrino opacities, which are sensitive to temperature, will be affected, but the implications for the emitted neutrino fluxes and temperatures can only be reliably evaluated in the context of a detailed PNS simulation discussed below.

2. In the presence of quarks, neutrinos have a significantly smaller opacity and hence larger diffusion coefficients than those in purely hadronic matter at similar densities (Chapter 3). These differences may have an observable impact on the neutrino flux from PNSs containing quark matter, but these differences are not expected to become apparent until the PNS is 10–20 s old.

   Concerning the evolution of a PNS, it is expected that the initial star, which is lepton rich, will not have an extensive mixed phase region. Only after several seconds of evolution will quark matter appear. In a newly-formed mixed phase region, the neutrino opacity will be substantially smaller than in the case in which a mixed phase region does not appear.

However, due to the large $\nu-$optical depth of the PNS, neutrinos remain trapped, and no significant effect on emergent neutrino luminosities is expected at early times. As the star evolves, however, the relatively larger increase in opacity and the growing extent of the mixed phase region eventually allows a larger flux of neutrinos, and thereby a more rapid evolution.

3. Using the equation of state and neutrino cross section information above, a detailed calculation of the evolution of a proto-neutron star with quarks was performed (Chapter 4). The metastability and subsequent collapse to a black hole of a PNS containing quark matter, or other types of matter including hyperons or a Bose condensate, are observable in current and planned ν detectors. However, discriminating among these compositions may require more than one such observation.

   Clearly, the observation of a single case of metastability, and the determination of the metastability time alone, will not necessarily permit one to distinguish among the various possibilities. Only if the metastability time is less than 10–15 s, could one decide on this basis that the star's composition was that of npH matter. However, as in the case of SN 1987A, independent estimates of M_B might be available [99, 100]. In addition, the observation of two or more metastable neutron stars might permit one to differentiate among these models.

4. The principal findings in Chapter 5 result from the requirement local color neutrality in superconducting quark matter with and without neutrinos at both zero and finite temperatures. The magnitudes of these chemical potentials for color and electric neutrality are sub-leading in μ. The corresponding free energy density costs are small and independent of μ at leading order with the free energy density cost for neutrality in the 2SC phase being significantly larger than that in the CFL phase. Consequently, and in agreement with Ref. [111], the bulk 2SC phase is less likely to occur in compact stars at $T = 0$ and $\mu_{\nu_e} = 0$. In the NJL model, a small 2SC window does exist at relatively low baryon density. However, since this window occurs at very low density it is likely to be shut by the hadronic phase.

   At finite temperature and neutrino chemical potential, the CFL phase becomes less favored both because of its small specific heat and because of its exponentially suppressed (by the factor $\exp(-\Delta/T)$) electron number density, which makes the free energy density cost of accommodating lepton number large. In contrast, the 2SC phase has a larger specific heat and easily accommodates electron number, and is therefore the favored phase at finite temperature and lepton number. The inclusion of Goldstone bosons in the CFL phase will tend to extend the region in the $T - \mu_{\nu_e}$ plane where the CFL phase is favored, since Goldstone bosons contribute significantly to the specific heat and also allow for the presence of electrons. In the absence of Goldstone bosons, a first order unlocking transition occurs from the CFL phase to the less symmetric 2SC phase with increasing lepton chemical potential.

Although the question of the existence of quark matter inside neutron stars cannot yet be definitively answered, the effects of the presence of quark matter on the evolution of a proto-neutron star has been clarified. Metastable neutron stars, those which collapse to a black hole after deleptonization, offer an excellent opportunity to test for the presence of deconfined quark matter. The abrupt cessation of the neutrino signal provides clear and unambiguous evidence of a softening phase transition. The timescale over which this cessation in the neutrino emission occurs will give some information about the nature of this softening component.

Although not discussed in detail here, the long-term evolution of a neutron star may also provide information about the possible presence of quark matter. Although the cooling characteristics of a neutron star with quark matter can often be reproduced in models without quark matter [92], advances in understanding the microphysical issues involved in neutron star cooling will likely improve this situation. In a star consisting entirely of strange quark matter, the cooling characteristics are more unique [61]. A strange quark star would likely be anomalously hot and compact [60], and observation of such an object would be difficult to explain unless it was a strange quark star.

There are several questions that have been left unanswered. In particular,

1. This work has focused on times longer than approximately 1 s after core bounce, after which effects of dynamics and accretion become unimportant. Studies of the ν signal during the first second, during which approximately 1/3 of the energy is emitted, and at late times, as the star becomes optically thin to neutrinos, requires more accurate techniques for $\nu-$transport. In addition, the earliest time periods require the incorporation of hydrodynamics [101, 102, 103, 104, 105].

2. Heterogeneous structures in the quark-hadron mixed phase region and the coherent scattering of neutrinos on these structures have been addressed in Refs. [54, 55]. Additionally, neutrino emissivities and opacities from Goldstone bosons in the CFL phase have also been com-

puted [63, 64]. However, a quantitative study of their influence on observable neutrino fluxes from proto-neutron stars remains to be undertaken.

3. Effects of the CFL-Hadron mixed phase [51] and crystalline superconductivity [118] have not been adequately addressed with regard to their observable consequences for supernova neutrinos. These possibilities alleviate the cost of enforcing color neutrality, since in these cases it is a global constraint. In such phases, however, energy costs associated with gradients in particle densities must be met.

4. Goldstone bosons created from the spontaneous breaking of chiral symmetry will make quantitative corrections to the phase diagram of quark matter. This topic is currently under active investigation.

5. The effects of quark superconductivity and of the different phases of color superconducting quark matter that are likely to be traversed by the inner core of a proto-neutron star during its early thermal evolution, have not been addressed. The task ahead is to study how these phases, and transitions between them, influence observable aspects of core collapse supernova, neutron star structure, and thermal evolution.

At the time of writing, we are fortunate that several neutrino observatories are in place and many more are under construction and consideration. The ever increasing fiducial volumes of these detectors are capable of detecting several thousands of neutrinos from a galactic core-collapse supernova unlike the handful of neutrinos that were detected in the supernova explosion of SN 1987A. In addition to revealing the fundamental properties of the various flavors of neutrinos, and uncovering the supernova explosion mechanism itself, the detection of such neutrinos offer the promise of delineating the properties of strongly interacting dense matter beyond the reach of laboratory studies and shed light on the synthesis of heavy elements of which we are made of. In short, the predictions contained in this thesis, including the direct observation of the formation of a black hole, may be tested.

Epilogue

Neutrinos Reveal Star's Inner Secrets [1]

Physical Review Focus features a couple of articles every month to be presented in a way that is accessible for students and researchers in all fields of physics. The material in Chapter 4 was featured as a Physical Review Focus article, and is reproduced below.

[1] Text by Geoff Brumfiel. Reprinted with permission from Phys. Rev. Focus **7**, story 26, 1 June, 2001 (http://focus.aps.org). Copyright 2001 by The American Physical Society.

Astronomers go to mountaintop observatories to get a good look at the sky, but the best view might be over a mile underground inside neutrino detectors. Neutrinos–neutral particles that regularly fly through the Earth undetected–may provide astronomers with information that light cannot. A paper in the 4 June PRL predicts that neutrinos from proto-neutron stars might reveal the existence of exotic quark matter inside these stars. It also shows that the presence of such matter could lead to the birth of a black hole, an event the authors believe could be detected from neutrino observations.

When a star explodes in a supernova, it leaves behind a dense core, called a proto-neutron star, which contains an equal number of protons and neutrons. The impulse from the supernova quickly converts the protons into neutrons–a process that releases many energetic neutrinos. Seconds after the explosion, the conversion is complete: The proto-neutron star has become a neutron star–a cold, dead star made primarily of neutrons. By the time the light and dust from the supernova dissipate, the proto-neutron star is gone.

"Observing the neutrinos is the only way we can observe the proto-neutron star," says James Lattimer of the State University of New York (SUNY) at Stony Brook. In 1987, detectors around the world recorded nearly twenty neutrinos from a proto-neutron star in the heart of a supernova. Neutrinos like these, Lattimer says, could provide information about the life of such a star. In their paper, the SUNY team calculates the neutrino energy that would be detected for proto-neutron stars made of three proposed forms of "quark matter": matter in which quarks become unglued from each other, matter filled with baryons containing strange quarks, and matter filled with kaon particles, which also contain strange quarks. In each case, the group describes a signature neutrino signal that could be detected at facilities like the new Sudbury Neutrino Observatory in Canada or Super-Kamiokande in Japan.

The team also shows that these detectors could watch black holes form. Their calculations reveal that the presence of quark matter could "soften" the proto-neutron star, making it easier to compress. In certain cases, the team believes that this softening could cause the proto-neutron star to collapse under its own gravity into a black hole. If that happened, detectors on earth would see a sudden cessation of neutrinos from the star. "You could catch the [black hole's formation] during the time it's happening, and that's important," says Madappa Prakash, the head of the SUNY group. "It's like catching a thief in the act."

Figure 6.1: **Watching the Stars.** At the heart of the Sudbury Neutrino Observatory in Canada is a large spherical vessel of water surrounded by 9500 photodetectors. It's one of a handful of facilities worldwide that could glimpse a proto-neutron star or witness the birth of a black hole.

The new neutrino detectors will have "unprecedented sensitivity," says Adam Burrows of the University of Arizona in Tucson. Burrows believes that the SUNY team's calculations will help these detectors analyze neutrino data from the next supernova. But until such an event occurs, he adds, it will be impossible to tell exactly what a proto-neutron star looks like.

Bibliography

[1] W. Baade and F. Zwicky. *Prc. Nat. Acad. Sci.*, 20:255, 1934.

[2] H.A. Bethe, G.E. Brown, J. Applegate, and J. M. Lattimer. *Nucl. Phys. A*, 334:487, 1979.

[3] G. Brown and H. A. Bethe. *Sci. Am.*, 252:60, 1985.

[4] A. Burrows and T. L. Mazurek. *Nature*, 301:315, 1983.

[5] A. Burrows and J. Lunine. *Nature*, 378:333, 1995.

[6] S. A. Colgate and R. H. White. *Astrophys. J.*, 143:626, 1966.

[7] W. D. Arnett. *Can. J. Phys.*, 44:2553, 1966.

[8] T. Mazurek. *Nature*, 252:287, 1974.

[9] M. Prakash, J. R. Cooke, and J.M. Lattimer. *Phys. Rev. D*, 52:661, 1995.

[10] M. Prakash, I. Bombaci, Manju Prakash, P. J. Ellis, J. M. Lattimer, and R. Knorren. *Phys. Rep.*, 280:1, 1997.

[11] A. Burrows and J. M. Lattimer. *Astrophys. J.*, 307:178, 1986.

[12] J. A. Pons, S. Reddy, M. Prakash, J. M. Lattimer, and J. A. Miralles. *Astrophys. J.*, 513:780, 1999.

[13] J. A. Pons, S. Reddy, P.J. Ellis, M. Prakash, and J.M. Lattimer. *Phys. Rev. C*, 62:035803, 2000.

[14] J. A. Pons, A. W. Steiner, M. Prakash, and J. M. Lattimer. *Phys. Rev. Lett.*, 86:5223, 2001.

[15] A. W. Steiner, M. Prakash, and J. M. Lattimer. *Phys. Lett. B*, 486:239, 2000.

[16] A. W. Steiner, M. Prakash, and J. M. Lattimer. *Phys. Lett. B*, 509:10, 2001.

[17] H.-Y. Chiu. *Ann. Phys.*, 26:364, 1964.

[18] J. N. Bahcall and R. A. Wolf. *Phys. Rev.*, 140:1445, 1965.

[19] J. M. Lattimer, C. J. Pethick, M. Prakash, and P. Haensel. *Phys. Rev. Lett.*, 66:2701, 1991.

[20] M. Prakash, Manju Prakash, J.M. Lattimer, and C. Pethick. *Astrophys. J*, 390:L77, 1992.

[21] J. W. Negele and D. Vautherin. *Nucl. Phys. A*, 207:298, 1973.

[22] C. J. Pethick and D. G. Ravenhall. *Ann. Rev. Nucl. Phys.*, 45:429, 1995.

[23] D. Q. Lamb, J.M. Lattimer, C. J. Pethick, and D. G. Ravenhall. *Phys. Rev. Lett.*, 41:1623, 1978.

[24] C. P. Lorenz, D. G. Ravenhall, and C. J. Pethick. *Phys. Rev. Lett.*, 70:379, 1993.

[25] G. Baym, C. J. Pethick, and P. Sutherland. *Astrophys. J.*, 170:299, 1971.

[26] V. G. J. Stoks, R. A. M. Klomp, M. C. M. Rentmeester, and J. J. de Swart. *Phys. Rev. C*, 48:792, 1993.

[27] B. Day and R. B. Wiringa. *Phys. Rev. C*, 55:1855, 1985.

[28] A. Akmal and V. R. Pandharipande. *Phys. Rev. C*, 56:2261, 1997.

[29] A. Akmal, V. R. Pandharipande, and D. G. Ravenhall. *Phys. Rev. C*, 58:1804, 1998.

[30] B. D. Serot and J. D. Walecka. *Advances in Nuclear Physics, J. W. Negele and E. Vogt, Eds.* Plenum Press, 1984.

[31] M. Prakash, P. J. Ellis, and J. I. Kapusta. *Phys. Rev. C*, 45:2518, 1992.

[32] H. Müller and B. D. Serot. *Nucl. Phys. A*, 606:508, 1996.

[33] P. Hohenberg and W. Kohn. *Phys. Rev.*, 136:B864, 1964.

[34] W. Kohn and L. J. Sham. *Phys. Rev.*, 140:A1133, 1965.

[35] A. Chodos, R. L. Jaffe, K. Johnson, and J. Kiskis. *Phys. Rev. D*, 9:3471, 1974.

[36] T. DeGrand, R. Jaffe, K. Johnson, and J. Kiskis. *Phys. Rev. D*, 12:2060, 1975.

[37] B. Freedman and L. McLerran. *Phys. Rev. D*, 17:1109, 1978.

[38] G. 't Hooft. *Phys. Rep.*, 142:357, 1986.

[39] T. Hatsuda and T. Kunihiro. *Phys. Rep.*, 247:221, 1994.

[40] B. Barrois. *Nucl. Phys. B*, 129:390, 1977.

[41] D. Bailin and A. Love. *Phys. Rep.*, 107:325, 1984.

[42] M. Alford, K. Rajagopal, and F. Wilczek. *Phys. Lett. B*, 422:247, 1998.

[43] R. Rapp, T. Schäffer, E. V. Shuryak, and M. Velkovsky. *Phys. Rev. Lett.*, 81:53, 1998.

[44] R. Csalbuoni and R. Gatto. *Phys. Lett. B*, 464:111, 1999.

[45] D. T. Son and M. A. Stephanov. *Phys. Rev. D*, 61:074012, 2000.

[46] M. Rho, A. Wirzba, and I. Zahed. *Phys. Lett. B*, 473:126, 2000.

[47] T. Schäffer. *Phys. Rev. Lett.*, 85:5531, 2000.

[48] G. Carter and S Reddy. *Phys. Rev. D*, 62:103002, 2000.

[49] J. Madsen. *Phys. Rev. Lett.*, 85:10, 2000.

[50] M. Alford, J. Berges, and K Rajagopal. *Nucl. Phys. B*, 571:269, 2000.

[51] M. Alford, K. Rajagopal, S. Reddy, and F. Wilczek. *Phys. Rev. D*, 64:074017, 2001.

[52] D. B. Kaplan and S. Reddy. *Phys. Rev. D*, 65:054042, 2002.

[53] N. K. Glendenning. *Phys. Rev. D*, 46:1274, 1992.

[54] M. B. Christiansen, N. K. Glendenning, and J. Schaffner-Bielich. *Phys. Rev. C*, 62:025804, 2000.

[55] S. Reddy, G. F. Bertsch, and M. Prakash. *Phys. Lett. B*, 475:1, 2000.

[56] T. Norsen and S. Reddy. *Phys. Rev. C*, 63:065804, 2001.

[57] T. J. Burrows, A. Mazurek and J. M. Lattimer. *Astrophys. J.*, 251:325, 1981.

[58] V. Thorsson, M. Prakash, and J. M. Lattimer. *Nucl. Phys. A*, 572:693, 1994.

[59] E. Witten. *Phys. Rev. D*, 30:272, 1984.

[60] J.M. Lattimer and M. Prakash. *Astrophys. J.*, 550:426, 2001.

[61] D. Page and V. V Usov. *astro-ph/0204275*, 2002.

[62] S. Reddy, M. Prakash, and J. M. Lattimer. *Phys. Rev. D*, 58:013009, 1998.

[63] P. Jaikumar, M. Prakash, and T. Schäfer. *astro-ph/0203088*, 2002.

[64] S. Reddy, M. Sadzikowski, and M. Tachibana. *nucl-th/0203011*, 2002.

[65] A. W. Steiner, S. Reddy, and M. Prakash. *hep-ph/0205201*, 2002.

[66] W. Keil and H. T. Janka. *Astron. Astrophys.*, 296:145, 1995.

[67] P. J. Ellis, J. M. Lattimer, and M. Prakash. *Comm. Nuc. Part. Phys.*, 22:63, 1996.

[68] N. K. Glendenning and S. A. Moszkowski. *Phys. Rev. Lett.*, 61:2414, 1991.

[69] D. J. Millener, C. B. Dover, and A. Gal. *Phys. Rev. C*, 38:2700, 1988.

[70] Manju Prakash, E. Baron, and M. Prakash. *Phys. Lett. B*, 243:175, 1990.

[71] Y. Nambu and G. Jona-Lasinio. *Phys. Rev.*, 122:345, 1961.

[72] P. Rehberg, S. P. Klevansky, and J. Hüfner. *Phys. Rev. C*, 53:410, 1996.

[73] T. Kunihiro. *Phys. Lett. B*, 219:363, 1989.

[74] S. Klimt, M. Lutz, and W. Weise. *Phys. Lett. B*, 249:386, 1990.

[75] M. Hanauske, L.M. Satarov, I.N. Mishustin, H. Stoecker, and W. Greiner. *Phys. Rev. D*, 64:043005, 2001.

[76] S. Klimt, M. Lutz, U. Vogl, and W. Weise. *Nucl. Phys. A*, 516:429, 1990.

[77] M. Buballa and M. Oertel. *Phys. Lett. B*, 457:261, 1999.

[78] K. Schertler, S. Leupold, and J. Schaffner-Bielich. *Phys. Rev. C*, 60:025801, 1999.

[79] A. Burrows and R. F. Sawyer. *Phys. Rev. C*, 59:510, 1999.

[80] J. A. Pons, J. A. Miralles, M. Prakash, and J. M. Lattimer. *Astrophys. J.*, 553:382, 2001.

[81] N. Iwamoto. *Ann. Phys. (N.Y.)*, 141:1, 1982.

[82] S. Weinberg. *Phys. Rev. Lett.*, 307:178, 1986.

[83] A. Wadhwa, V. K. Gupta, S. Singh, and J. D. Anand. *J. Phys. G*, 21:1137, 1995.

[84] S. K. Ghosh, S. C. Phatak, and P. K. Sahu. *Int. J. Mod. Phys. E*, 5:385, 1996.

[85] D. L. Tubbs and D. N. Schramm. *Astrophys. J.*, 201:467, 1975.

[86] C. K. Jung. In M. V. Diwan and C. K. Jung, editors, *Next Generation Nucleon Decay and Neutrino Detector, AIP Conf. Proc. No. 533*, page 29, New York, 2000. AIP.

[87] J.C. Collins and M.J. Perry. *Phys. Rev. Lett*, 30:1353, 1975.

[88] D.J. Gross and F. Wilczek. *Phys. Rev. D*, 8:3633, 1973.

[89] D.J. Gross and F. Wilczek. *Phys. Rev. D*, 9:980, 1974.

[90] H.D. Politzer. *Phys. Rev. Lett.*, 30:1346, 1973.

[91] J.M. Lattimer and M. Prakash. *Phys. Rep.*, 333:121, 2000.

[92] D. Page, M. Prakash, J.M. Lattimer, and A.W. Steiner. *Phys. Rev. Lett*, 85:2048, 2000.

[93] N.K. Glendenning, S. Pei, and F. Weber. *Phys. Rev. Lett.*, 79:1603, 1997.

[94] G.E. Brown. *Nucl. Phys. A*, 574:217, 1994.

[95] G.E. Brown and H.A. Bethe. *Astrophys. J.*, 423:659, 1994.

[96] N.K. Glendenning. *Astrophys. J.*, 448:797, 1995.

[97] T.W. Baumgarte, S.L. Shapiro, and T.A. Teukolsky. *Astrophys. J.*, 458:1996, 1996.

[98] A. Burrows. *Astrophys. J.*, 334:897, 1988.

[99] F.-K. Thielemann, M. Hashimoto, and K. Nomoto. *Astrophys. J.*, 349:22, 1990.

[100] H.A. Bethe and G.E. Brown. *Astrophys. J. Lett.*, 445:L29, 1995.

[101] O.E.B. Messer, A. Mezzacappa, S.W. Bruenn, and M.W. Guidry. *Astrophys J.*, 507:353, 1998.

[102] S. Yamada, H-Th. Janka, and H. Suzuki. *Astron. Astrophys.*, 344:533, 1999.

[103] A. Burrows, T. Young, P. Pinto, R. Eastman, and T.A. Thompson. *Astrophys. J.*, 539:865, 2000.

[104] M. Rampp and H-Th. Janka. *Astrophys. J.*, 539:L33, 2000.

[105] M. Liebendoerfer, A. Mezzacappa, F.-K. Theilemann, O. E. Bronson Messer, and W. Rapheal Hix. *Phys. Rev. D*, 63:103004, 2001.

[106] M. Alford, K. Rajagopal, and F. Wilczek. *Nucl. Phys. B*, 537:443, 1999.

[107] M. Alford, K. Rajagopal, and F. Wilczek. *Nucl. Phys. B*, 558:219, 1999.

[108] R. Rapp, T. Schäffer, E. V. Shuryak, and M. Velkovsky. *Ann. Phys.*, 280:35, 2000.

[109] K. Rajagopal and F. Wilczek. *At the Frontier of Particle Physics / Handbook of QCD*. World Scientific, 2000.

[110] K. Iida and G. Baym. *Phys. Rev. D*, 63:074018, 2001.

[111] M. Alford and K. Rajagopal. *hep-ph/0204001*, 2002.

[112] P. Amore, M. C. Birse, J. A. McGovern, and N. R. Walet. *Phys. Rev. D*, 66:074005, 2002.

[113] M. Buballa and M. Oertel. *Nucl. Phys. A*, 703:770, 2002.

[114] F. Gastineau, R. Nebauer, and J. Aichelin. *hep-ph/0101289*, 2001.

[115] K. Rajagopal and F. Wilczek. *Phys. Rev. Lett.*, 86:3492, 2000.

[116] J. Kundu and K. Rajagopal. *Phys. Rev. D*, 65:094022, 2002.

[117] P. F. Bedaque and T. Schäfer. *Nucl. Phys. A*, 697:802, 2002.

[118] J. A. Bowers and K. Rajagopal. *hep-ph/0204079*, 2002.

[119] J. I. Kapusta. *Finite-Temperature Field Theory*. Cambridge University Press, Cambridge, U. K., 1985.

Appendix A

Thermodynamical Potential in the Hadronic Phase

In the mean-field approximation, the meson fields appearing in Eq. (2.1) may be replaced by their ground-state expectation values [30]:

$$\sigma \to \sigma \qquad \omega \to \delta_{\mu 0}\omega_0 \qquad \rho \to \delta_{\mu 0}\rho_0 \,. \tag{A.1}$$

For matter that is static and uniform, these quantities are constants. The Kronecker delta functions in the last two relations ensure rotational invariance. Use of these mean fields in Eq. (2.1) results in

$$\begin{aligned}\mathcal{L} \;=\; & \sum_B \bar{B}\left(i\gamma^\mu\partial_\mu - g_{\omega B}\gamma^0\omega_0 - g_{\rho B}\gamma^0\rho_0 t_{3B} - M_B + g_{\sigma B}\sigma - \mu_B\gamma_0\right)B \\ & -\frac{1}{2}m_\sigma^2\sigma^2 - \frac{\kappa}{3!}\sigma^3 - \frac{\lambda}{4!}\sigma^4 \\ & +\frac{1}{2}m_\omega^2\omega_0^2 + \frac{\zeta}{4!}g_\omega^4\omega_0^4 + \frac{1}{2}m_\rho^2\rho_0^2 + \frac{\xi}{4!}g_\rho^4\rho_0^4 \,.\end{aligned} \tag{A.2}$$

This is analogous to the Dirac Lagrangian for free baryons, but with an effective mass $M_B^* = M_B - g_{\sigma B}\sigma$ and an effective chemical potential $\nu_B = \mu_B + g_{\omega B}\omega_0 + g_{\rho B}t_{3B}\rho_0$. The thermodynamic potential per unit volume and energy density are given by [119]

$$\begin{aligned}-\frac{\Omega}{V} = \;\; P = \;\; & 2T\sum_B \int \frac{d^3k}{(2\pi)^3}\ln\left(1+e^{-(E_B-\nu_B)/T}\right) \\ & -\frac{1}{2}m_\sigma^2\sigma^2 + \frac{1}{2}m_\omega^2\omega_0^2 + \frac{1}{2}m_\rho^2\rho_0^2 \\ & -\frac{\kappa}{6}\sigma^3 - \frac{\lambda}{24}\sigma^4 + \frac{\zeta}{24}g_\omega^4\omega_0^4 + \frac{\xi}{24}g_\rho^4\rho_0^4 \\ \varepsilon = \;\; & \sum_B \int \frac{d^3k}{(2\pi)^3}\frac{E_B}{(1+e^{(E_B-\nu_B)/T})}\end{aligned}$$

$$\begin{aligned} & +\frac{1}{2}m_\sigma^2\sigma^2 + \frac{1}{2}m_\omega^2\omega_0^2 + \frac{1}{2}m_\rho^2\rho_0^2 \\ & +\frac{\kappa}{6}\sigma^3 + \frac{\lambda}{24}\sigma^4 + \frac{\zeta}{8}g_\omega^4\omega_0^4 + \frac{\xi}{8}g_\rho^4\rho_0^4 \,,\end{aligned} \tag{A.3}$$

where we have defined $E_B^2 = M_B^{*2} + k^2$. The Euler-Lagrange equations for the meson fields are

$$\begin{aligned} m_\sigma^2\sigma &= -\frac{\kappa}{2}\sigma^2 - \frac{\lambda}{6}\sigma^3 + \sum_B g_{\sigma B}\left\langle\bar{B}B\right\rangle \\ m_\omega^2\omega_0 &= -\frac{\zeta}{6}g_\omega^4\omega_0^3 + \sum_B g_{\omega B}\left\langle\bar{B}\gamma_0 B\right\rangle \\ m_\rho^2\rho_0 &= -\frac{\xi}{6}g_\rho^4\rho_0^3 + \sum_B g_{\rho B}\left\langle\bar{B}\gamma_0 B\right\rangle \,.\end{aligned} \tag{A.4}$$

The expectation values of the field operators are

$$\begin{aligned}\left\langle\bar{B}B\right\rangle &= 2\int\frac{d^3p}{(2\pi)^3}\left(1+e^{(E_B-\nu_B)/T}\right) \\ \left\langle\bar{B}\gamma_0 B\right\rangle &= 2\int\frac{d^3p}{(2\pi)^3}\frac{M_B^*}{E_B}\left(1+e^{(E_B-\nu_B)/T}\right) \,.\end{aligned} \tag{A.5}$$

These results are utilized for the equation of state in Chapter 2.

Appendix B

Neutrino-Quark Scattering

In this Appendix, we include a derivation of Eqs. (3.5) and (3.8) as well as extend the analytic results of neutrino quark scattering originally derived in Refs. [85, 81]. Also, the analytic results are compared with the exact calculation.

B.1 Evaluation of the Angular Integrals from Eqs. (3.5) and (3.8)

B.1.1 The integral I_a in Eq. (3.5)

The integral in Eq. (3.5) reads as

$$I_a = \int d\Omega_2 d\Omega_3 d\Omega_4 \left(E_1 E_2 - \vec{p_1}\cdot\vec{p_2}\right)\left(E_3 E_4 - \vec{p_3}\cdot\vec{p_4}\right)\delta^3\left(\vec{p_1}+\vec{p_2}-\vec{p_3}-\vec{p_4}\right) . \tag{B.1}$$

Defining $\vec{P} = \vec{p_1} + \vec{p_2}$, the delta function can be rewritten as

$$p_4^{-2}\delta\left(p_4 - |\vec{P} - \vec{p_3}|\right)\delta^2\left(\Omega_4 - \Omega_{|\vec{P}-\vec{p_3}|}\right) . \tag{B.2}$$

The two-dimensional delta function may be used to perform the Ω_4 integral, which gives unity. Now define x as the cosine of the angle between $\vec{P}$ and $\vec{p_3}$ so that $d\Omega_3 = d\phi dx$. The one-dimensional delta function then becomes

$$\delta\left(p_4 - |\vec{P} - \vec{p_3}|\right) = \frac{p_4}{p_3 P}\delta\left(x - \left(\frac{P^2 + p_3^2 - p_4^2}{2p_3 P}\right)\right) . \tag{B.3}$$

The dot product of $\vec{p_3}$ and $\vec{p_4}$ can be rewritten by eliminating x:

$$\vec{p_3}\cdot\vec{p_4} = \vec{p_3}\cdot(\vec{P} - \vec{p_3}) = p_3 P x - p_3^2 = \frac{P^2 - p_4^2 - p_3^2}{2} . \tag{B.4}$$

The ϕ integral gives 2π, and after integrating over x, we get

$$I_a = \frac{2\pi}{p_3 p_4}\int d\Omega_2 \frac{1}{P}\left(E_1 E_2 - \vec{p_1}\cdot\vec{p_2}\right)\left(E_3 E_4 + \left(p_3^2 + p_4^2 - P^2\right)/2\right) . \tag{B.5}$$

We must remember that we are limited by $|x| < 1$, so there are restrictions on P:

$$P < p_3 + p_4 , \qquad \text{and} \qquad P > |p_3 - p_4| . \tag{B.6}$$

Now, define y as the cosine of the angle between $\vec{p_1}$ and $\vec{p_2}$ so that we may write $d\Omega_2 = d\phi_2 dy$ and $P^2 = p_1^2 + p_2^2 + 2p_1 p_2 y$. Noting that $PdP = p_1 p_2 dy$, the integral becomes

$$I_a = \frac{4\pi^2}{p_1 p_2 p_3 p_4}\int_{P_{\min}}^{P_{\max}}\left(A - P^2/2\right)\left(B - P^2/2\right)dP , \tag{B.7}$$

where

$$\begin{aligned} A &= \left(2E_1 E_2 + p_1^2 + p_2^2\right)/2 , \\ B &= \left(2E_3 E_4 + p_3^2 + p_4^2\right)/2 , \\ P_{\min} &= \max\left(|p_1 - p_2|, |p_3 - p_4|\right) , \text{and} \\ P_{\max} &= \min\left(p_1 + p_2, p_3 + p_4\right) . \end{aligned} \tag{B.8}$$

After performing the P integral, we arrive at

$$\begin{aligned} I_a &= \frac{\pi^2}{5p_1 p_2 p_3 p_4}\left[3\left(P_{\max}^5 - P_{\min}^5\right) - 10\left(A + B\right)\left(P_{\max}^3 - P_{\min}^3\right) + \right. \\ &\quad \left. 60AB\left(P_{\max} - P_{\min}\right)\right] . \end{aligned} \tag{B.9}$$

This is the result in Eq. (3.6).

B.1.2 The integral I_b in Eq. (3.8)

The integral I_b has the form

$$I_b = \int d\Omega_2 d\Omega_3 d\Omega_4 \left(E_1 E_2 - \vec{p_1}\cdot\vec{p_4}\right)\left(E_3 E_4 - \vec{p_3}\cdot\vec{p_2}\right)\delta^3\left(\vec{p_1}+\vec{p_2}-\vec{p_3}-\vec{p_4}\right) . \tag{B.10}$$

With $\vec{P} = \vec{p_4} - \vec{p_1}$, the delta function may be written as

$$p_2^{-2}\delta\left(p_2 - |\vec{P} + \vec{p_3}|\right)\delta^2\left(\Omega_2 - \Omega_{|\vec{P}+\vec{p_3}|}\right) . \tag{B.11}$$

Integration over Ω_2 yields unity because of the two-dimensional delta function. Now define x as the cosine of the angle between $\vec{P}$ and $\vec{p_3}$ so that $d\Omega_3 = d\phi dx$. The one-dimensional delta function becomes

$$\delta\left(p_2 - |\vec{P} + \vec{p_3}|\right) = \frac{p_2}{p_3 P}\delta\left(x - \left(\frac{p_2^2 - P^2 - p_3^2}{2p_3 P}\right)\right) . \tag{B.12}$$

The dot product of $\vec{p_2}$ and $\vec{p_3}$ can be rewritten by eliminating x:

$$\vec{p_2}\cdot\vec{p_3} = \vec{p_3}\cdot(\vec{P} + \vec{p_3}) = p_3 P x + p_3^2 = \frac{p_3^2 + P^2 - p_2^2}{2} . \tag{B.13}$$

Performing the integral over x, we obtain

$$I_b = \frac{2\pi}{p_3 p_2}\int d\Omega_4 \frac{1}{P}\left(E_1 E_4 - \vec{p_1}\cdot\vec{p_4}\right)\left(E_3 E_4 + \left(P^2 - p_2^2 - p_3^2\right)/2\right) . \tag{B.14}$$

There are again restrictions on P:

$$P < p_2 + p_3 , \qquad \text{and} \qquad P > |p_2 - p_3| . \tag{B.15}$$

Now, define y as the cosine of the angle between $\vec{p_1}$ and $\vec{p_4}$ so that $d\Omega_4 = d\phi_4 dy$ and $P^2 = p_1^2 + p_4^2 - 2p_1 p_4 y$. The integral then becomes

$$I_b = \frac{4\pi^2}{p_1 p_2 p_3 p_4}\int_{P_{\min}}^{P_{\max}}\left(P^2/2 - C\right)\left(P^2/2 - D\right) dP \tag{B.16}$$

where

$$\begin{aligned} C &= \left(-2E_3 E_2 + p_3^2 + p_2^2\right)/2 , \\ D &= \left(-2E_1 E_4 + p_1^2 + p_4^2\right)/2 , \\ P_{\min} &= \max\left(|p_1 - p_4|, |p_2 - p_3|\right) , \text{and} \\ P_{\max} &= \min\left(p_2 + p_3, p_1 + p_4\right) . \end{aligned} \tag{B.17}$$

This result is equivalent to the replacements $p_2 \leftrightarrow p_4$ and $E_2 \leftrightarrow -E_4$ in the result for integral I_a (Eqs. (B.7) and (B.8)) as mentioned in connection with Eq. (3.8). It is worthwile to note that, when the neutrino momentum p_4 may be neglected in comparison with other momenta, the conditions on P in Eqs. (B.8) and (B.17) reduce to the "triangle inequalities"

$$p_1 > |p_2 - p_3| , \qquad p_2 > |p_1 - p_3| , \qquad \text{and} \qquad p_3 > |p_1 - p_2| . \tag{B.18}$$

which are encountered in the evaluation of the quark direct Urca process.

The calculation of the integral I_c in Eq. (3.8) proceeds exactly as the calculation for I_a above, but with the replacements noted in Eq. (3.8).

B.2 Scattering of Degenerate Neutrinos

In the neutron star problem the quarks are always degenerate, since quark chemical potentials are on the order of hundreds of MeV, while the temperature is no more than tens of MeV. Since only particles near the Fermi surface are allowed to participate in scattering reactions with neutrinos, an excellent first approximation is to replace the quark energies by their chemical potentials: $E_2 \approx \mu_2 = \mu_4 \approx E_4 \Rightarrow E_3 \approx E_1$. This justifies an expansion in terms of the neutrino energy transfer $q_0 \equiv E_1 - E_3$. In this section, we will treat the neutrinos as degenerate, and the next section will consider the case in which the neutrinos are non-degenerate.

B.2.1 Results to leading order in energy transfer q_0

The replacement of the quark energies by chemical potentials allows us to separate the energy integral from the angular integral. The energy integral

$$\begin{aligned} I_E &= \int dE_2 dE_3 dE_4 \left(E_2 E_4 \frac{E_3}{E_1}\right)\delta(E_1 + E_2 - E_3 - E_4) \\ &\quad \times f_2\left(1 - f_3\right)\left(1 - f_4\right) \end{aligned} \tag{B.19}$$

can be calculated analytically; the result is

$$I_E = \mu_2^2\left(\frac{T^2\pi^2 + \left(E_1 - \mu_1\right)^2}{2\left(1 + e^{(E_1 - \mu_1)/T}\right)}\right) \approx \frac{\pi^2}{4}\mu_2^2 T^2 . \tag{B.20}$$

For massless quarks, the term involving I_c does not contribute. In the limit $\mu_2 > E_1$, the remaining integrals can be simplified. Explicitly,

$$\begin{aligned} I_a &\approx \frac{4\pi^2}{p_1 p_2 p_3 p_4}\int_{|\mu_2 - E_1|}^{|\mu_2 + E_1|}\frac{dP}{4}\left(P^2 - \alpha\right)^2 \approx \frac{4\pi^2}{\mu_2^2 E_1^2}\int_{\mu_2 - E_1}^{\mu_2 + E_1}\frac{dP}{4}\left(P^2 - \alpha\right)^2 \\ &= \frac{16\pi^2 E_1}{15\mu_2^2}\left(10\mu_2^2 + 5\mu_2 E_1 + E_1^2\right) , \\ I_b &\approx \frac{4\pi^2}{p_1 p_2 p_3 p_4}\int_{|\mu_2 - E_1|}^{|\mu_2 + E_1|}\frac{dP}{4}\left(P^2 - \beta\right)^2 \approx \frac{4\pi^2}{\mu_2^2 E_1^2}\int_{\mu_2 - E_1}^{\mu_2 + E_1}\frac{dP}{4}\left(P^2 - \beta\right)^2 \\ &= \frac{16\pi^2 E_1}{15\mu_2^2}\left(10\mu_2^2 - 5\mu_2 E_1 + E_1^2\right) . \end{aligned} \tag{B.21}$$

where $\alpha = (\mu_2 + E_1)^2$, $\beta = (\mu_2 - E_1)^2$. In obtaining this result, we have used that $E_2 \approx E_4 \approx \mu_2$ and $E_1 \approx E_3$. The case $\mu_2 < E_1$ may be treated by the

replacement $|\mu_2 - E_1| = E_1 - \mu_2$ in the limits of the integral. Collecting these results, we arrive at

$$\begin{aligned}\frac{\sigma_{DS}}{V} &= \frac{G_F^2\mu_2^3}{5\pi^3}\left[(E_1-\mu_1)^2+\pi^2T^2\right]\left(\frac{xE_1}{\mu_2}\right)^{1/2}\times \\ &\quad \left[\left(\mathcal{V}^2+\mathcal{A}^2\right)\left(10+x^2\right)+5\left(2\mathcal{V}\mathcal{A}\right)x\right], \end{aligned} \tag{B.22}$$

where $x = \min(\mathrm{E}_1, \mu_2)/\max(\mathrm{E}_1, \mu_2)$. This is the result quoted in Eq. (3.9) [85, 81].

B.2.2 Results to all orders in q_0 for the case $\mu_2 > E_1$

In this case, we cannot replace E_2 and E_4 with their chemical potentials, nor replace E_3 with E_1 in I_E, I_a and I_b. Because I_a and I_b now depend on $q_0 \equiv E_1 - E_3$, E_2, and E_4, the energy integrals cannot be performed independently of the angular integrals. The angular integrals are:

$$\begin{aligned} I_a &= \int_{P_{\min 1}}^{P_{\max 1}} \frac{dP}{4}\left(\mathcal{V}+\mathcal{A}\right)^2\left(P^2-A\right)\left(P^2-B\right) \\ I_b &= \int_{P_{\min 2}}^{P_{\max 2}} \frac{dP}{4}\left(\mathcal{V}-\mathcal{A}\right)^2\left(P^2-C\right)\left(P^2-D\right) \\ P_{\min 1} &= \max\left(|E_1-E_2|, |E_3-E_4|\right) \\ P_{\max 1} &= \min\left(|E_1+E_2|, |E_3+E_4|\right) = E_1+E_2 \\ P_{\min 2} &= \max\left(|E_3-E_2|, |E_1-E_4|\right) = |E_3-E_2| \\ P_{\max 2} &= \min\left(|E_3+E_2|, |E_1+E_4|\right) . \end{aligned} \tag{B.23}$$

The quantities A, B, C, and D are defined in section B.1 above.

The energy delta function may be used to eliminate E_4 everywhere. We then reduce the limits on the P integrals to a "closed form" by ensuring that for each integral, the lower limit is smaller than the upper limit and that there are no absolute value signs. $P_{\min 1}$ can be simplified to $\max\left(|a|, |a-2q_0|\right)$, where $a = E_1 - E_2$. The equation $|a| > |a - 2q_0|$ can be satisfied in two cases:

1. $\mathbf{a > 0}$: $a > |a-2q_0| \Rightarrow (a > 2q_0 \text{ and } q_0 > 0) \text{ or } (a < 2q_0 \text{ and } a > -q_0)$,
2. $\mathbf{a < 0}$: $-a > |a-2q_0| \Rightarrow (a > 2q_0 \text{ and } a < q_0) \text{ or } (a < 2q_0 \text{ and } q_0 < 0)$.

Similarly, the equation $|a| < |a - 2q_0|$ can be satisfied in two cases:

1. $\mathbf{a > 0}$: $a < |a-2q_0| \Rightarrow (a > 2q_0 \text{ and } q_0 < 0) \text{ or } (a < 2q_0 \text{ and } a < q_0)$,

2. $\mathbf{a < 0}$: $-a < |a-2q_0| \Rightarrow (a > 2q_0 \text{ and } a > q_0) \text{ or } (a < 2q_0 \text{ and } q_0 > 0)$.

The quantitiy $P_{\max 2} = E_3 + E_2 = E_1 - q_0 + E_2$ when $q_0 > 0$ and $E_1 + E_4 = E_2 + E_1 + q_0$ when $q_0 < 0$. Similarly, $P_{\min 2} = E_3 - E_2 = E_1 - q_0 - E_2$ when $E_2 < E_1 - q_0$ and $E_2 - E_3 = E_2 - E_1 + q_0$ when $E_2 > E_1 - q_0$. Utilizing these results, the cross section per unit volume may be written as

$$\begin{aligned}\frac{\sigma}{V} &= \int_0^{E_1/2} dq_0 \int_0^{E_1-2q_0} dE_2 \int_{E_1-E_2}^{E_1+E_2} dP f_A \\ &+ \int_0^{E_1/2} dq_0 \int_{E_1-2q_0}^{E_1-q_0} dE_2 \int_{E_1-E_2}^{E_1+E_2} dP f_A \\ &+ \int_{-\infty}^{0} dq_0 \int_{E_1-q_0}^{E_1-2q_0} dE_2 \int_{E_2-E_1}^{E_1+E_2} dP f_A \\ &+ \int_{-\infty}^{0} dq_0 \int_{E_1-2q_0}^{\infty} dE_2 \int_{E_2-E_1}^{E_1+E_2} dP f_A \\ &+ \int_{-E_2}^{0} dq_0 \int_0^{E_1-2q_0} dE_2 \int_{E_1-E_2-2q_0}^{E_1+E_2} dP f_A \\ &+ \int_0^{E_1} dq_0 \int_{E_1-q_0}^{E_1} dE_2 \int_{E_2-E_1+2q_0}^{E_1+E_2} dP f_A \\ &+ \int_{-E_2}^{0} dq_0 \int_{E_1}^{E_1-q_0} dE_2 \int_{E_1-E_2-2q_0}^{E_1+E_2} dP f_A \\ &+ \int_0^{E_1} dq_0 \int_{E_1}^{\infty} dE_2 \int_{E_2-E_1+2q_0}^{E_1+E_2} dP f_A \\ &+ \int_{-\infty}^{0} dq_0 \int_{-q_0}^{E_1-q_0} dE_2 \int_{E_2+E_1+q_0}^{E_1-E_2-q_0} dP f_B \\ &+ \int_{-\infty}^{0} dq_0 \int_{E_1-q_0}^{\infty} dE_2 \int_{E_2+E_1+q_0}^{E_2-E_1+q_0} dP f_B \\ &+ \int_0^{E_1} dq_0 \int_0^{E_1-q_0} dE_2 \int_{E_1+E_2-q_0}^{E_1-E_2-q_0} dP f_B \\ &+ \int_0^{E_1} dq_0 \int_{E_1-q_0}^{\infty} dE_2 \int_{E_1+E_2-q_0}^{E_2-E_1+q_0} dP f_B \end{aligned} \tag{B.24}$$

where,

$$\begin{aligned} f_A &\equiv \frac{3G_F^2}{16\pi^3E_1^2} f_2\left(1-f_3\right)\left(1-f_4\right)\left(\mathcal{V}+\mathcal{A}\right)^2\left(P^2-A\right)\left(P^2-B\right) \\ f_B &\equiv \frac{3G_F^2}{16\pi^3E_1^2} f_2\left(1-f_3\right)\left(1-f_4\right)\left(\mathcal{V}-\mathcal{A}\right)^2\left(P^2-C\right)\left(P^2-D\right) \end{aligned} \tag{B.25}$$

The first, second, sixth, and eighth integrals in Eq. (B.24) contribute to f_A for different ranges of E_2 to the integral when q_0 is positive, and the third, fourth,

fifth, and seventh integrals contribute to f_A for the same ranges of E_2 when q_0 is negative. The upper limit in the first two integrals is further restricted to $q_0 < E_1/2$, since otherwise, $E_1 - 2q_0 < 0$ and the upper limits are smaller than the lower limits. The contributions to f_B can be analyzed similarly.

The E_2 integrals are of the form L_n, given below in section B.4. In the case $\mu_2 > E_1$, $a < 0$ for all of the polylogarithmic integrals except for $E_2 = \infty$. When $a < 0$, the polylogarithms vanish, and so the integrals vanish unless the upper limit is infinite. The asymptotic values of the L_n at $-\infty$ give

$$\begin{aligned}\frac{\sigma_{DS}}{V} &= \int_{-\infty}^{0} dq_0 \frac{F q_0 G_F^2 E_1}{15\pi^3}\left[\left(\mathcal{V}^2+\mathcal{A}^2\right)F_{1,-} + (2\mathcal{V}\mathcal{A})\,F_{2,-}\right] \\ &+ \int_{0}^{E_1} dq_0 \frac{F q_0 G_F^2}{15\pi^3 E_1^2}\left[\left(\mathcal{V}^2+\mathcal{A}^2\right)F_{1,+} + (2\mathcal{V}\mathcal{A})\,F_{2,+}\right], \qquad \text{(B.26)}\end{aligned}$$

where F is the factor $(1 - f_3(E_3))\,(1 - e^{-z})^{-1}$, $zT \equiv q_0 - \mu_2 + \mu_4$, and $F_{(1\text{or}2),\pm}$ are given by

$$\begin{aligned}F_{1,-} &= +60\mu_2^2 + 6E_1^2 + 20\pi^2T^2 - 15E_1q_0 + 20q_0^2 \\ F_{2,-} &= 30\mu_2E_1 - 60\mu_2q_0 \\ F_{1,+} &= \mu_2^2\left(60E_1^3 - 180q_0E_1^2 + 180q_0^2E_1 - 60q_0^3\right) \\ &\quad +6E_1^5 - 15q_0E_1^4 + 20q_0^2E_1^3 - 30q_0^3E_1^2 + 30q_0^4E_1 - 11q_0^5 \\ &\quad +\pi^2T^2\left(20E_1^3 - 60q_0E_1^2 + 60q_0^2E_1 - 20q_0^3\right) \\ F_{2,+} &= +30\mu_2E_1^4 - 60q_0\mu_2E_1^3 + 60q_0^3\mu_2E_1 - 30q_0^4\mu_2 \qquad \text{(B.27)}\end{aligned}$$

The q_0 integrations are detailed in section B.4. The final result is

$$\begin{aligned}\frac{\sigma_{DS}}{V} &= \frac{G_F^2T^2}{20E_1\pi^3}\left[\left(\mathcal{V}^2+\mathcal{A}^2\right)\left(20\mu_2^2E_1^2\pi^2 + 420\zeta(3)\mu_2^2E_1T\right.\right. \\ &\quad \left.+15\mu_2^2\pi^4T^2 + 2E_1^4\pi^2 + 10E_1^2\pi^4T^2 + 140\zeta(3)E_1\pi^2T^3\right) \\ &\quad \left.+\,(2\mathcal{V}\mathcal{A})\,10\mu_2E_1^3\pi^2\right]. \qquad \text{(B.28)}\end{aligned}$$

Figure B.1 shows the result above, in addition to the exact result from Eqs. (3.4) through (3.8) and the first order result of Eq. (B.22). The first order result gives a good representation of the exact cross section, and the higher-order approximation is nearly indistinguishable from the exact cross section.

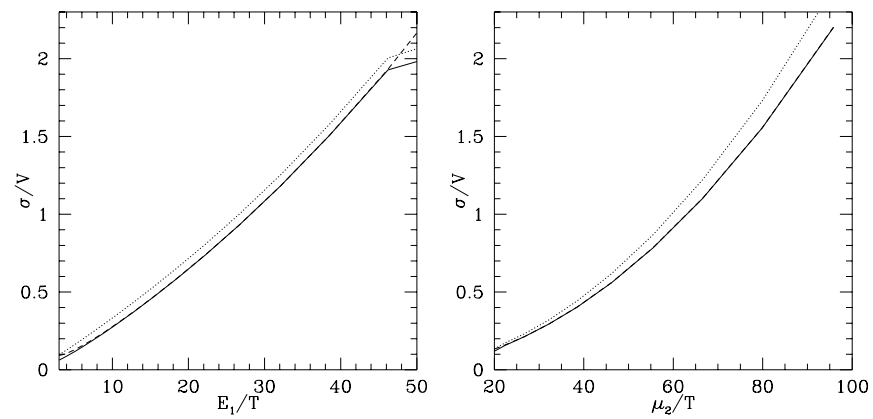

Figure B.1: The cross section per unit volume for neutrino scattering from quarks. The top panel varies the incoming neutrino energy (E_1) and fixes the quark chemical potential at $\mu_2 = \mu_4 = 50T$. The bottom panel varies the quark chemical potential $\mu_2 = \mu_4$ and fixes the neutrino energy $E_1 = 20T$. In both panels the solid line is the exact result from Eqs. (3.4) through (3.8), the dotted lines is the first order result of Eq. (B.22), and the dashed line (often hidden under the solid line) is Eq. (B.28)

B.3 Scattering of Non-Degenerate Neutrinos

The analysis up to Eq. (B.26) is correct also for lowest-order results for the scattering of non-degenerate neutrinos, because the essential aspects depend only on the degeneracy of the quarks, not the degeneracy of the neutrinos. The terms of highest order in μ_2 from equation (B.27) give

$$\begin{aligned}\frac{\sigma_{NDS}}{V} &= \frac{4G_F^2\mu_2^2\left(\mathcal{V}^2+\mathcal{A}^2\right)}{\pi^3}\left[\int_{-\infty}^{0} dq_0 q_0 E_1 - \right.\\ &\left.\int_0^{E_1} dq_0 \frac{q_0}{E_1^2}\left(q_0^3 - 3q_0^2E_1 + 3q_0E_1^2 - E_1^3\right)\right]. \end{aligned} \tag{B.29}$$

The first q_0 integral is negligible because it is a function of powers of the temperature instead of powers of E_1. The q_0 integration effectively replaces q_0^n with $E_1^{n+1}/(n+1)$ (see section B.4). This gives

$$\frac{\sigma_{NDS}}{V} = \frac{G_F^2\mu_2^2E_1^3(\mathcal{V}^2+\mathcal{A}^2)}{5\pi^3}. \tag{B.30}$$

This reproduces the formula from [81].

B.4 Integrals Expressible as Polylogarithms

The integrals L_n defined by

$$L_n = \int dE_2 \frac{E_2^n}{\left(1+e^a\right)\left(1+e^{-a-z}\right)} \tag{B.31}$$

where $a \equiv (E_2-\mu_2)/T$, and $z \equiv q_0/T$ can be expressed in terms of polylogarithms

$$L_n(E_2) = \frac{T}{1-e^{-z}}\sum_{j=0}^{n}(-1)^{j+n+1}E_n^{n-j}T^j\frac{n!}{(n-j)!}\xi_n, \tag{B.32}$$

where $\xi_n = \mathrm{Li}_n(-e^a) - \mathrm{Li}_n(-e^{a+z})$. When $E_2 \to \infty$, the integrals are given by

$$\begin{aligned} L_0 &= Tz \\ L_1 &= \frac{Tz}{2}\left(2\mu_2 - Tz\right) \\ L_2 &= \frac{Tz}{3}\left(3\mu_2^2 - 3Tz\mu_2 + z^2T^2 + \pi^2T^2\right). \end{aligned} \tag{B.33}$$

The q_0 integrals in Eqs. (B.26) and (B.27) can be written explicitly in terms of polylogarithmic functions:

$$\begin{aligned}\chi I_n &= \chi\int_0^x \frac{z^n}{\left(1-e^{-z}\right)\left(1+e^{z+h}\right)}dz \\ &= \sum_{k=1}^{n+1}\left[\left(\frac{-d}{dx}\right)^{k-1} z^n\right]\left[\mathrm{Li}_k\left(-e^{x+h}\right) - \mathrm{Li}_k\left(e^x\right)\right] \end{aligned} \tag{B.34}$$

where $x = E_1/T$, $z = q_0/T$, $\chi = 1+e^h$ and $h = (\mu_1 - E_1)/T$. Here, we collect some useful resutls by neglecting terms of order e^{-x}.

For degenerate scattering, $h = 0$, and it is convenient to separate the integrals into the positive and negative regions of z:

$$\begin{aligned}\chi I_{n,+} &\approx \chi\int_0^\infty \frac{z^n}{\left(1-e^{-z}\right)\left(1+e^{z}\right)}dz \\ \chi I_{n,-} &\approx \chi\int_{-\infty}^0 \frac{z^n}{\left(1-e^{-z}\right)\left(1+e^{z}\right)}dz \\ I_{1,+} &= I_{1,-} \approx \frac{\pi^2}{8} \\ I_{2,+} &= -I_{2,-} = \frac{7}{4}\zeta(3) \\ I_{3,+} &= I_{3,-} \approx \frac{\pi^4}{16} \\ I_{4,+} &= -I_{4,-} \approx \frac{93}{4}\zeta(5) \\ I_{5,+} &= -I_{5,-} \approx \frac{\pi^6}{8}. \end{aligned} \tag{B.35}$$

For non-degenerate scattering, $h \to -\infty$, we can ignore the latter term in the denominator of Eq. (B.34). The integrals $I_{n,-}$ in this case are proportional to powers of the temperature and can therefore be neglected. The remaining positive portions give

$$I_{n,+} \approx \frac{x^{n+1}}{n+1}. \tag{B.36}$$

This result is used for the integrals in Eq. (B.29).

Appendix C

Color Superfluidity

In this Appendix, the Lagrangian in Eq. (5.2) is treated in the mean-field approximation from which the corresponding thermodynamic potential is derived. This result enables the calculation of all other physical quantities.

C.1 The Derivation of the Mean-Field Lagrangian

We note first that $\bar{q}q^C$ is a pseudoscalar under Lorentz transformations, while $\bar{q}^C\gamma^5 q$ is a scalar. Instanton interactions are known to favor the scalar interactions at high density [42, 43], so we will take the pseudoscalar contribution to be zero. The Lagrangian (without the psedoscalar terms) from Eq. (5.2) is [113, 114]:

$$\begin{aligned}\mathcal{L} &= \bar{q}_f\left(i\partial\!\!\!/ - m_{0f} - \mu_f\gamma_0\right)q_f + G_S\sum_{a=0}^{8}\left(\bar{q}\lambda_f^a q\right)^2 \\ &\quad + G_{DIQ}\sum_k\sum_\gamma\left(\bar{q}_{i\alpha}i\gamma^5\epsilon^{ijk}\epsilon^{\alpha\beta\gamma}q^C_{j\beta}\right)\left(\bar{q}^C_{i'\alpha'}i\gamma^5\epsilon^{i'j'k}\epsilon^{\alpha'\beta'\gamma}q_{j'\beta'}\right) \\ &\quad - G_D\left[\det{}_f\bar{q}\left(1-i\gamma^5\right)q + \det{}_f\bar{q}\left(1+i\gamma^5\right)q\right], \end{aligned} \tag{C.1}$$

where color is represented by Greek indices, flavor by Latin indices, $\lambda^0 = \sqrt{2/3}I_{3\times3}$, and the charge conjugate Dirac spinors are defined by ($C\gamma^\mu C = \gamma^{\mu T}$ and $C^T = -C$)

$$q^C \equiv C\bar{q}^T \quad \text{and} \quad \bar{q}^C = \left(C\bar{q}^T\right)^\dagger\gamma^0 = \bar{q}^*C^\dagger\gamma^0 = -q^T\gamma^{0*}C\gamma^0 = q^TC\,. \tag{C.2}$$

Note that the chemical potential terms are unaffected by the manipulations that follow.

In the mean-field approximation, the four- and six-fermion interactions may be written in terms of two-fermion interactions by applying the following rules [39]

$$\begin{aligned}\bar{\psi}_1\psi_1\bar{\psi}_2\psi_2 &\rightarrow \left\langle\bar{\psi}_1\psi_1\right\rangle\bar{\psi}_2\psi_2 + \bar{\psi}_1\psi_1\left\langle\bar{\psi}_2\psi_2\right\rangle - \left\langle\bar{\psi}_1\psi_1\right\rangle\left\langle\bar{\psi}_2\psi_2\right\rangle \\ \bar{\psi}_1\psi_1\bar{\psi}_2\psi_2\bar{\psi}_3\psi_3 &\rightarrow \left\langle\bar{\psi}_1\psi_1\right\rangle\left\langle\bar{\psi}_2\psi_2\right\rangle\bar{\psi}_3\psi_3 + \left\langle\bar{\psi}_1\psi_1\right\rangle\bar{\psi}_2\psi_2\left\langle\bar{\psi}_3\psi_3\right\rangle \\ &\quad + \bar{\psi}_1\psi_1\left\langle\bar{\psi}_2\psi_2\right\rangle\left\langle\bar{\psi}_3\psi_3\right\rangle \\ &\quad - 2\left\langle\bar{\psi}_1\psi_1\right\rangle\left\langle\bar{\psi}_2\psi_2\right\rangle\left\langle\bar{\psi}_3\psi_3\right\rangle\,. \end{aligned} \tag{C.3}$$

We begin with the G_S term in Eq. (C.1). Using the explicit form of the λ matrices, we may write

$$\begin{aligned}\textstyle\sum_{a=0}^8\left(\bar{q}\lambda^a q\right)^2 = &\ \tfrac{2}{3}\left(\bar{u}u\right)^2 + \tfrac{2}{3}\left(\bar{d}d\right)^2 + \tfrac{2}{3}\left(\bar{s}s\right)^2 && (a=0) \\ &+ \left(\bar{u}d\right)^2 + \left(\bar{d}u\right)^2 && (a=1) \\ &- \left(\bar{u}d\right)^2 - \left(\bar{d}u\right)^2 && (a=2) \\ &+ \left(\bar{u}u\right)^2 + \left(\bar{d}d\right)^2 && (a=3) \\ &+ \left(\bar{u}s\right)^2 + \left(\bar{s}u\right)^2 && (a=4) \\ &- \left(\bar{u}s\right)^2 - \left(\bar{s}u\right)^2 && (a=5) \\ &+ \left(\bar{d}s\right)^2 + \left(\bar{s}d\right)^2 && (a=6) \\ &- \left(\bar{d}s\right)^2 - \left(\bar{s}d\right)^2 && (a=7) \\ &\tfrac{1}{3}\left(\bar{u}u\right)^2 + \tfrac{1}{3}\left(\bar{d}d\right)^2 + \tfrac{4}{3}\left(\bar{s}s\right)^2 && (a=8)\end{aligned}$$

$$\sum_{a=0}^{8}\left(\bar{q}\lambda^a q\right)^2 = 2G_S\left[\left(\bar{u}u\right)^2 + \left(\bar{d}d\right)^2 + \left(\bar{s}s\right)^2\right]. \tag{C.4}$$

Utilizing the result in Eq. (C.3), and defining $\alpha \equiv \langle\bar{u}u\rangle$, $\beta \equiv \left\langle\bar{d}d\right\rangle$, and $\gamma \equiv \langle\bar{s}s\rangle$ gives

$$\sum_{a=0}^{8}\left(\bar{q}\lambda^a q\right)^2 = 2G_S\left[2\alpha\bar{u}u - \alpha^2 + 2\beta\bar{d}d - \beta^2 + 2\gamma\bar{s}s - \gamma^2\right]. \tag{C.5}$$

Employing the rule in Eq. (C.3), the term involving G_{DIQ} may be written as

$$G_{DIQ}\sum_k\sum_\gamma\left\langle\bar{q}_{i\alpha}i\gamma^5\epsilon^{ijk}\epsilon^{\alpha\beta\gamma}q^C_{j\beta}\right\rangle\left(\bar{q}^C_{i'\alpha'}i\gamma^5\epsilon^{i'j'k}\epsilon^{\alpha'\beta'\gamma}q_{j'\beta'}\right)$$

$$+\left(\bar{q}_{i\alpha}i\gamma^5\epsilon^{ijk}\epsilon^{\alpha\beta\gamma}q^C_{j\beta}\right)\left\langle\bar{q}^C_{i'\alpha'}i\gamma^5\epsilon^{i'j'k}\epsilon^{\alpha'\beta'\gamma}q_{j'\beta'}\right\rangle$$
$$-\left\langle\bar{q}_{i\alpha}i\gamma^5\epsilon^{ijk}\epsilon^{\alpha\beta\gamma}q^C_{j\beta}\right\rangle\left\langle\bar{q}^C_{i'\alpha'}i\gamma^5\epsilon^{i'j'k}\epsilon^{\alpha'\beta'\gamma}q_{j'\beta'}\right\rangle . \tag{C.6}$$

In what follows, the notation

$$\Delta^{k\gamma}\equiv\left\langle\bar{q}_{i'\alpha'}i\gamma^5\epsilon^{i'j'k}\epsilon^{\alpha'\beta'\gamma}q^C_{j'\beta'}\right\rangle \tag{C.7}$$

will be employed. Defining $\eta\equiv i\gamma^5\epsilon^{i'j'k}\epsilon^{\alpha'\beta'\gamma}=-\eta^\dagger$, the Hermitian conjugate of $\Delta^{k\gamma}$ is

$$\begin{aligned}\Delta^{k\gamma\dagger} &= -\left\langle q^{C\dagger}\eta\bar{q}^\dagger\right\rangle=-\left\langle\left(C\bar{q}^T\right)^\dagger\eta\left(q^\dagger\gamma^0\right)^\dagger\right\rangle\\ &= \left\langle q^T\gamma^{0*}C\eta\gamma^{0\dagger}q\right\rangle=-\left\langle q^TC\gamma^0\eta\gamma^{0\dagger}q\right\rangle\\ &= -\left\langle\bar{q}^C\gamma^0\eta\gamma^0q\right\rangle=\left\langle\bar{q}^C_{j'\beta'}i\gamma^5\epsilon^{i'j'k}\epsilon^{\alpha'\beta'\gamma}q_{i'\alpha'}\right\rangle .\end{aligned} \tag{C.8}$$

In this expression, we can relabel indices $i'\leftrightarrow j'$, $\alpha'\leftrightarrow\beta'$ and $k\leftrightarrow\gamma$ without changing the expression. Thus, the diquark term becomes

$$G_{DIQ}\sum_k\sum_\gamma\left[\left(\bar{q}^C_{i\alpha}i\gamma^5\epsilon^{ijk}\epsilon^{\alpha\beta\gamma}q_{j\beta}\right)\Delta^{k\gamma}+\left(\bar{q}_{i\alpha}i\gamma^5\epsilon^{ijk}\epsilon^{\alpha\beta\gamma}q^C_{j\beta}\right)\Delta^{k\gamma\dagger}-\Delta^{k\gamma}\Delta^{k\gamma\dagger}\right] . \tag{C.9}$$

The definitions (see Eq. (5.8))

$$\begin{aligned}\tilde{\Delta}^{ij}_{\alpha\beta} &\equiv 2G_{DIQ}i\gamma^5\epsilon^{ijk}\epsilon^{\alpha\beta\gamma}\Delta^{k\gamma}\\ \tilde{\Delta}^{ij\dagger}_{\alpha\beta} &\equiv 2G_{DIQ}i\gamma^5\epsilon^{ijk}\epsilon^{\alpha\beta\gamma}\Delta^{k\gamma\dagger},\end{aligned} \tag{C.10}$$

simplify the diquark terms in the Lagrangian to

$$\sum_k\sum_\gamma\left[\frac{1}{2}\bar{q}^C_{i\alpha}\tilde{\Delta}^{ij}_{\alpha\beta}q_{j\beta}+\frac{1}{2}\bar{q}_{i\alpha}\tilde{\Delta}^{ij\dagger}_{\alpha\beta}q^C_{j\beta}-\frac{\left|\tilde{\Delta}^{ij}_{\alpha\beta}\right|^2}{4G_{DIQ}}\right] . \tag{C.11}$$

For the term involving G_D in Eq. (C.1), the only purely scalar terms are the ones along the diagonal, where the flavor indexes are the same. Ignoring pseudoscalar terms, the determinant is given by the product of the terms along the diagonal. This gives

$$\begin{aligned}\rightarrow\ & -G_D\bar{u}\left(1-i\gamma^5\right)u\bar{d}\left(1-i\gamma^5\right)d\bar{s}\left(1-i\gamma^5\right)s\\ & -G_D\bar{u}\left(1+i\gamma^5\right)u\bar{d}\left(1+i\gamma^5\right)d\bar{s}\left(1+i\gamma^5\right)s\\ \rightarrow\ & -2G_D\bar{u}u\bar{d}d\bar{s}s .\end{aligned} \tag{C.12}$$

Utilizing Eq. (C.3) reduces the six-fermion interaction to a sum of two-fermion interactions, giving

$$-2G_D\left[\bar{u}u\beta\gamma+\bar{d}d\alpha\gamma+\bar{s}s\alpha\beta-2\alpha\beta\gamma\right] . \tag{C.13}$$

Collecting the results from Eqs. (C.5), (C.13), and (C.11), we have

$$\begin{aligned}\mathcal{L} &= \bar{q}\left(i\partial-m_{0f}\right)q\\ &\quad +2G_S\left[2\alpha\bar{u}u-\alpha^2+2\beta\bar{d}d-\beta^2+2\gamma\bar{s}s-\gamma^2\right]\\ &\quad -2G_D\left[\bar{u}u\beta\gamma+\bar{d}d\alpha\gamma+\bar{s}s\alpha\beta-2\alpha\beta\gamma\right]\\ &\quad +\sum_k\sum_\gamma\left[\frac{1}{2}\bar{q}^C_{i\alpha}\tilde{\Delta}^{ij}_{\alpha\beta}q_{j\beta}+\frac{1}{2}\bar{q}_{i\alpha}\tilde{\Delta}^{ij\dagger}_{\alpha\beta}q^C_{j\beta}-\frac{\left|\tilde{\Delta}^{ij}_{\alpha\beta}\right|^2}{4G_{DIQ}}\right] .\end{aligned} \tag{C.14}$$

The constant terms that do not involve any fields give constant terms of the same form in the thermodynamic potential given in Eq. (5.5). Eq. (C.14) above allows us to define an effective quark mass M for a quark with flavor i ($i\neq j\neq k$). Explicitly,

$$M_i=m_{0i}-4G_S\left\langle\bar{q}_iq_i\right\rangle+2G_D\left\langle\bar{q}_jq_j\right\rangle\left\langle\bar{q}_kq_k\right\rangle . \tag{C.15}$$

This is exactly the same form as Eq. (2.6), which is unchanged by the presence of the superconducting gap. Six-fermion interactions which mix contributions from $\langle qq\rangle$ and $\langle\bar{q}q\rangle$ condensates, which are not considered here, would modify this dynamically generated mass.

In the Nambu-Gorkov formalism, we construct 8-component spinors of the form

$$\bar{\Psi}\equiv\begin{pmatrix}\bar{q} & q^T\end{pmatrix}\qquad\text{and}\qquad\Psi\equiv\begin{pmatrix}q & \bar{q}^T\end{pmatrix} . \tag{C.16}$$

Consequently, the Dirac term in the Lagrangian appears twice, once for the q and $\bar{q}$, and once for q^C and $\bar{q}^C$. The diquark term in the Lagrangian is simply multiplied by a factor of 2. In terms of these spinors, the portion of the Lagrangian which involves the fermion fields is given by

$$\mathcal{L}=\bar{\Psi}\begin{bmatrix}i\partial\!\!\!/-M_f & \tilde{\Delta}^{ij\dagger}_{\alpha\beta}C\\ C\tilde{\Delta}^{ij}_{\alpha\beta} & i\partial\!\!\!/^T+M_f\end{bmatrix}\Psi . \tag{C.17}$$

It is understood that at the end of the calculation we shall have to divide this result by a factor of two in order to avoid double-counting.

C.2 The Thermodynamic Potential

We begin by noting that, in our case, $\bar{\Psi}$ is not independent of the representation of γ matrices, since

$$\bar{\bar{q}}^T = \left(\bar{q}^T\right)^\dagger \gamma^0 = \left(q^\dagger \gamma^0\right)^* \gamma^0 = q^T \gamma^{0*} \gamma^0 \,. \tag{C.18}$$

The same comment applies for the conjugate momentum Π also, since :

$$\Pi = \begin{pmatrix} \bar{q} i \gamma^0 \\ q^T i \gamma^{0^T} \end{pmatrix} = i \Psi^\dagger \,. \tag{C.19}$$

In the following, we will only use the Dirac representation, which has $\gamma^{0^*} = \gamma^{0^T} = \gamma^0$ and $C = i\gamma^2\gamma^0$.

Observing that,

$$\begin{aligned} x^\mu &= (x^0, \vec{x}), & x_\mu &= (x^0, -\vec{x}), \\ \partial^\mu &= (\partial^0, -\vec{\partial}), \quad \text{and} & \partial_\mu &= (\partial^0, \vec{\partial}) \\ \rightarrow i\partial\!\!\!/ &= i\gamma^0\partial_0 + i\vec{\gamma}\cdot\vec{\partial} \quad \text{and} & \tau &= it \rightarrow i\gamma^0\partial_0 = -\gamma^0\partial_\tau \end{aligned} \tag{C.20}$$

yields

$$i\Pi \frac{\partial \Phi}{\partial \tau} - \mathcal{H} + \mu \mathcal{N} = \bar{\Psi}_a D \Psi_b \tag{C.21}$$

where

$$D = \begin{bmatrix} -\gamma^0\partial_\tau + i\vec{\gamma}\cdot\vec{\nabla} - M_f + \mu\gamma^0 & \tilde{\Delta}^\dagger C \\ C\tilde{\Delta} & -\gamma^0\partial_\tau + i\vec{\gamma}^T\cdot\vec{\nabla} + M_f - \mu\gamma^0 \end{bmatrix} . \tag{C.22}$$

Eq. (C.21) may be converted in to momentum space through the transformation

$$\Psi\left(\vec{x}, \tau\right) = \frac{1}{\sqrt{V}} \sum_n \sum_{\vec{p}} e^{i(\vec{p}\cdot\vec{x} + \omega_n \tau)} \Psi\left(\vec{p}, n\right) \,. \tag{C.23}$$

This decomposition implies that q transforms differently in the upper half space of the 8-component spinor in comparison to the lower half space. In

momentum space, we have

$$i\Pi \tfrac{\partial \Phi}{\partial \tau} - \mathcal{H} + \mu \mathcal{N} = \bar{\Psi}_a \begin{bmatrix} -i\gamma^0\omega_n - \vec{\gamma}\cdot\vec{p} - M_f + \mu\gamma^0 & \tilde{\Delta}^\dagger C \\ C\tilde{\Delta} & -i\gamma^0\omega_n - \vec{\gamma}^T\cdot\vec{p} + M_f - \mu\gamma^0 \end{bmatrix} \Psi_b \tag{C.24}$$

We multiply each 4×4 entry by γ^0 which will not affect the value of the determinant and express D as

$$\begin{aligned} D &= -i\omega_n I_{8x8} + D' \,, \\ D' &= \begin{bmatrix} -\gamma^0\vec{\gamma}\cdot\vec{p} - M_f\gamma^0 + \mu & \gamma^0\tilde{\Delta}^\dagger C \\ \gamma^0 C\tilde{\Delta} & -\gamma^0\vec{\gamma}^T\cdot\vec{p} + M_f\gamma^0 - \mu \end{bmatrix} . \end{aligned}$$

The eigenvalues of D' (which is now Hermitian) can be calculated. These eigenvalues will occur in pairs with each member of the pair being the negative of the other. This allows us to calculate the determinant of D, which reads

$$\begin{aligned} \det D &= \left(-i\omega_n + \lambda_1\right)\left(-i\omega_n - \lambda_1\right) \ldots \left(-i\omega_n + \lambda_{72}\right)\left(-i\omega_n - \lambda_{72}\right) \\ &= \left(\omega_n^2 + \lambda_1^2\right) \ldots \left(\omega_n^2 + \lambda_{72}^2\right) \,. \end{aligned} \tag{C.25}$$

The partition function is [119]

$$\ln Z = \sum_{\vec{p}} \sum_n \ln \det D \,. \tag{C.26}$$

The Matsubara sums over the frequencies ω_n are formally divergent, but these are harmless since an infinite constant may be removed by applying the identity

$$\sum_n \ln \beta^2 \left(\omega_n^2 + x^2\right) = \int_1^x d\theta \left(\frac{1}{2} - \frac{1}{1 + e^\theta}\right) = \frac{x}{2} + \ln\left(1 + e^{-x}\right) . \tag{C.27}$$

Notice that since the LHS is invariant under $x \rightarrow -x$, the RHS must be also.

The partition function is given in terms of the eigenvalues above:

$$\ln Z = \frac{V}{2} \int \frac{d^3p}{(2\pi)^3} \sum_{i=1}^{72} \left[\frac{\lambda_i}{2T} + T \ln\left(1 + e^{-\lambda_i}\right)\right] , \tag{C.28}$$

where we have divided by a factor of two to account for the double counting inherent in the Nambu-Gorkov formalism. This result is utilized in Eq. (5.5).

Eq. (C.28) requires the calcuation of the eigenvalues of a 72×72 matrix. This matrix is block diagonal, with two 12×12 blocks corresponding to the two Nambu-Gorkov copies of the matrix that "pairs" up-red, down-green, and strange-blue quarks. The remaining diagonal matrices are the two Nambu-Gorkov copies of 4×4 matrices that pair $dr - ug$, $sr - ub$, and $db - sg$ quarks. In principle, the complication of the Dirac structure in this matrix may be removed by going to the second quantization formalism, however; this is at the expense of introducing proper expressions for spinor normalization as done in Ref. [114]. In the limit where all of the chemical potentials are equal, as in Refs. [113, 114], the matrices all become 4×4 or smaller. In the CFL limit (all quarks massless and all gaps equal), the eigenvalues and their respective degeneracies are:

$$\begin{array}{ll} \pm\sqrt{(p+\mu)^2 + 4\Delta^2} & \text{2 times} \\ \pm\sqrt{(p-\mu)^2 + 4\Delta^2} & \text{2 times} \\ \pm\sqrt{(p+\mu)^2 + \Delta^2} & \text{16 times} \\ \pm\sqrt{(p-\mu)^2 + \Delta^2} & \text{16 times} \end{array} \tag{C.29}$$

while in the 2SC limit (only the strange quark massive and only Δ_{ud} is non-zero), the eigenvalues and their respective degeneracies are:

$$\begin{array}{ll} \pm\,(p-\mu) & \text{4 times} \\ \pm\,(p+\mu) & \text{4 times} \\ \pm\,(E-\mu) & \text{6 times} \\ \pm\,(E+\mu) & \text{6 times} \\ \pm\sqrt{(p+\mu)^2 + \Delta_{ud}^2} & \text{8 times} \\ \pm\sqrt{(p-\mu)^2 + \Delta_{ud}^2} & \text{8 times} \end{array} \tag{C.30}$$

where $E^2 = p^2 + m_s^2$. The eigenvalues given in Eqs. (C.29) and (C.30) provide approximations to the full eigenvalues in Eq. (5.5).